A&A 623, A1 (2019)
https://doi.org/10.1051/0004-6361/201833741

Astronomy & Astrophysics

The Fornax Deep Survey with the VST

V. Exploring the faintest regions of the bright early-type galaxies inside the virial radius*

E. Iodice[1], M. Spavone[1], M. Capaccioli[2], R. F. Peletier[3], G. van de Ven[4], N. R. Napolitano[1], M. Hilker[4], S. Mieske[5], R. Smith[6], A. Pasquali[7], L. Limatola[1], A. Grado[1], A. Venhola[3,8], M. Cantiello[9], M. Paolillo[2], J. Falcon-Barroso[10,11], R. D'Abrusco[12], and P. Schipani[1]

[1] INAF – Astronomical Observatory of Capodimonte, via Moiariello 16, 80131 Naples, Italy
e-mail: enrichetta.iodice@inaf.it
[2] University of Naples "Federico II", C.U. Monte Sant'Angelo, Via Cinthia, 80126 Naples, Italy
[3] Kapteyn Astronomical Institute, University of Groningen, PO Box 72, 9700 AV Groningen, The Netherlands
[4] European Southern Observatory, Karl-Schwarzschild-Strasse 2, 85748 Garching bei Munchen, Germany
[5] European Southern Observatory, Alonso de Cordova 3107, Vitacura, Santiago, Chile
[6] Department of Astronomy and Institute of Earth-Atmosphere-Astronomy, Yonsei University, 03722 Seoul, Korea
[7] Astronomisches Rechen-Institut Zentrum für Astronomie der Universität Heidelberg, Monchhofstrasse 12-14, 69120 Heidelberg, Germany
[8] Division of Astronomy, Department of Physics, University of Oulu, Oulu, Finland
[9] INAF – Astronomical Abruzzo Observatory, Via Maggini, 64100 Teramo, Italy
[10] Instituto de Astrofísica de Canarias, C/ Via Láctea s/n, 38200 La Laguna, Canary Islands, Spain
[11] Departamento de Astrofísica, Universidad de La Laguna, 38200 La Laguna, Tenerife, Spain
[12] Smithsonian Astrophysical Observatory, Chandra X-ray centre, Cambridge, MA 02138, USA

Received 29 June 2018 / Accepted 29 November 2018

ABSTRACT

Context. This paper is based on the multi-band (*ugri*) Fornax Deep Survey (FDS) with the VLT Survey Telescope (VST). We study bright early-type galaxies ($m_B \leq 15$ mag) in the 9 square degrees around the core of the Fornax cluster, which covers the virial radius ($R_{vir} \sim 0.7$ Mpc).
Aims. The main goal of the present work is to provide an analysis of the light distribution for all galaxies out to unprecedented limits (in radius and surface brightness) and to release the main products resulting from this analysis in all FDS bands. We give an initial comprehensive view of the galaxy structure and evolution as a function of the cluster environment.
Methods. From the isophote fit, we derived the azimuthally averaged surface brightness profiles, the position angle, and ellipticity profiles as a function of the semi-major axis. In each band, we derived the total magnitudes, effective radii, integrated colours, and stellar mass-to-light ratios.
Results. The long integration times, the arcsec-level angular resolution of OmegaCam at VST, and the large covered area of FDS allow us to map the light and colour distributions out to large galactocentric distances (up to about 10−15 R_e) and surface brightness levels beyond $\mu_r = 27$ mag arcsec^{-2} ($\mu_B \geq 28$ mag arcsec^{-2}). Therefore, the new FDS data allow us to explore in great detail the morphology and structure of cluster galaxies out to the region of the stellar halo. The analysis presented in this paper allows us to study how the structure of galaxies and the stellar population content vary with the distance from the cluster centre. In addition to the intra-cluster features detected in previous FDS works, we found a new faint filament between FCC 143 and FCC 147, suggesting an ongoing interaction.
Conclusions. The observations suggest that the Fornax cluster is not completely relaxed inside the virial radius. The bulk of the gravitational interactions between galaxies happens in the W-NW core region of the cluster, where most of the bright early-type galaxies are located and where the intra-cluster baryons (diffuse light and globular clusters) are found. We suggest that the W-NW sub-clump of galaxies results from an infalling group onto the cluster, which has modified the structure of the galaxy outskirts (making asymmetric stellar halos) and has produced the intra-cluster baryons (ICL and GCs), concentrated in this region of the cluster.

Key words. surveys – galaxies: photometry – galaxies: elliptical and lenticular, cD – galaxies: clusters: individual: Fornax

* The tables and profiles resulting from the isophote fit are only available at the CDS via anonymous ftp to cdsarc.u-strasbg.fr (130.79.128.5) or via http://cdsarc.u-strasbg.fr/viz-bin/qcat?J/A+A/623/A1

1. Introduction

Clusters of galaxies are excellent sites to study the effects of the environment on the galaxy structure and on the star formation rate (e.g. Trujillo et al. 2001; Lewis et al. 2002; Aguerri et al. 2004; Gutiérrez et al. 2004; Méndez-Abreu et al. 2012; Aguerri 2016; Merluzzi et al. 2016; Lisker et al. 2018). There are several types of environmental mechanisms that can act, also simultaneously, on the cluster members, which induce strong changes in the stellar distribution and gas content. The process of repeated high-speed tidal encounters of the galaxies inside the cluster, which induce galaxy–galaxy gravitational interactions, and/or with the intra-cluster medium is known as galaxy harassment (Moore et al. 1998). It generates a tidal mass loss from the galaxies, which depends on the orbit of the galaxy inside the cluster (Mastropietro et al. 2005; Smith et al. 2015). The tidal forces can strip dark matter, stars, and gas from galaxies, which generates faint streams detectable along the orbit of the galaxy through the cluster. This mechanism is more efficient in low-mass galaxies (Smith et al. 2010). The interaction of gas-rich galaxies with the hot interstellar medium, known as ram-pressure stripping, can sweep off their atomic gas and therefore halt the star formation (Gunn & Gott 1972). The ram-pressure stripping can also remove the hot, ionised gas within the halo of a galaxy, so that the supply of cold gas is lost. This is the so-called "strangulation" that is able to shut down the star formation in a galaxy (Larson et al. 1980; Dekel & Birnboim 2006; Peng et al. 2015). The strangulation also occurs when the inflow of new gas onto the galaxy hot gas halo is stopped (Dekel & Birnboim 2006). The mechanisms listed above, which induce morphological transformation and/or the quenching of the star formation are thought to be partly responsible for the morphology-density relation (Dressler et al. 1997; van der Wel et al. 2010; Fasano et al. 2015), where early-type galaxies (ETGs) dominate the central regions of the clusters, while late-type galaxies (LTGs), spirals, and irregulars populate the outskirts. Recently, to investigate the many processes acting in clusters, the "phase-space diagram" has been used, where the cluster-centric velocities and radii are combined in one plot (see Smith et al. 2015; Jaffé et al. 2015; Rhee et al. 2017; Pasquali et al. 2019, and references therein).

In the deep potential well at the cluster centre, the galaxies continue to undergo active mass assembly and, in this process, gravitational interactions and merging between systems of comparable mass and/or smaller objects play a fundamental role in defining the galaxies' morphology and the build-up of the stellar halos. During the infall of groups of galaxies to form the cluster, the material stripped from the galaxy outskirts builds up the intra-cluster light, ICL (De Lucia & Blaizot 2007; Puchwein et al. 2010; Cui et al. 2014). This is a diffuse faint component that grows over time with the mass assembly of the cluster, to which the relics of the interactions between galaxies (stellar streams and tidal tails) also contribute (see Arnaboldi & Gerhard 2010; Tutukov & Fedorova 2011; Mihos 2015, as reviews).

The evolution of galaxies in a cluster is mainly driven by the processes listed above. Their effects strictly depend on some parameters related to the internal structure of the galaxy (like the total mass) to the orbits, relative velocities, and to the location of the galaxy in the cluster.

In this framework, the study of ETGs, elliptical and lenticular (S0) galaxies, has a special role. Since these galaxies are mainly located close to the cluster centre, they are good tracers of past galaxy interactions and mass assembly that shaped their structure, from the inner, bright regions to their faint outskirts. Important hints for the formation and evolution of ETGs reside in the morphology, age, metallicity, mass-to-light ratio, and in the kinematics (see Buta 2011; de Zeeuw et al. 2002, as review). The most recent studies on the photometry of galaxies in nearby clusters are the extensive analyses by Kormendy et al. (2009) for the Virgo cluster and by Gutiérrez et al. (2004) for the Coma cluster. Recent integral-field spectroscopic surveys offer the largest kinematic database to study the stellar population in ETGs (e.g. SAURON, ATLAS^{3D}, CALIFA, SAMI, de Zeeuw et al. 2002; Cappellari et al. 2011; Sánchez et al. 2012; Bryant et al. 2015).

In this context, the VST Early-type GAlaxy Survey (VEGAS[1]) aims to provide deep multi-band imaging and quantitative photometric analysis for a large sample of ETGs in different environments, including giant cD galaxies in the core of clusters (Capaccioli et al. 2015; Spavone et al. 2017). The main goal of VEGAS is to study the galaxy structure down to the faintest levels of surface brightness of $\mu_g \sim 27$–30 mag arcsec^{-2}, in order to map also the regions of the stellar halos and the ICL. VEGAS is producing competitive results to the several pioneering deep imaging surveys (Mihos et al. 2005, 2017; Janowiecki et al. 2010; Martínez-Delgado et al. 2010; Roediger et al. 2011; Ferrarese et al. 2012; Duc et al. 2015; van Dokkum et al. 2014; Munoz et al. 2015; Trujillo & Fliri 2016; Merritt et al. 2016; Crnojević et al. 2016).

The Fornax Deep Survey at VST (FDS) is one part of the deep-surveys campaign. It is a joint project based on VEGAS (PI E. Iodice) and the OmegaCam guaranteed time (PI R. Peletier), which aims to cover the whole Fornax cluster out to the virial radius (~0.7 Mpc, Drinkwater et al. 2001), with an area of about 26 square degrees around the central galaxy NGC 1399 in the cluster core and including the SW subgroup centred on NGC 1316. To date, together with the *Hubble* Space Telescope data (Jordán et al. 2007) and the Dark Energy Camera (DECAM) data for the Next Generation Fornax Cluster Survey (Munoz et al. 2015), FDS is the deepest and widest dataset mapping the Fornax cluster in the optical wavelength range. These surveys are part of the multi-wavelength observations available for this cluster, such as the *Herschel* survey (Davies et al. 2013), *Chandra* X-ray imaging of the cluster core (Scharf et al. 2005), and UV GALEX imaging (Martin et al. 2005). Upcoming data from Atacama Large Millimeter/submillimeter Array (ALMA, PI T. Davis) and neutral hydrogen HI data from the MeerKat survey (Serra et al. 2016) will provide a complete census of the cool interstellar medium in Fornax. In addition, the integral-field spectroscopy is now available for dwarf and giant galaxies in Fornax with several instruments, including SAMI (Scott et al. 2014) and Multi Unit Spectroscopic Explorer (MUSE; Sarzi et al. 2018).

The Fornax cluster is the second most massive galaxy concentration within 20 Mpc, after the Virgo cluster, with a virial mass of $M = 7 \times 10^{13}\, M_\odot$ (Drinkwater et al. 2001). It is among the richest nearby sites to study galaxy evolution and dynamical harassment in a dense environment. Previous works indicate that it has a complex structure and the mass assembly is still ongoing (Drinkwater et al. 2001; Scharf et al. 2005). The core is in a quite evolved phase (Grillmair et al. 1994; Jordán et al. 2007), since most of the bright ($m_B < 15$ mag) cluster members are ETGs (Ferguson 1989), more than in the Virgo cluster. It hosts a vast population of dwarf galaxies and ultra compact galaxies (Munoz et al. 2015; Hilker 2015; Schulz et al. 2016; Venhola et al. 2017, 2018; Eigenthaler et al. 2018), an intra-cluster population of globular clusters (GCs; Schuberth et al. 2008, 2010; D'Abrusco et al. 2016; Cantiello et al. 2018; Pota et al. 2018), and of planetary

[1] see http://www.na.astro.it/vegas/VEGAS/Welcome.html

nebulae (Napolitano et al. 2003; McNeil-Moylan et al. 2012; Spiniello et al. 2018).

FDS provided the mosaic of 3 × 2 square degrees around the central galaxy NGC 1399[2] in the core and around the brightest cluster member in the SW subgroup, NGC 1316[3]. With FDS we (i) mapped the surface brightness around NGC 1399 and NGC 1316 out to an unprecedented distance of about ∼200 kpc ($R \sim 6\,R_e$) and down to $\mu_g \simeq 29{-}31$ mag arcsec^{-2} (Iodice et al. 2016, 2017a); (ii) traced the spatial distribution of candidate globular clusters (GCs) inside ∼0.5 deg^2 of the cluster core (D'Abrusco et al. 2016; Cantiello et al. 2018); (iii) detected new and faint ($\mu_g \sim 29{-}30$ mag arcsec^{-2}) features in the intra-cluster region between NGC 1399 and NGC 1387 (Iodice et al. 2016) and in the outskirts of NGC 1316 (Iodice et al. 2017a); (iv) detected a previously unknown region of ICL in the core of the cluster, on the west side of NGC 1399 (Iodice et al. 2017b); (v) provided a census of the low-surface brightness and dwarf galaxies in the whole area covered by FDS (Venhola et al. 2017, 2018).

The FDS observations were completed at the end of 2017. A full description of the data and survey plans will be presented soon in a forthcoming paper (Peletier et al., in prep.). Taking advantage of the multi-band deep observations, the large field-of-view of OmegaCam at VST, and the optimised observing strategy, the "novelty" of FDS consists in the systematic characterisation of many basic, global properties of the galaxies in the Fornax cluster over a wide baseline of radius. These global properties include luminosity profiles, isophote shapes, galaxy outskirts, colour gradients, and inventories of satellite galaxies and GCs. The published papers on FDS proved the ability to study the galaxy outskirts, mapping the regions of the stellar halos and intra-cluster space to detect any kind of low-surface brightness structures and their connection with the environment.

In this work we focus on the inner 9 square degrees around the core of the Fornax cluster, which corresponds to about the viral radius (∼0.7 Mpc). We study the ETGs brighter than $m_B = 15$ mag ($M_B = -16.4$ mag) inside this area (19 objects), as a complete sample, in magnitude and morphological type, of galaxies inside the virial radius of the Fornax cluster. The main goal of the present work is to provide the analysis of the light and colour distribution out to unprecedented limits (in radius and surface brightness) and to release the main products resulting from this analysis (i.e. total magnitudes, effective radii, integrated colours and M/L ratios). We also give a global comprehensive view of the galaxy structure as a function of the cluster environment from observations, focusing on the results mainly based on the new FDS data. Therefore, with the present paper, we aim at providing the observables to be used in forthcoming and ongoing works on specific science topics.

2. FDS data

This work is based on the Fornax Deep Survey (FDS) data in the *u*,*g*,*r* and *i* bands, inside an area of 9 square degrees around the core of the Fornax cluster, ($\alpha = 03^h38^m29.024^s$, $\delta = -35^d27'03.18''$, see Fig. 1). The area covers the virial radius of the cluster, which is $R_{vir} \sim 0.7$ Mpc (Drinkwater et al. 2001).

FDS observations are part of the Guaranteed Time Observation surveys, FOCUS (PI R. Peletier) and VEGAS (PI E. Iodice, Capaccioli et al. 2015) obtained with the ESO VLT Survey Telescope (VST). VST is a 2.6-m wide field optical survey telescope, located at Cerro Paranal in Chile (Schipani et al. 2012), equipped with the wide field camera (1 × 1 deg^2) OmegaCam that has a pixel scale of 0.21 arcsec pixel^{-1}.

The central FDS fields (F11, F16) were presented by Iodice et al. (2016, 2017a) and Venhola et al. (2017), which works include a detailed description of the observing strategy and the data reduction pipelines used for FDS. The data used in this work (see Fig. 1), which includes also the already published FDS fields cited above, were collected during several visitor mode runs (from 2013 to 2017, see Table 1) in dark time for the *u*, *g*, and *r* bands and in grey time for the *i* band and were reduced with the VST-Tube pipeline (Grado et al. 2012; Capaccioli et al. 2015). The image quality of all FDS fields is presented by Venhola et al. (2018).

As pointed out by Iodice et al. (2016, 2017a) and Venhola et al. (2017), in order to track the background variation exposure by exposure and therefore have a very accurate estimate of the sky background around bright and extended galaxies, the FDS fields were obtained by using a step-dither observing strategy. It consists of a cycle of short exposures (150 s) of adjacent fields, close in time and space (≤1 deg away). The "empty" fields, that is, those with no bright stars or galaxies, were adopted to derive an average sky frame for each night and each band. This is scaled and subtracted from each science frame. The average sky frame derived for each observing night takes into account the small contribution to the sky brightness by the smooth components (i.e. galactic cirrus, zodiacal light, and terrestrial airglow) plus the extragalactic background light. In the sky-subtracted science frame some "residual fluctuations" could remain of a few percent in flux, which are due to the flux variation of the background during the night. These are estimated on the final stacked image (see Sect. 3) and set the accuracy of the sky-subtraction step (see also Iodice et al. 2016; Venhola et al. 2017).

For each field we obtained 76 exposures (of 150 s each) in the *u* band, 54 in the *g* and *r* bands, and 35 in the *i* band, giving a total exposure time of 3.17 h in the *u* band, 2.25 h in the *g* and *r* bands, and 1.46 h in the *i* bands. Only images with seeing $FWHM \leq 1.5$ arcsec were co-added. The resulting total exposure times for each filter are listed in Table 1.

The full *g*-band mosaic of the 9 square degrees around the core of the Fornax cluster is shown in Fig. 2. The dataset studied in this work includes all ETGs brighter than $m_B \leq 15$ mag selected from Ferguson (1989; see Table 2 and Fig. 1). Fainter objects are classified as dwarf galaxies. The *r*-band image in surface brightness levels for each galaxy of the sample is shown in Appendix A.

3. Surface photometry of the ETGs in the Fornax cluster

In this section we describe the method adopted to study VST images and the main steps to provide the parameters characterising the galaxy structure (i.e. total magnitudes, colours and effective radii). We have chosen one galaxy of the sample, FCC 167 (see Fig. 3), to describe each step of the analysis in detail. FCC 167 (also known as NGC 1380) is a lenticular galaxy in the NW side of the Fornax cluster, located at ∼0.6° (∼219 kpc) from NGC 1399 (see Fig. 2) and at a distance of ∼21 Mpc from us (Blakeslee et al. 2010). This object was chosen as a showcase since it is close to the core of the cluster but outside the extended stellar halo of NGC 1399, which is mapped out to 33 arcmin (Iodice et al. 2016). Results for all galaxies of the sample are

[2] See the ESO photo release at https://www.eso.org/public/news/eso1612/

[3] See the ESO photo release at https://www.eso.org/public/news/eso1734/

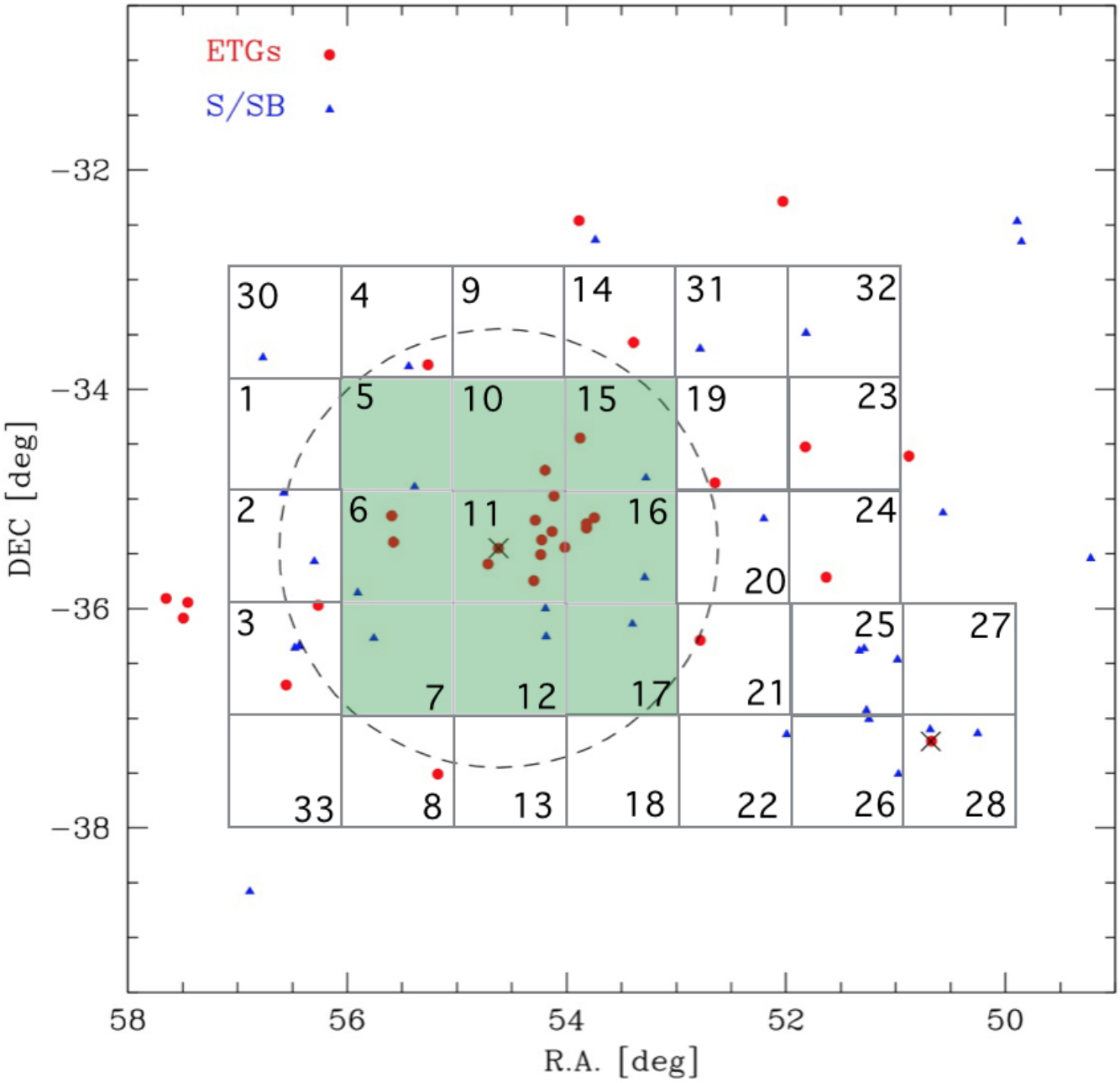

Fig. 1. Distribution of early-type (elliptical and S0s, red circles) and late-type galaxies (blue triangles) in the Fornax cluster and in the subgroup Fornax A, brighter than $m_b < 15$ mag (see also Table 2). The two crosses indicate the location of NGC 1399 at the centre of the cluster (RA = 54.62°, Dec = −35.45°) and of NGC 1316 at the centre of the SW subgroup (RA = 50.67°, Dec = −37.21°). The dashed circle corresponds to the virial radius $R_{\rm vir} \sim 0.7$ Mpc. Squares are the FDS fields of $1 \times 1°$. The green boxes are the FDS fields presented in this work.

described in Appendix A and related images and profiles are shown in Appendices B and C.

Method: Isophote fitting – From the sky-subtracted FDS field, we extracted the azimuthally averaged intensity profile for each object of the sample in each band, by using the IRAF[4] task ELLIPSE. The method is described in detail by Iodice et al. (2016), where the galaxy properties of the central cluster galaxy NGC 1399 were presented. The main steps, performed for each image in each filter, are:

1. mask all the bright sources (galaxies and stars) and background objects close to the galaxy under study;
2. fit the isophotes in elliptical annuli centred on the galaxy out to the edge of the FDS field (out to about 0.5 deg), where all fitting parameters (centre, position angle, and ellipticity) were left free. For those galaxies that are in the overlapping regions between two FDS fields (see Fig. 1), we performed this analysis on the mosaic of the two fields;
3. from the intensity profiles in each band, estimate the outermost radius $R_{\rm lim}$ from the centre of the galaxy where the galaxy's light blends into the average background level[5]. We

[4] The Image Reduction and Analysis Facility is distributed by the National Optical Astronomy Observatory (NOAO), which is operated by the Association of Universities for Research in Astronomy (AURA), Inc. under cooperative agreement with the National Science Foundation.

[5] The average background level is the residual after subtracting the sky frame, and therefore very close to zero (see Iodice et al. 2016).

Table 1. Fornax Deep Survey observations used in this work.

Field	*u* band			*g* band			*r* band			*i* band		
	date	Exp. T. (h)	*FWHM* (arcsec)	date	Exp. T. (h)	*FWHM* (arcsec)	date	Exp. T. (h)	*FWHM* (arcsec)	date	Exp. T. (h)	*FWHM* (arcsec)
(1)	(2)	(3)	(4)	(5)	(6)	(7)	(8)	(9)	(10)	(11)	(12)	(13)
F5	Nov 2015	2.9	1.33	Nov 2014/2015	2.5	1.15	Nov 2014/2015	2.7	1.39	Nov 2014/2015	2.2	1.08
F6	Nov 2013	2.12	1.11	Nov 2013	2.3	0.84	Nov 2013	2.2	1.08	Nov 2014	1.0	1.21
F7	Nov 2013	2.12	1.04	Nov 2013	2.3	0.83	Nov 2013	2.2	0.95	Nov 2014	1.0	1.42
F10	Nov 2015	2.9	1.34	Nov 2014/2015	2.5	1.15	Nov 2014/2015	2.7	1.02	Nov 2014/2015	2.2	1.09
F11	Nov 2014	3.7	1.27	Nov 2014	2.2	1.06	Nov 2014	2.1	1.09	Nov 2014	1.3	1.15
F12	Nov 2013	2.12	1.15	Nov 2013	2.3	0.83	Nov 2013	2.2	1.04	Nov 2014	1.0	1.17
F15	Nov 2013/2014	3.7	1.30	Nov 2013/2014	2.2	1.13	Nov 2013/2014	2.1	0.9	Nov 2013/2014	1.3	0.97
F16	Nov 2014	3.7	1.31	Nov 2014	2.2	1.26	Nov 2014	2.1	0.94	Nov 2014	1.3	1.08
F17	Nov 2014	3.7	1.27	Nov 2014	2.2	1.11	Nov 2014	2.1	0.87	Nov 2014	1.3	1.01

Notes. Column 1: FDS field, see Fig. 1. Columns 2–4: date of the observations, total exposure time in hours, and average seeing in arcsec for the *u* filter. Columns 5–13: same as Cols. 2–4 for the *g*, *r*, and *i* bands. The FWHM is computed for all FDS fields by Venhola et al. (2018).

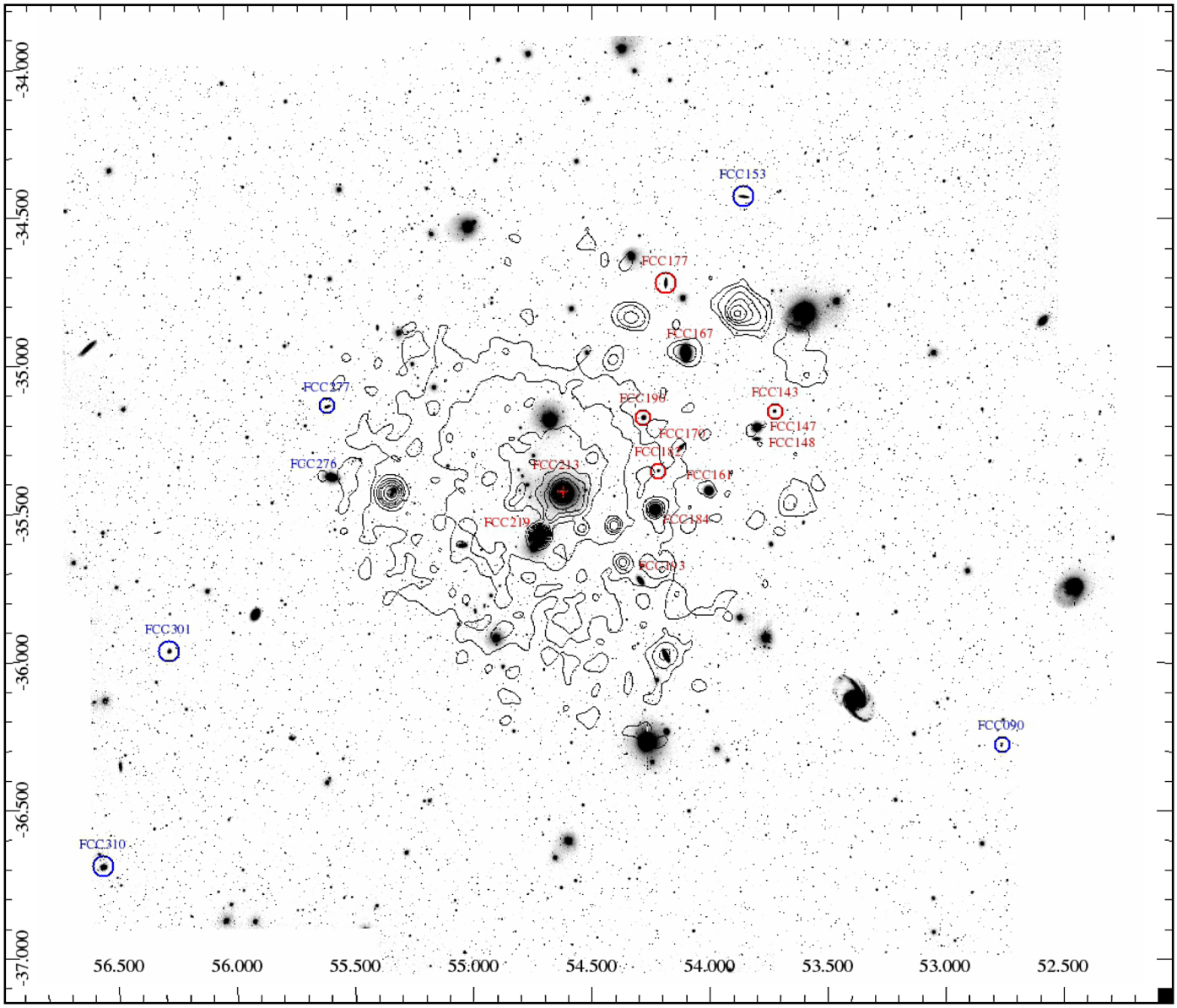

Fig. 2. VST mosaic in the *g* band of the Fornax cluster inside the virial radius (see Fig. 1). The image size is about 9 square degrees. Black contours are the X-Ray emission from ROSAT (Paolillo et al. 2002). The X-ray contours are spaced by a factor of 1.3, with the lowest level at 3.0×10^{-3} counts arcmin^{-2} s^{-1}. All ETGs studied in the present work (see Table 2) are labelled on the image. Galaxies marked with blue symbols have $g-i \leq 0.8$ mag and $g-r \leq 0.4$ mag (see Sect. 4 for details). North is up and east is on the left.

Table 2. Early-type galaxies inside the virial radius ($R_{vir} \sim 0.7$ Mpc) of the Fornax cluster, brighter than $m_B < 15$ mag.

Object	α h:m:s	δ d:m:s	Morph type	Distance Mpc	m_B mag	FDS field	Names
(1)	(2)	(3)	(4)	(5)	(6)	(7)	(8)
FCC 090	03 31 08.1	–36 17 19	E4 pec	19.5 ± 1.7	15.0	F16–F17	
FCC 143	03 34 59.1	–35 10 10	E3	19.3 ± 0.8	14.3	F16	NGC 1373, ESO 358-G21
FCC 147	03 35 16.8	–35 13 34	E0	19.6 ± 0.6	11.9	F16	NGC 1374, ESO 358-G23
FCC 148	03 35 16.8	–35 15 56	S0	19.9 ± 0.7	13.6	F16	NGC 1375, ESO 358-G24
FCC 153	03 35 30.9	–34 26 45	S0	20.8 ± 0.7	13.0	F10–F15	IC 1963, ESO 358-G26
FCC 161	03 36 04.0	–35 26 30	E0	19.9 ± 0.4	11.7	F11–F16	NGC 1379, ESO 358-G37
FCC 167	03 36 27.5	–34 58 31	S0/a	21.2 ± 0.7	11.3	F10–F11	NGC 1380, ESO 358-G28
FCC 170	03 36 31.6	–35 17 43	S0	21.9 ± 0.8	13.0	F11	NGC 1381, ESO 358-G29
FCC 177	03 36 47.4	–34 44 17	S0	20.0 ± 0.6	13.2	F10	NGC 1380A, ESO 358-G33
FCC 182	03 36 54.3	–35 22 23	SB0 pec	19.6 ± 0.8	14.9	F11	
FCC 184	03 36 56.9	–35 30 24	SB0	19.3 ± 0.8	12.3	F11	NGC 1387, ESO 358-G36
FCC 190	03 37 08.9	–35 11 37	SB0	20.3 ± 0.7	13.5	F11	NGC 1380B, ESO 358-G37
FCC 193	03 37 11.7	–35 44 40	SB0	21.2 ± 0.7	12.8	F11	NGC 1389, ESO 358-G38
FCC 213	03 38 29.2	–35 27 02	E0	20.9 ± 0.9	10.6	F11	NGC 1399, ESO 358-G45
FCC 219	03 38 52.1	–35 35 38	E2	20.2 ± 0.7	10.9	F11	NGC 1404, ESO 358-G46
FCC 276	03 42 19.2	–35 23 36	E4	19.6 ± 0.6	11.8	F6	NGC 1427, ESO 358-G52
FCC 277	03 42 22.6	–35 09 10	E5	20.7 ± 0.7	13.8	F6	NGC 1428, ESO 358-G53
FCC 301	03 45 03.5	–35 58 17	E4	19.7 ± 0.7	14.2	F7	ESO 358-G59
FCC 310	03 46 13.7	–36 41 43	SB0	19.9 ± 0.6	13.5	F3–F7	NGC 1460, ESO 358-G62

Notes. Column 1: Fornax cluster members from Ferguson (1989). Columns 2 and 3: right ascension and declination. Columns 4–6: morphological type, distance, and total magnitude in the B band given by Ferguson (1989) and Blakeslee et al. (2009). For FCC 161 the distance is from Tonry et al. (2001). Column 7: location in the FDS field (see Fig. 1). Column 8: other catalogue name.

estimated the average sky fluctuation levels (Δ sky) and the "amplitudes" of the distribution, that is, the RMS of the mean value at one sigma. We assume as the latest valuable science point in the surface brightness profile the point where flux ≥Δ sky. The average RMS on the sky subtraction increases from the u to the i band, with the following average values: ∼0.01−0.08 counts in the u band; ∼0.02−0.13 counts in the g band; ∼0.03−0.2 counts in the r band and ∼0.08−0.3 counts in the i band. For FCC 167, this step is shown in Fig. 3 (lower-left panel), where $R_{lim} = 10.2$ arcmin in the r band.

Products: Total magnitudes, effective radii, colours, mass-to-light ratio

1. From the isophote fit, we derive the azimuthally averaged surface brightness (SB) profiles (corrected for the residual background level estimated at $R \geq R_{lim}$), the position angle (PA) and ellipticity (ϵ) profiles (where $\epsilon = 1 - b/a$, and b/a is the axial ratio of the ellipses) as a function of the semi-major axis, in each band. The error estimates on the magnitudes take the uncertainties on the photometric calibration (∼0.001−0.006 mag) and sky subtraction into account (Capaccioli et al. 2015; Iodice et al. 2016). For FCC 167 the SB profiles in the r band are shown in Fig. 3. For all the galaxies of the sample, results from the isophote fit are shown in Appendix B.
2. From the azimuthally averaged SB profiles, we derive the $g-i$ colour profiles and from the corresponding images we make the $g-i$ colour maps. For FCC 167 they are shown in Fig. 4. For all the galaxies of the sample, the $g-i$ colour maps and colour profiles are shown in Appendix C.
3. Using a growth curve analysis, derived from the isophote fit in the elliptical apertures, we compute the total magnitudes and effective radii (R_e) inside the outermost radius R_{lim} in each band. They are listed in Table 3.
4. From the total magnitudes (see Table 3) we computed the $g-i$ and $g-r$ average colours. We also derived the average $g-i$ colours in the inner regions of the galaxy at $R \leq 0.5\,R_e$ and in the outskirts at $R \geq 3\,R_e$. They are listed in Table 4, which also includes the absolute magnitudes and the projected distance of each galaxy from NGC 1399 (assumed as the "centre" of the cluster).
5. From the $g-i$ average colour we estimate the stellar mass M_* by using the empirical relation $\log_{10}\frac{M_*}{M_\odot} = 1.15 + 0.70(g-i) - 0.4\,M_i$ from Taylor et al. (2011), where M_i is the absolute magnitude in the i band[6]. According to Taylor et al. (2011), this relation provides an estimate of the stellar mass-to-light ratio (M_*/L_i) to a 1σ accuracy of ∼0.1 dex. The M_*/L_i value for each galaxy of the sample is given in Table 4.

4. Mapping the galaxy light distribution beyond $\mu_B = 28$ mag arcsec^{-2} in FDS

The bright galaxies inside the Fornax cluster are well studied in a wide wavelength range and at several resolution levels (see Sect. 1). In this section we show that the main and new contribution from the FDS is to map the light and colour distribution in the optical bands up to unprecedented limits. As shown in Sect. 5, this allows us to systematically characterise, for the first time, the galaxy structure and colour profiles out to the regions of the stellar halos (where $\mu_g \geq 26$ mag arcsec^{-2}).

In Fig. 5 we compare the limiting magnitudes and effective radii obtained by FDS with the estimates from previous works, mainly from Caon et al. (1994), which contains the most extended analysis of the light distribution in the B band for the

[6] The empirical relation proposed by Taylor et al. (2011) assumed a Chabrier IMF.

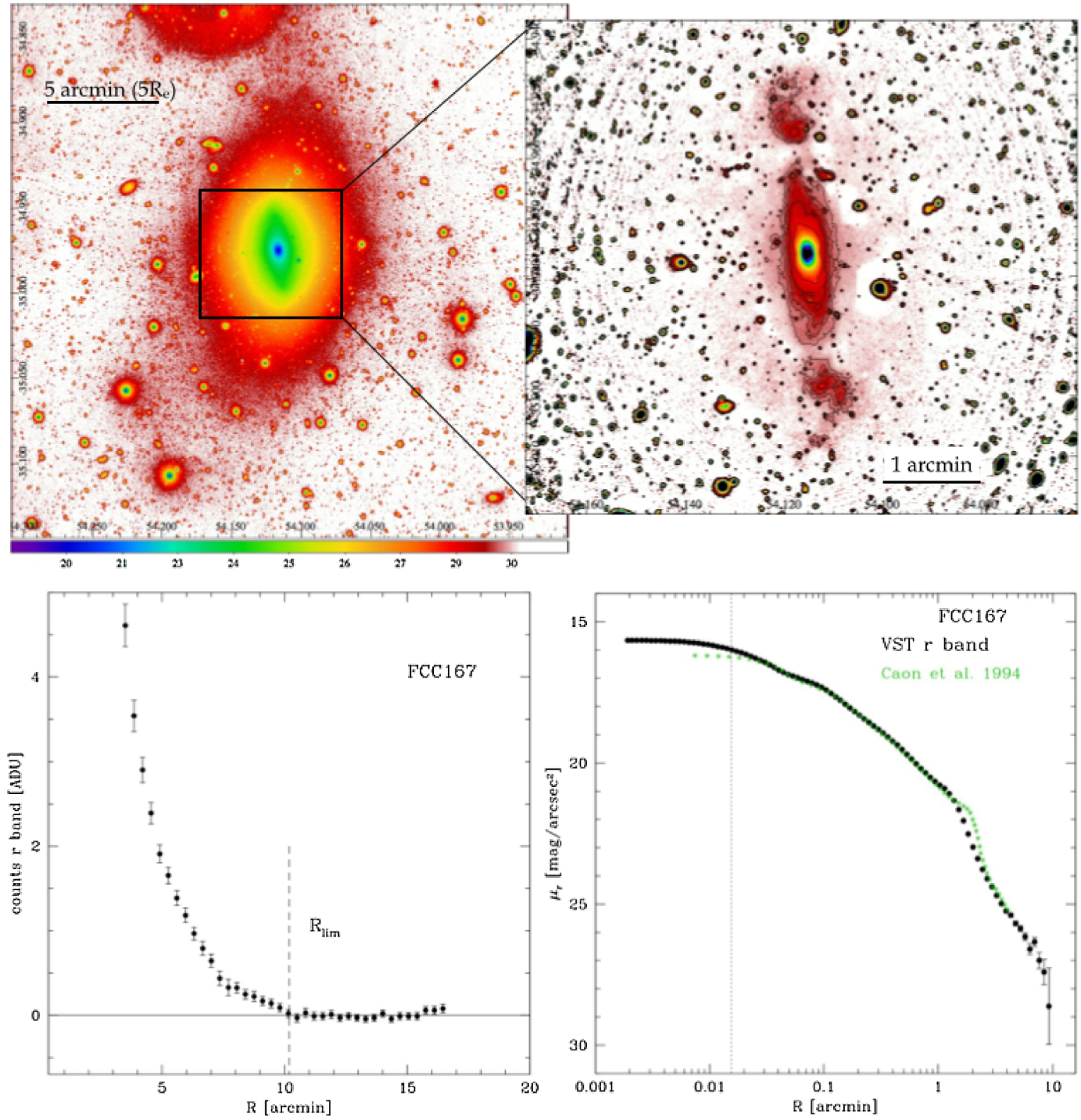

Fig. 3. *Top panels*: extracted region of the VST mosaic of 0.34×0.34 square degrees around FCC 167 in *r* band (*left*), plotted in surface brightness levels (shown in the colour bar). High-frequency residual image obtained from the *r*-band VST image of FCC 167 (*right*). *Lower panels*: intensity profile (*left*), in the *r* band, in the outer regions of FCC 167. For $R \geq 10.2$ arcmin, the galaxy's light blends into the average sky level, which has a residual scatter of about 0.04 counts around the zero (continuous black line). Azimuthally-averaged surface brightness profiles of FCC 167 in the *r* band (*right*) derived from VST data (black points), compared with literature data from Caon et al. (1994) in the *B* band (green asterisks), transformed to *r*-band. The vertical dotted line (*right panel*) delimits the region where the light profiles are "flattened" due to the convolution effect with the point-spread function (PSF). The FWHM of the PSF is about 1 arcsec, which is the average seeing for FDS observations (see Table 1).

majority of the ETGs in the FDS sample: FDS is providing the deepest images of ETGs in the Fornax cluster. For all ETGs in FDS the faintest levels of the azimuthally averaged surface brightness are about two magnitudes deeper than the previous photometry and about twice as extended (see Fig. 5).

Looking at FCC 167, adopted as illustrative example, the *r*-band SB profile extends out to 10 arcmin (~52 kpc) from the centre, which is about 10 R_e, and down to $\mu_r = 29 \pm 1$ mag arcsec^{-2} (see lower-right panel of Fig. 3). The *r*-band SB profile was compared with the light profile from Caon et al. (1994) in the

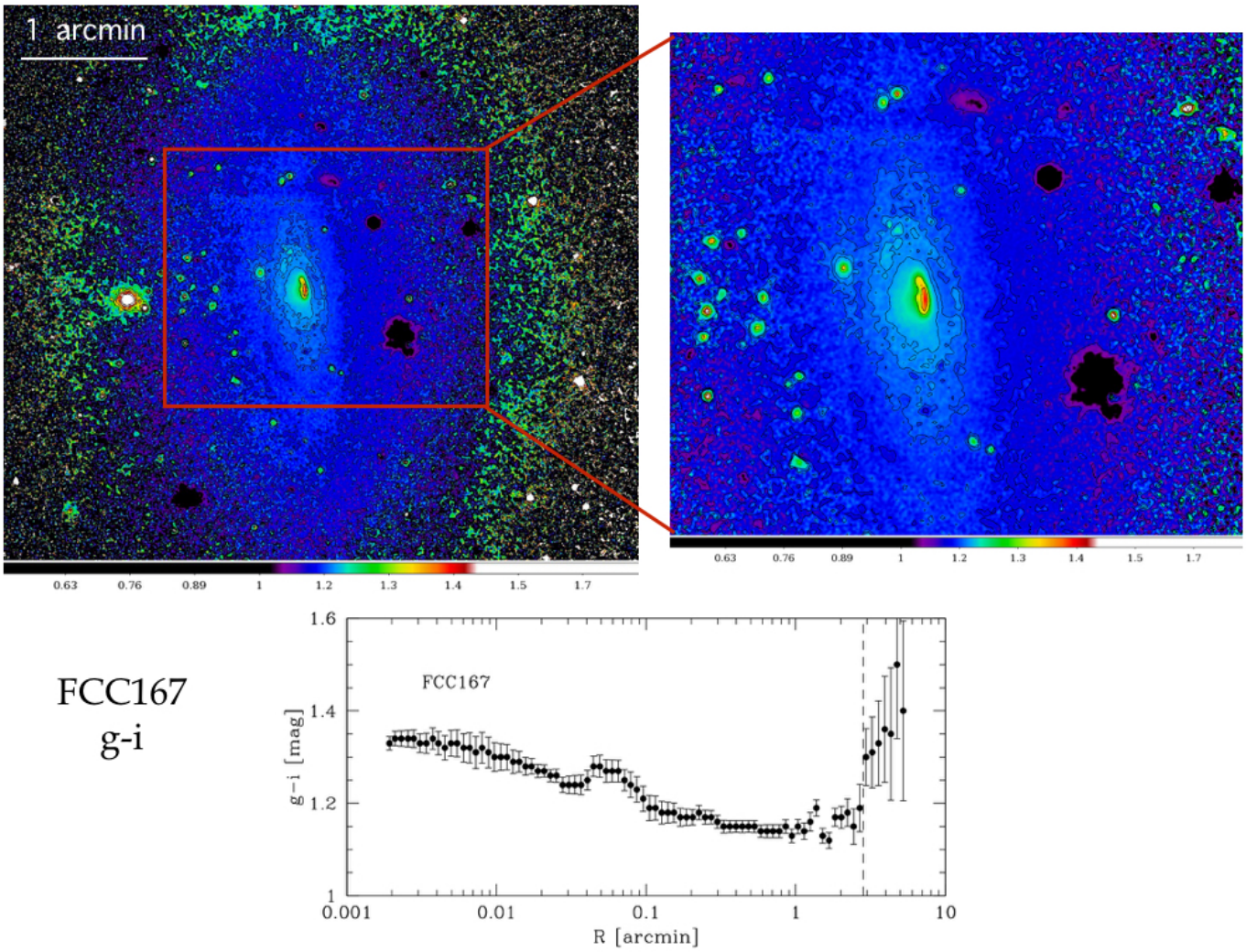

Fig. 4. *Top panels*: $g-i$ colour map of FCC 167 inside 4.5×4.3 arcmin from the centre (*left panel*) and a zoom towards the nuclear regions (*right panel*) for 2.6×1.8 arcmin. The $g-i$ levels are shown in the colour bar. *Bottom panel*: azimuthally-averaged $g-i$ colour profile as function of the semi-major axis by the fit of the ellipses. The vertical long-dashed line indicates the transition radius at $R \sim 3$ arcmin, between the disc and the outer stellar exponential halo (see Sect. A.7).

B band[7], which is not azimuthally averaged but was derived along the major axis of the galaxy. This causes the small difference at $1 \leq R \leq 3$ arcmin, where the B-band profile has a more pronounced "bump". This feature at $R \simeq 2$ arcmin is reasonably due to the bright knots detected along the major axis of the galaxy from the high-frequency residual image[8] (see right panel of Fig. 3) and which are smoothed out in the azimuthally averaged profiles. Except for this, the agreement is satisfactory out to 4 arcmin, the outermost measured SB value from previous photometry. The r-band SB profile from the VST data is two times more extended and about four magnitudes deeper then that from Caon et al. (1994) in the B band.

The SB profiles for all ETGs of the sample in the r band are shown in Fig. 6. As for FCC 167, all of them extend out to $10-15\,R_e$ and down to $\sim 8\,\mu_e$. The shape of the SB profiles appears similar for all the elliptical galaxies (see top panels of Fig. 6), including a shallower decline at larger radii ($R \geq 5\,R_e$), which resembles the typical behaviour of the outer stellar envelope as observed in other ETGs (Seigar et al. 2007; Spavone et al. 2017; Iodice et al. 2016). Most of the S0 galaxies have a Type II profile or a composite Type II + Type III profile (see middle and lower panels of Fig. 6), where one or two breaks are observed in the SB profiles (Erwin et al. 2008). According to Erwin et al. (2008), the inner break in the SB profile is due to the presence of a bar. The outer break could be due to a truncation of the disc or indicates the presence of an outer additional component, like the stellar halo. A quantitative analysis of the SB profiles for all galaxies of the sample, by using a multi-component fit to estimate the scale lengths and total luminosity of each galaxy component (bulge, bar, disc, and stellar halo), will be presented in a forthcoming paper (Spavone et al., in prep.).

Figure 7 shows the azimuthally averaged $g-i$ colour profiles: they are mapped out to $5-10\,R_e$ with an error less than 10%. A colour gradient is evident for five elliptical galaxies of the sample (FCC 143, FCC 147, FCC 161, FCC 219, FCC 213),

[7] Following the colour transformation by Fukugita et al. (1996), where the average $g-r = 0.59$ colour for FCC 167 (see Table 4) is taken into account to estimate the colour term, we derived $B-r = 1.33$ and the B band profile is shifted to the r band, accordingly.

[8] A Gaussian filter of the r-band VST image of FCC 167 given in Fig. 3 was performed by using the IRAF task FMEDIAN. The ratio between the original and filtered image gave the high-frequency residual image shown in the top-right panel of Fig. 3.

Table 3. Total magnitudes and effective radii for the early-type galaxies inside the virial radius ($R_{vir} \sim 0.7$ Mpc) of the Fornax cluster, brighter than $m_B < 15$ mag, in the *ugri* bands.

Object	m_u	m_g	m_r	m_i	Re_u	Re_g	Re_r	Re_i
	mag	mag	mag	mag	arcsec	arcsec	arcsec	arcsec
(1)	(2)	(3)	(4)	(5)	(6)	(7)	(8)	(9)
FCC 090	15.18 ± 0.04	14.16 ± 0.02	13.62 ± 0.03	13.38 ± 0.02	10.34 ± 0.10	10.31 ± 0.06	12.11 ± 0.10	11.31 ± 0.07
FCC 143	14.88 ± 0.06	13.36 ± 0.02	12.66 ± 0.03	12.39 ± 0.07	13.51 ± 0.09	11.86 ± 0.01	11.00 ± 0.05	10.46 ± 0.09
FCC 147	12.67 ± 0.03	11.14 ± 0.01	10.50 ± 0.01	10.15 ± 0.02	38.34 ± 0.12	28.53 ± 0.01	24.8 ± 0.2	24.1 ± 0.2
FCC 148	13.77 ± 0.02	12.33 ± 0.01	11.70 ± 0.01	11.47 ± 0.02	30.4 ± 0.2	27.2 ± 0.2	28.3 ± 0.2	25.04 ± 0.14
FCC 153	13.88 ± 0.02	11.94 ± 0.02	11.70 ± 0.03	11.17 ± 0.01	24.5 ± 0.3	26.3 ± 0.3	19.8 ± 0.7	27.4 ± 0.5
FCC 161	12.85 ± 0.03	11.18 ± 0.01	10.47 ± 0.01	10.14 ± 0.03	28.2 ± 0.2	28.6 ± 0.2	28.6 ± 0.2	26.96 ± 0.03
FCC 167	11.70 ± 0.02	9.86 ± 0.01	9.27 ± 0.02	8.83 ± 0.01	57.9 ± 0.3	72.7 ± 0.5	56.4 ± 0.5	60.0 ± 0.4
FCC 170	13.30 ± 0.01	11.64 ± 0.01	10.99 ± 0.01	10.57 ± 0.01	20.9 ± 0.5	17.97 ± 0.15	15.89 ± 0.13	16.34 ± 0.12
FCC 177	13.88 ± 0.04	12.52 ± 0.01	11.8 ± 0.01	11.44 ± 0.02	31 ± 1	33.9 ± 0.3	35.9 ± 0.2	35.6 ± 0.2
FCC 182	15.66 ± 0.04	14.24 ± 0.01	13.58 ± 0.01	13.21 ± 0.01	12.66 ± 0.05	10.27 ± 0.05	9.90 ± 0.05	9.78 ± 0.06
FCC 184	12.64 ± 0.01	10.76 ± 0.01	10.00 ± 0.04	9.62 ± 0.03	32.26 ± 0.03	36.8 ± 0.01	34.45 ± 0.01	31.17 ± 0.11
FCC 190	14.20 ± 0.06	12.92 ± 0.01	12.26 ± 0.01	11.88 ± 0.01	26.32 ± 0.13	18.98 ± 0.08	18.34 ± 0.08	18.2 ± 0.08
FCC 193	13.09 ± 0.06	11.42 ± 0.01	10.69 ± 0.02	10.25 ± 0.02	28.2 ± 0.3	27.6 ± 0.3	28.2 ± 0.3	32.8 ± 0.4
FCC 213	10.55 ± 0.12	8.57 ± 0.09	7.89 ± 0.09	7.59 ± 0.03	232 ± 2	346 ± 3	308 ± 2	248 ± 2
FCC 219	11.33 ± 0.04	9.28 ± 0.08	8.57 ± 0.04	8.32 ± 0.01	97.47 ± 0.06	201.5 ± 0.1	161 ± 0.2	116.6 ± 0.9
FCC 276	12.52 ± 0.05	10.45 ± 0.06	10.15 ± 0.02	9.81 ± 0.04	56.1 ± 0.5	56.1 ± 0.5	44.67 ± 0.07	42.4 ± 0.3
FCC 277	14.64 ± 0.02	12.74 ± 0.01	12.34 ± 0.02	11.97 ± 0.04	14.45 ± 0.10	12.61 ± 0.05	12.78 ± 0.04	12.61 ± 0.03
FCC 301	15.0 ± 0.1	12.99 ± 0.05	12.65 ± 0.01	12.29 ± 0.03	14.9 ± 0.4	13.7 ± 0.4	11.7 ± 0.3	11.9 ± 0.3
FCC 310	13.0 ± 0.01	12.19 ± 0.05	11.81 ± 0.04	11.41 ± 0.01	63 ± 1	36.3 ± 0.14	35.57 ± 0.02	36.41 ± 0.06

Notes. Column 1: Fornax cluster members from Ferguson (1989). Columns 2–5: total magnitudes in the *u*, *g*, *r*, and *i* band respectively, derived from the isophote fit. Values were corrected for the Galactic extinction by using the absorption coefficient by Schlegel et al. (1998). Columns 6–9: effective radius in the *u*, *g*, *r*, and *i* band respectively, derived from the isophote fit.

all of which are located in the core of the cluster (see Fig. 2). For the remaining four elliptical galaxies (FCC 090, FCC 276, FCC 277, FCC 301), which are at larger cluster-centric radius ($R \geq 0.8-1.0$ deg), the colour profiles show a dip in their inner regions, where colours are bluer ($g-i \sim 0.5$ mag), and they remain almost constant at larger radii. For all these galaxies, the dip starts at a larger radii (∼1.8−6 arcsec) than the regions affected by the seeing (∼1 arcsec). There are no other comparable estimates of the colour distribution available in the literature for the ETGs in the Fornax cluster.

5. Results: a deep look at the Fornax cluster from FDS

In this section, we give a global comprehensive view of the main properties for all bright ETG members inside the virial radius of the cluster, as a function of the environment. We focus, in particular, on the analysis of the deep photometry and large covered area of FDS. Results are discussed in Sect. 6.

According to the pioneering studies of Ferguson & Sandage (1988), half of the bright ETGs inside the virial radius of the Fornax cluster (∼0.7 Mpc) are elliptical galaxies and half of the lenticular (S0) galaxies are barred (see Table 2). Looking at the FDS mosaic in this area (shown in Fig. 2), the ETGs are not homogeneously distributed within the core of the cluster: most of the ETGs are located on the western side of the core, concentrated along a "stripe" in the north-south direction. All S0 galaxies are inside 1.2° (∼0.4 Mpc) from the core of the cluster (see left panel of Fig. 8) and only on the western side (see Fig. 2). Except for FCC310, which is at $R \sim R_{vir}$, all barred galaxies are very close to the core of the cluster, projected inside the stellar halo of NGC 1399 (i.e. ∼0.5°), on the western side. As the total magnitudes derived from FDS confirm, the most luminous elliptical galaxies are close to the cluster centre (see the lower right panel of Fig. 8). Such a trend is not obvious for S0 galaxies (see the middle right panel of Fig. 8) and it seems completely absent for the barred S0 galaxies (see the top right panel of Fig. 8).

The $g-r$ average colours of the ETGs are in the range 0.5–0.8 mag, with a peak around $g-r \sim 0.7$ mag, and there is no significant difference in colours between ellipticals and S0s (see Fig. 9). Both $g-r$ and $g-i$ colours are almost constant ($g-r \sim 0.7$ mag and $g-i \sim 1$ mag) out to ∼1° from the core. At larger cluster-centric distances ETGs tend to be bluer, with $g-r \sim 0.2-0.4$ mag and $g-i \sim 0.6-0.8$ mag (see the left panel of Fig. 10). The colour-density diagram shows that the bluest galaxies are in the lower density regions of the cluster (see top panel of Fig. 11), where $\Sigma \leq 40$ Gal Mpc^{-2} at a distance larger than 0.8°, that is, ∼0.3 Mpc (∼$0.4R_{vir}$) from the cluster centre. The bluest galaxies are the less luminous ($M_i \leq -20$ mag) and less massive objects ($M_* \leq 6.3 \times 10^9\ M_\odot$) of the sample (see the mass-size and colour-magnitude relations in Fig. 12). The massive and reddest galaxies are located in the high-density region of the cluster (see the top panel in Fig. 12), at $R \leq 0.3$ Mpc (∼$0.4R_{vir}$) from the cluster centre. By comparing the X-ray emission with the colour distribution of ETGs inside the cluster (see Fig. 2), it clearly appears that the transition from red to blue colours (at about 0.3 Mpc) corresponds to a decrease in the hot gas density.

5.1. Signs of interaction in the diffuse light

The deep observations, the large covered area, and the optimised observing strategy of FDS allow us for the first time to detect and analyse the faintest structures in the galaxy outskirts and in the intra-cluster area. Figure 13 shows which are the faint features

Table 4. Stellar mass estimates of the ETGs in the *i*-band.

Object	D_{core}	M_r	M_i	R_e	$g-r$	$g-i$	$g-i$ ($R \leq 0.5\,R_e$)	$g-i$ ($R \geq 3\,R_e$)	M_*	M/L
	(°)	(mag)	(mag)	(kpc)	(mag)	(mag)	(mag)	(mag)	$10^{10}\,M_\odot$	
(1)	(2)	(3)	(4)	(5)	(6)	(7)	(8)	(9)	(10)	(11)
FCC 090	1.7	–18.83	–18.06	1.07	0.54 ± 0.05	0.78 ± 0.04	0.62 ± 0.02	0.8 ± 0.1	0.082	0.72
FCC 143	0.76	–18.77	–19.04	0.98	0.07 ± 0.05	0.97 ± 0.09	1.08 ± 0.02	0.8 ± 0.2	0.28	0.99
FCC 147	0.67	–20.96	–21.31	2.29	0.64 ± 0.02	0.99 ± 0.03	1.13 ± 0.01	0.98 ± 0.07	2.4	1.04
FCC 148	0.67	–19.79	–20.02	2.42	0.63 ± 0.02	0.86 ± 0.03	0.92 ± 0.02	0.7 ± 0.3	0.58	0.83
FCC 153	1.17	–19.89	–20.42	2.84	0.24 ± 0.07	0.77 ± 0.07	0.78 ± 0.06	0.77 ± 0.13	0.76	0.74
FCC 161	0.49	–21.02	–21.35	2.60	0.71 ± 0.02	1.04 ± 0.04	1.04 ± 0.04	1.04 ± 0.04	2.63	1.11
FCC 167	0.62	–22.36	–22.8	6.17	0.59 ± 0.03	1.03 ± 0.02	1.19 ± 0.02	1.31 ± 0.11	9.85	1.10
FCC 170	0.42	–20.71	–21.13	1.73	0.65 ± 0.02	1.07 ± 0.02	1.13 ± 0.01	1.07 ± 0.07	2.25	1.17
FCC 177	0.79	–19.71	–20.07	3.45	0.72 ± 0.02	1.08 ± 0.03	1.00 ± 0.02	1.1 ± 0.6	0.85	1.19
FCC 182	0.32	–17.88	–18.25	0.93	0.66 ± 0.02	1.03 ± 0.02	1.09 ± 0.01	1.03 ± 0.15	0.15	1.1
FCC 184	0.31	–21.43	–21.81	2.91	0.76 ± 0.05	1.14 ± 0.04	1.30 ± 0.01	1.34 ± 0.14	4.70	1.31
FCC 190	0.37	–19.28	–19.66	1.79	0.66 ± 0.02	1.04 ± 0.02	1.09 ± 0.01	0.89 ± 0.14	0.54	1.10
FCC 193	0.39	–20.93	–21.38	3.37	0.73 ± 0.03	1.17 ± 0.03	1.12 ± 0.01	1.14 ± 0.06	3.32	1.37
FCC 213	0.0	–23.71	–24.01	25.1	0.7 ± 0.2	0.98 ± 0.12	1.19 ± 0.02	0.8 ± 0.5	27.5	1.0
FCC 219	0.17	–22.95	–23.21	11.4	0.71 ± 0.12	0.96 ± 0.09	1.18 ± 0.01	1.07 ± 0.04	12.7	0.98
FCC 276	0.79	–21.31	–21.65	4.03	0.3 ± 0.08	0.64 ± 0.10	0.81 ± 0.01	0.61 ± 0.15	1.81	0.58
FCC 277	0.86	–19.24	–19.61	1.26	0.4 ± 0.03	0.77 ± 0.05	0.75 ± 0.01	0.76 ± 0.09	0.34	0.72
FCC 301	1.44	–18.82	–19.17	1.14	0.34 ± 0.06	0.70 ± 0.08	0.70 ± 0.05	0.65 ± 0.15	0.20	0.63
FCC 310	2.0	–19.70	–20.10	3.51	0.37 ± 0.09	0.77 ± 0.06	0.76 ± 0.01	0.66 ± 0.07	0.54	0.72

Notes. Column 1: Fornax cluster members from Ferguson (1989). Column 2: projected distance from the galaxy centre (in degrees), i.e. from NGC 1399 (FCC 213). Columns 3 and 4: absolute magnitudes in the *r* and *i* bands. Column 5: effective radius (in kpc) in the *i* band. Columns 6 and 7: average $g-r$ and $g-i$ colours. Columns 8 and 9: average $g-i$ colours for $R \leq 0.5\,R_e$ and for $R \geq 3\,R_e$. Columns 10 and 11: stellar mass and mass-to-light (M/L) in the *i* band.

detected inside the virial radius of the cluster and where they are located.

In previous studies on FDS we detected a faint ($\mu_g \sim 29$–30 mag arcsec^{-2}) stellar bridge, about 5 arcmin long (~29 kpc), in the intra-cluster region on the western side of NGC 1399 and towards FCC 184 (Iodice et al. 2016). An over-density of blue GCs, also based on FDS data, was found in the same region (D'Abrusco et al. 2016), which confirms the ongoing interaction between the two galaxies, where the outer envelope of NGC1387 on its eastern side is stripped away (see also Bassino et al. 2006).

On the western side of the cluster core, we detected several patches of diffuse light in the intra-cluster region (Iodice et al. 2017b). These features are very faint ($\mu_r \sim 28$–29 mag arcsec^{-2} in the *r* band) and extend out to 250 kpc within the core. The most prominent is concentrated between the three bright galaxies in the core, FCC 184, FCC 161, and FCC 170. The spatial distribution of the blue GCs coincides with the intra-cluster patches of light, suggesting that these regions in the core of the cluster are populated by intra-cluster material.

In this work, we have explored a wider region of the cluster at the faintest magnitude levels and we detected a new, quite faint bridge of light $\mu_r \simeq 29.5$ mag arcsec^{-2} between the compact elliptical galaxy FCC 143 and the luminous and larger elliptical FCC 147 (see Fig. 13 and also the top left panel of Fig. B.2), located on western side of the core. The two galaxies are quite close in space (distance differs by 0.3 Mpc Blakeslee et al. 2009), therefore they are likely to be going through an interaction.

By analysing the outskirts of each galaxy of the sample (see Appendix A) at $\mu_g \geq 26$ mag arcsec^{-2}, we found that many of the bright ETGs in the high-density region on the western side of the cluster show an asymmetric stellar envelope, more elongated and twisted in one direction (like FCC 161, FCC 167, FCC 184 shown in Fig. 13). Far away from the cluster centre, there are no other detectable faint structures in the intra-cluster space and the

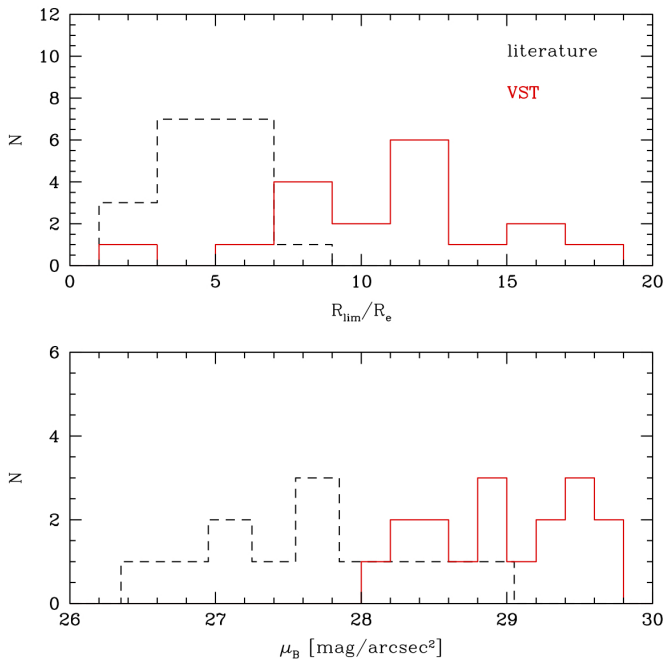

Fig. 5. Comparison of the limiting magnitudes, derived from the surface brightness profiles shown in Appendix B, (*bottom panel*) and effective radii (*top panel*) obtained by the new FDS images (red histograms) and the estimates from previous works (dashed histograms), mainly from Caon et al. (1994).

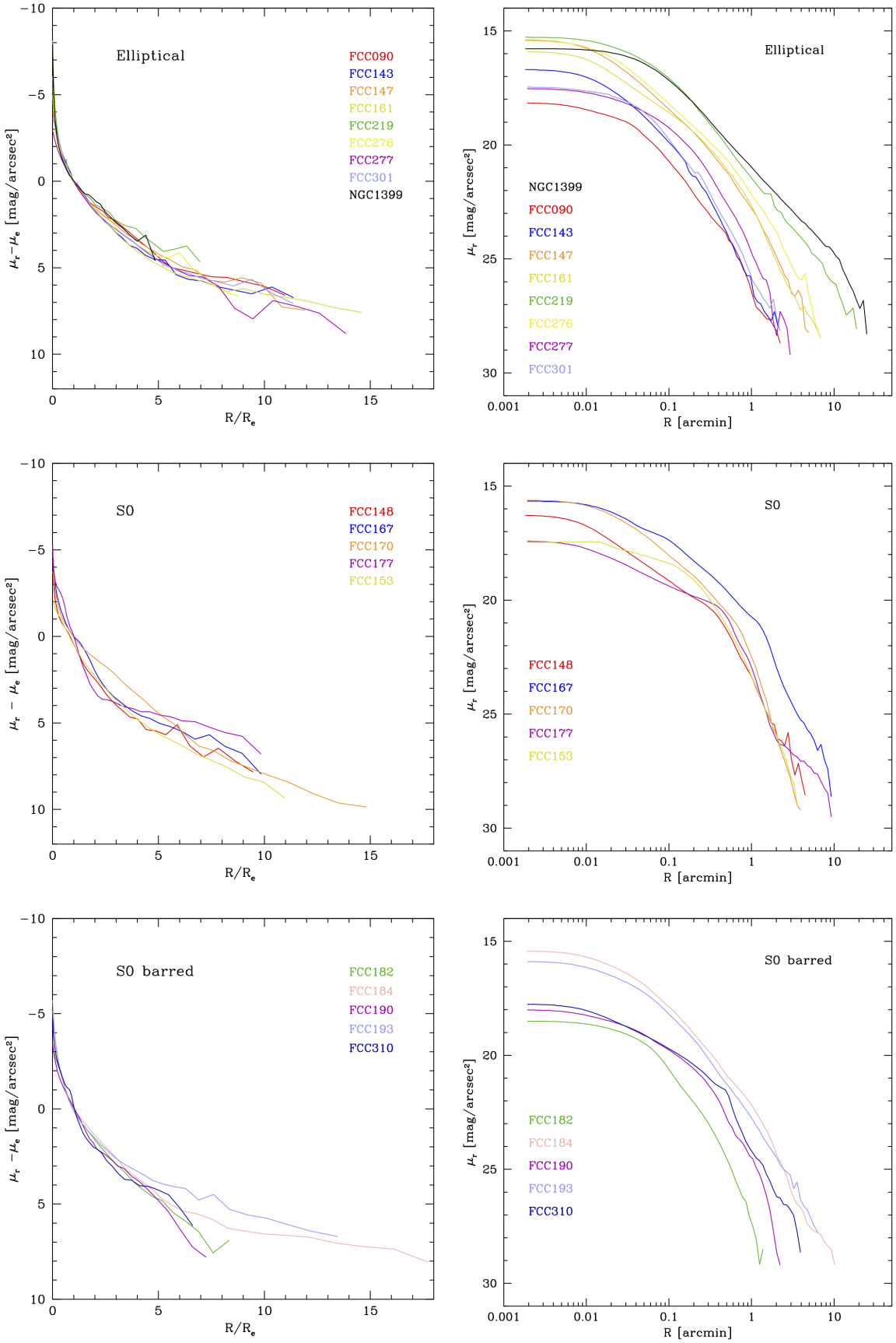

Fig. 6. Azimuthally averaged surface brightness profiles in the r band for elliptical galaxies (*top panels*), S0s (*middle panels*), and barred S0s (*bottom panels*). *Left panels*: linear scale as function of R/R_e , where R_e is the effective radius given in Table 3. *Right panels*: logarithmic scale.

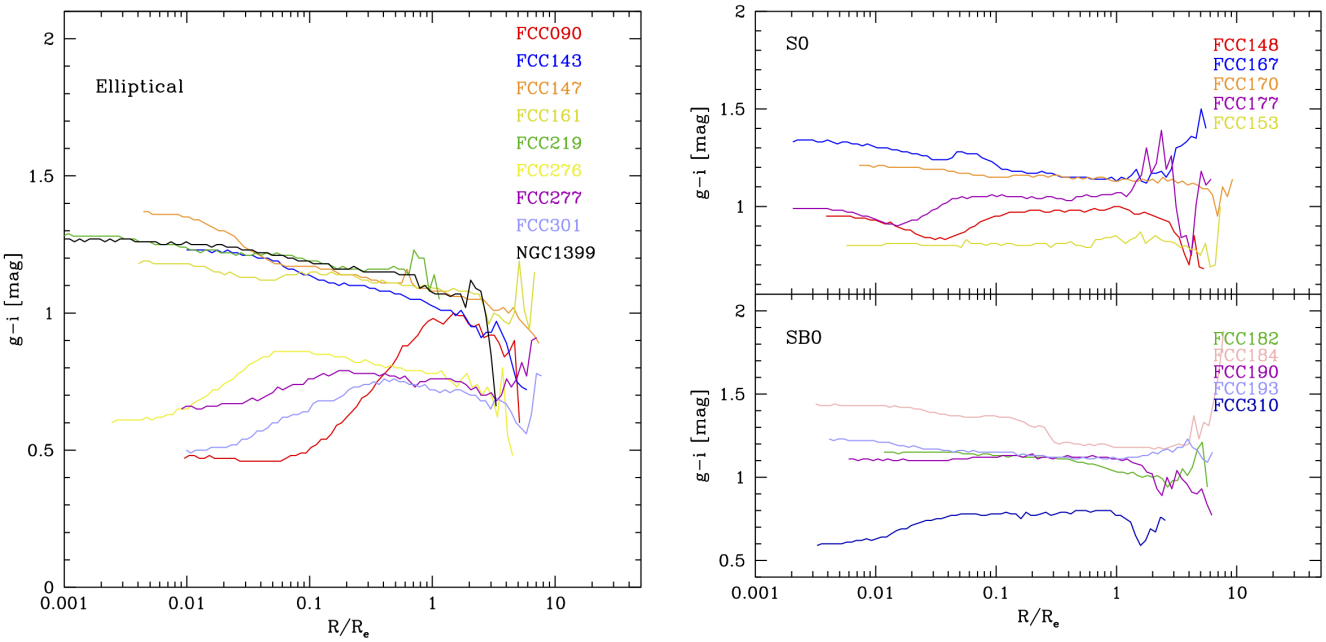

Fig. 7. $g-i$ colour profiles for elliptical galaxies (*left panel*) and normal S0s (*top right panel*) and barred S0s (*bottom right panel*) inside the virial radius of the Fornax cluster.

galaxy outskirts appear more regular than those of galaxies in the high-density region. In summary, signs of interaction in the diffuse light are found on the western side of the cluster, where the galaxy density is highest.

5.2. Colours in the galaxy outskirts

Since the FDS data allow us to map the colour profiles out to $5-10\,R_e$, we derived the average $g-i$ colours in the inner and brightest regions of the galaxies, at $R \leq 0.5\,R_e$ (excluding the seeing disc), and in the outskirts, at $R \geq 3\,R_e$. We found that the colour distribution shows the same trend observed for the average global colours: at larger cluster-centric distances the inner regions of ETGs, as well as the outskirts, tend to be bluer (see the right panel of Fig. 10). This is quite evident for colours inside $0.5\,R_e$, while larger scatter and errors affect the colours in the galaxy outskirts (at $R \geq 3\,R_e$). In the high-density regions of the cluster, the galaxy outskirts are about 0.12 mag bluer than the inner and brightest parts: $g-i = 1.0 \pm 0.2$ mag at $R \geq 3\,R_e$ and $g-i = 1.12 \pm 0.09$ mag at $R \leq 0.5\,R_e$ (see the right panel of Fig. 10). In the low-density regions, the difference is about 0.03 mag compared to the colours of the inner parts, even if it is still within the errors ($g-i = 0.74 \pm 0.07$ mag at $R \leq 0.5\,R_e$ and $g-i = 0.71 \pm 0.08$ mag at $R \geq 3\,R_e$). The colours of the galaxy outskirt reflect differences in stellar populations as a function of the environment and therefore a different process of mass assembly. This point is addressed in Sect. 6.

5.3. Flaring of the discs in the edge-on S0 galaxies

Mapping the light distribution beyond $\mu_r = 27\,\mathrm{mag\,arcsec^{-2}}$, FDS data have revealed the flaring of the disc in the outer and fainter regions of the three edge-on S0 galaxies, FCC 153, FCC 170, and FCC 177, all of them located on the north-western side of the cluster. For the three galaxies, we derived the two-dimensional model from the fit of the isophotes (see Sect. 3) by using the IRAF task BMODEL. The residuals are obtained by subtracting the model from the galaxy image. For all three galaxies, the results are shown in Fig. 14.

The most extended and thickest flaring is detected in FCC 170 (see the middle panels of Fig. 14), since it reaches a distance of 1.7 arcmin from the galaxy centre and an height of 0.5 arcmin at $\mu_r \sim 29\,\mathrm{mag\,arcsec^{-2}}$. The flaring in FCC 153 has a similar morphology and spans a comparable surface brightness range to that in FCC 170. It is less extended ($R \sim 1.3$ arcmin) but it is as thick as that in FCC 170, since the height is ~0.5 arcmin at $\mu_r \sim 29\,\mathrm{mag\,arcsec^{-2}}$ (see the top panels of Fig. 14). With a quite different shape and luminosity from the previous ones, the flaring in FCC 177 appears thin and more luminous close to the galaxy centre, with $\mu_r \sim 23\,\mathrm{mag\,arcsec^{-2}}$ at ~0.5 arcmin. At larger radii (~1 arcmin) at $\mu_r \sim 27\,\mathrm{mag\,arcsec^{-2}}$, the maximum thickness is only ~0.2 arcmin (see the lower panel of Fig. 14).

The $g-i$ colour maps, which are model-independent, also show a flaring structure for the disc in each object (see Fig. C.2). For FCC 153 and FCC 177 they are quite evident from the colour map, even if the flaring has different colour distributions: FCC 153 shows bluer colours ($g-i \sim 0.8$ mag, see also Sect. A.5) at large radii, while FCC 177 shows a dip in the colour distribution ($g-i \sim 0.9$ mag) in the regions of the light peak at ~0.5 arcmin, and red colours ($g-i \sim 1.1$ mag) at larger radii (see also Sect. A.9). The flaring in the disc of FCC 170 is less pronounced in the colour map, which is dominated by a central red ($g-i \sim 1.2$ mag) and thin disc. In the outer region it appears thicker and bluer ($g-i \sim 1$ mag, see also Sect. A.8).

The two-dimensional stellar kinematics and stellar population analysis of FCC 170 from the Fornax3D (F3D) project with MUSE (Sarzi et al. 2018) reveal the presence of a fast-rotating and flaring thin disc and a slower rotating thick disc in this galaxy (Pinna et al. 2019). Preliminary results from the F3D survey for the other two galaxies, FCC 153 and FCC 177, also confirm the existence of a flaring disc (Pinna et al., in prep.). Different morphology, luminosities, and colours suggest a different origin for the flaring of the disc in each galaxy (see discussion in Sect. 6).

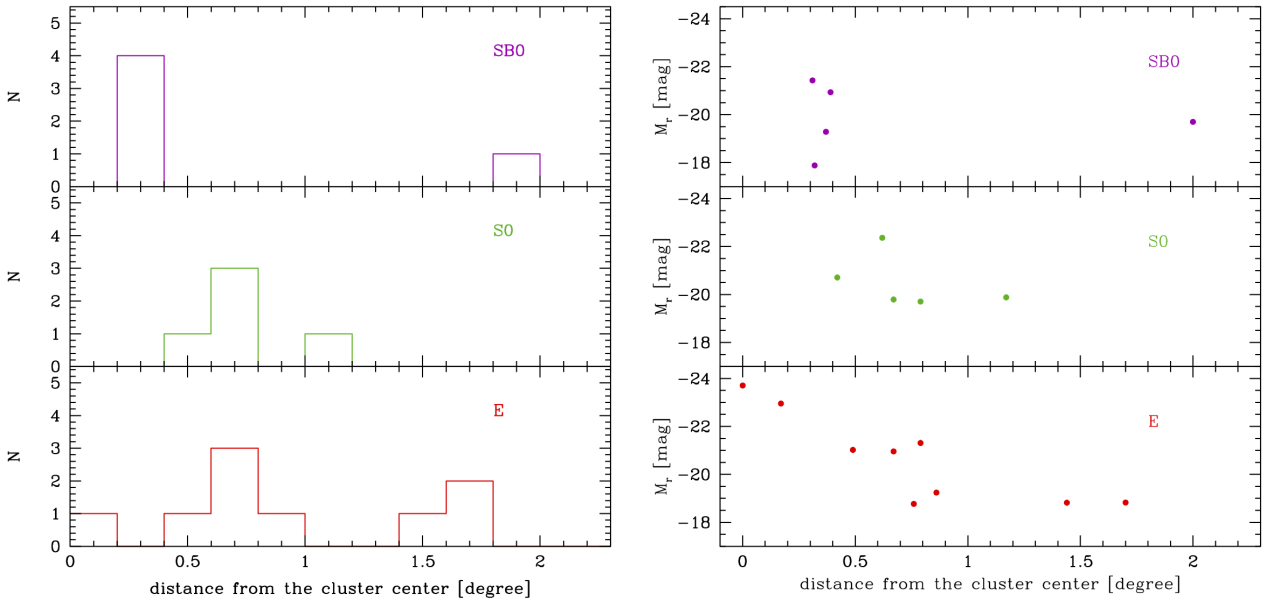

Fig. 8. Distribution (*left panel*) and absolute magnitude in the *r* band (*right panel*) of ETGs (barred S0 in the top panel, normal S0 and elliptical galaxies in the *middle and bottom panels*, respectively) inside the virial radius as function of the projected distance from the cluster centre.

6. Discussion

This paper is based on FDS data and it focuses on the bright ETGs galaxies ($m_B \leq 15$ mag) inside the virial radius of the Fornax cluster ($R_{vir} \sim 0.7$ Mpc). For all galaxies of the sample (given in Table 2), we analysed the light and colour distribution in all OmegaCam filters, *ugri* (see Sect. 3). A detailed description of the results for each galaxy is provided in Appendix A. The deep images and the colour maps are given in Appendices B and C, respectively. In this work we release the main data products resulting from the surface photometry[9] in all OmegaCam filters, *ugri* (i.e. total magnitudes, effective radii, integrated colours, and M/L ratios) for all the bright ETGs galaxies in the sample (see Tables 3 and 4).

Taking advantage of the multi-band deep observations, the large field of view of OmegaCam at VST, and the optimised observing strategy, the main contribution of this work to the previous science on the Fornax cluster is tracing with great detail the structure of galaxies and colour gradients, out to the largest galactocentric radii reached compared to previous studies (up to about 10−15 R_e) and beyond $\mu_r = 27$ mag arcsec^{-2} ($\mu_B \geq 28$ mag arcsec^{-2}, see Fig. 5). Therefore, in addition to the previous study by Ferguson & Sandage (1988), which presented the morphologies and luminosity function of the galaxies in the Fornax cluster inside a radius of 2.4°, from FDS we are able to map the faint outskirts of galaxies and the intra-cluster space over a comparable area (∼2°).

Below, we summarise the main results and we give a global comprehensive view of the galaxy structure and cluster properties based on them.

1. All signs of interactions between galaxies, in the form of faint ($\mu_r \sim 29$ mag arcsec^{-2}) bridges of stars connecting galaxies, diffuse patches of ICL, and disturbed galaxy envelopes are located in the high-density region of the cluster (≤0.3 Mpc) on the western side. In particular, we found that many of the bright ETGs in the high-density region on the western side of the cluster show an asymetric and elongated stellar envelope, which is twisted in one direction (like FCC 161, FCC 167, FCC 184, FCC 190). In the intra-cluster region, the new feature detected from the FDS data is a very faint bridge of light $\mu_r \simeq 29.5$ mag arcsec^{-2} between the compact elliptical galaxy FCC 143 and the luminous and larger elliptical FCC 147. This new intra-cluster patch of light is added to the other two detected in the core of the cluster in previous FDS studies. Figure 13 shows most of these features.

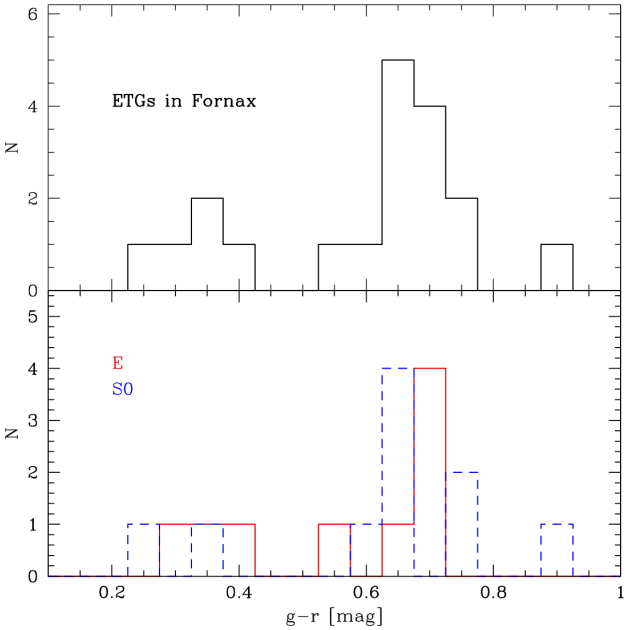

Fig. 9. Average *g*−*r* colour distribution of ETGs inside the virial radius of the Fornax cluster. The *g*−*r* average colour for elliptical and S0 galaxies is plotted in the bottom panel.

[9] The tables and the profiles resulting from the isophote fit (i.e. surface brightness, ellipticity, and PA profiles) given in the present paper will be available in the CDS database. The reduced FDS images for the whole FDS area will be released by the team later in 2019.

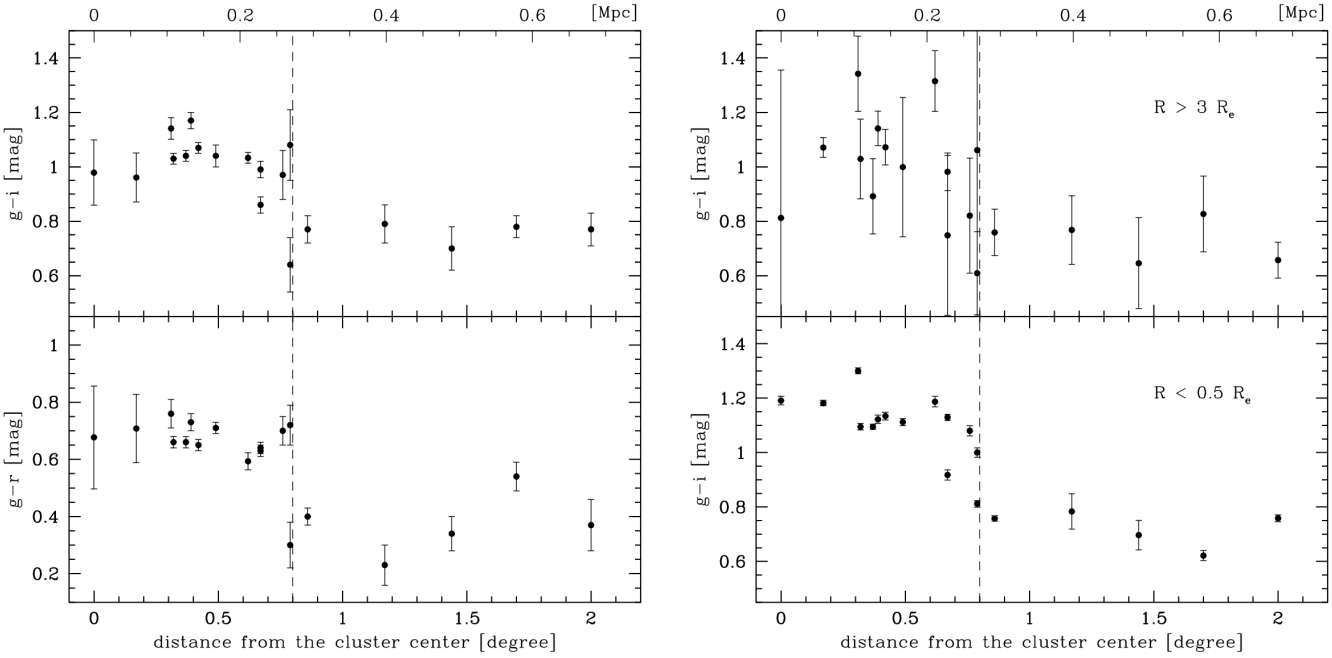

Fig. 10. *Left panel*: $g-r$ (*bottom panel*) and $g-i$ (*top panel*) average colours of ETGs inside the virial radius of the Fornax cluster as a function of the projected distance from the cluster centre. *Right panel*: $g-i$ average colours derived in the inner parts for $R \leq 0.5\,R_e$ (*lower panel*), and in the galaxy outskirts at $R \geq 3\,R_e$ (*top panel*). The dashed line in each panel indicates the transition radius from the high-density to low-density regions of the cluster, at $R = 0.8^\circ = 0.27$ Mpc ($\sim 0.4 R_{\rm vir}$).

2. The outskirts (at $R \geq 3\,R_e$) of galaxies located in the high-density region of the cluster have redder colours ($g-i = 1.0 \pm 0.2$ mag) than the outskirts of cluster members in the low-density region ($g-i = 0.71 \pm 0.08$ mag).
3. For the three edge-on S0 galaxies of the sample (FCC 153, FCC 170, and FCC 177), the disc is flaring in the outer and fainter regions, down to $\mu_r \sim 29$ mag arcsec^{-2}.

6.1. The building-up of the Fornax cluster

Inside the virial radius, the ETGs of the Fornax cluster are not uniformly distributed in space around the core: most of the ETGs are located on the western side of NGC 1399, concentrated along a "stripe" in north-south direction (see Fig. 2). All S0 galaxies are inside 1.2° (~0.4 Mpc) from the centre of the cluster (see left panel of Fig. 8) and only on the western side (see Fig. 2). Few elliptical galaxies are found on the eastern side at larger projected distances ($\geq 1.5^\circ \sim 0.5$ Mpc), which are fainter and bluer than the elliptical galaxies in the core, and show nuclear substructures. This difference might suggest a different formation and/or evolution process for the galaxies in the two regions of the cluster.

The W-NW sub-clump may result from the accretion of a group of galaxies during the gradual build-up of the cluster, which induced this evident asymmetry in the spatial distribution of bright galaxies. Since groups of galaxies host different types of galaxies, the accretion of a group onto a cluster contributes to a large range of luminosities and morphologies (Tully & Trentham 2008). Galaxy interactions and merging are more frequent in groups than in clusters due to a lower velocity dispersion in the former (Tremaine 1981), therefore the galaxy cluster members accreted as part of groups can undergo a pre-processing that has modified their structure and internal dynamics. Vijayaraghavan & Ricker (2013) found that a sudden burst of enhanced ram pressure occurs when the group passes the pericentre of the cluster. Simulations show that the tidal interactions induce a decrease in rotational support and a thickening of the stellar structure (Toomre & Toomre 1972; Bialas et al. 2015; Smith et al. 2015). This would explain the high fraction of early-type systems in the W-NW sub-clump of the Fornax cluster.

The different morphology and colours of the flaring observed in the three edge-on S0s of the sample (FCC 153, FCC 170, and FCC 177, see Sect. 5.1) and the presence of a thick disc in FCC 170 (see also Pinna et al. 2019), which is in the core of the sub-clump and close to the core of the cluster, could be reconciled with different kinds of interactions. During the infalling of a group in a cluster, the field late-type galaxies could be swept up and interact for a short time with the galaxies in the group before becoming cluster members (Vijayaraghavan & Ricker 2013). In this process, these galaxies experience ram pressure stripping and appear as S0 galaxies. Boselli & Gavazzi (2006) also addressed the origin of lenticular galaxies induced by the gravitational interactions in infalling groups. Due to the interaction with the hot and dense intra-cluster medium, the late-type galaxies (LTGs), after several crossing times, were depleted of the gas supply, lost their angular momentum and have a possible heating of the stellar disc. Therefore, LTGs will result in disc-dominated and quiescent galaxies, similar to S0s. With the help of simulations, Boselli et al. (2006) showed that the gas stripping in the disc galaxies, caused by the interaction with the intra-cluster medium, is reflected in the colour gradients. By studying the colour profiles of the spiral galaxy NGC 4569 in the Virgo cluster, these authors found an inversion in the colour profiles that appear redder in the outer disc and bluer towards the centre. FCC 177, to the north in the Fornax cluster, could be one example of this mechanism, since it shows a different structure with respect to the other edge-on S0s in Fornax (see Sect. 5.1 and Appendix A). This galaxy shows an extended thin disc ($R \leq 2$ arcmin and $\mu_r \sim 20-27$ mag arcsec^{-2}),

bluer in the inner regions, thicker and redder in the outer parts (see Fig. C.2). FCC 177 could be the result of a early-type spiral galaxy that has lost the cold gas and is evolving into an S0 galaxy.

6.2. Growth of bars

We have reported that all barred galaxies are very close to the core of the cluster (i.e. ∼0.5°), on the western side (see Sect. 5). This is consistent with predictions from N-body simulations, which found that tidal interactions trigger bar formation in a cluster core, rather than in the outskirts or in isolation, causing therefore a larger fraction of barred galaxies toward the cluster centre (Łokas et al. 2016; Martinez-Valpuesta et al. 2017). In a Virgo-like cluster, simulations show that a bar forms at the first pericentre passage of a disky galaxy and survive many giga years after the bar formation. Moreover, a pronounced boxy or peanut shape could appear in those galaxies that undergo stronger tidal forces (Łokas et al. 2016; Martinez-Valpuesta et al. 2017). This would be the case of FCC 148 (see Fig. A.4).

6.3. Region of tidal interactions

From the observational side, the deep FDS data further confirm that the bulk of the gravitational interactions between galaxies happened on the W-NW sub-clump of the cluster. In fact, this is the only region of the cluster, inside the virial radius, where the intra-cluster baryons (diffuse light and GCs) are found, that is, the bridge between NGC 1399 and FCC 184 (Iodice et al. 2016), the intra-cluster light and GCs between FCC 184, FCC 170, and FCC 161 (Iodice et al. 2017b), and the new faint filaments between FCC 143 and FCC 147 (see Sect. 5.1 and Fig. 13). The gravitational interactions could have also modified the structure of the galaxy outskirts and produced the intra-cluster baryons. Compared with simulations by Rudick et al. (2009), the diffuse form observed for the ICL is consistent with the scenario where this component formed by stripped material from the outskirts of a galaxy in a close passage with the cD (Iodice et al. 2017b). In this area of the cluster, the stellar envelope of some ETGs is asymmetric, appearing more elongated and twisted in one direction, while the outskirts of galaxies at larger distances from the cluster centre have a more regular shape. Mastropietro et al. (2005) show how harassment can induce twists in the outer isophotes of dwarf galaxies. More massive and luminous galaxies, like the elliptical galaxies in this region of the Fornax cluster, have a deeper potential well, therefore the stripping of stars by harassment implies even stronger tidal forces. A disturbed morphology in galaxy outskirts could also result from the ongoing accretion of smaller satellites. Simulations on the mass accretion and stellar halo formation for different stellar masses (10^{10}–$10^{13}\,M_{\odot}$) show that the outskirts of galaxies (for $\mu_r \sim 27$–31 mag arcsec^{-2}) appear with a quite disturbed morphology and with an overall elongated shape (Michel-Dansac et al. 2010; Cooper et al. 2015; Monachesi et al. 2018). The structure of the stellar envelope, as well as the shape of the SB profile, depends on the mass and number of the accreted progenitors. The ETGs showing asymmetric and diffuse envelopes (FCC 161, FCC 167, FCC 184, see Sect. 5.1 and Fig. 13) are in range of stellar mass (~ 3–$10 \times 10^{10}\,M_{\odot}$) comparable with simulations and they could still build up their envelope. As noticed by Iodice et al. (2017b), a fraction of the ICL population in this region of the cluster could also come from lower mass dwarf galaxies that are tidally disrupted in the potential well of the massive galaxies, which are therefore contributing to the mass assembly in their halo.

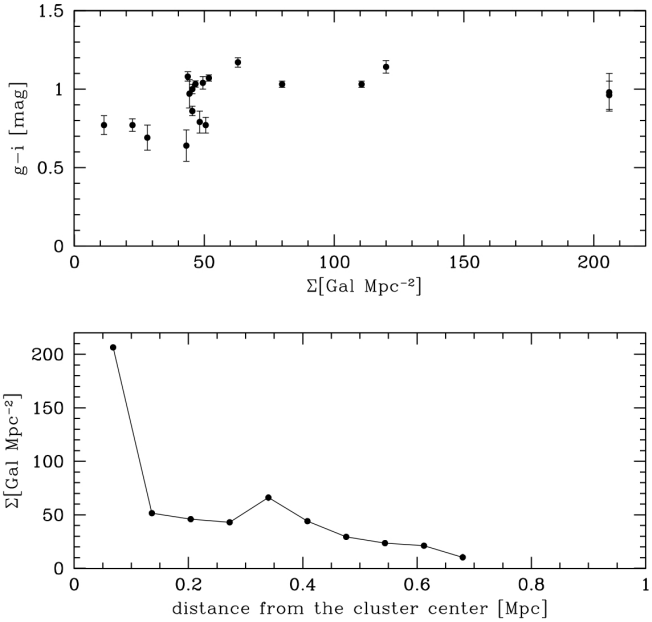

Fig. 11. Colour-density diagram (*top panel*) of the ETGs inside the virial radius of the Fornax cluster as a function of the cluster density Σ. The cluster density as a function of the projected distance from the cluster centre in megaparsec is shown in the *lower panel*. This is derived in circular annuli with bin of 0.2° (out to 2°), accounting for all cluster members given by Ferguson (1989).

This is further supported by a recent study from Venhola et al. (2017), based on FDS data, that found a drop in the number density of LSB galaxies at cluster-centric distances smaller than ∼180 kpc.

6.4. Colour segregation inside the cluster

We have found that the galaxies in the W-NW sub-clump of the cluster have redder colours than galaxies at larger cluster-centric radii. This sub-clump of reddest galaxies makes the greatest contribution to the galaxy density ($\Sigma \geq 40$ Gal Mpc^{-2}, see Fig. 11), inside 0.3 Mpc (∼0.5 $R_{\rm vir}$), and they are the most luminous ($M_i \leq -20$ mag) and massive $M_* \geq 10^{10}\,M_{\odot}$ objects of the sample (see Fig. 12). Similar colour segregation was found by Kodama et al. (2001) for the Abell 851 cluster at $z \sim 0.4$ and also by Aguerri et al. (2018) for the nearby ($z \sim 0.05$) cluster Abell 85, which is considered a strong indication of environmental influences on the galaxy evolution.

The transition from redder to bluer ETGs, at a projected distance of ∼0.8° from the cluster centre (see Fig. 10), coincides with the decrease of the X-ray emission (see Sect. 5 and Fig. 2). This might confirm that the reddest and most massive galaxies in the high-density region of the cluster, where the X-ray emission is still detected, have been depleted of their gas content by processes such as harassment or suffocation induced by ram pressure stripping, so the star formation stopped earlier than for the galaxies in the low-density regions of the cluster. In fact the ROSAT data have shown that the Fornax X-ray halo is composed of several components whose centroids are offset with respect to the optical galaxies. This is likely due to the sloshing movement of NGC 1399 and other bright ellipticals within the central dark matter halo traced by the X-ray gas (Paolillo et al. 2002; Sheardown et al. 2018) combined with the infall of the NGC 1316 group into the cluster, where the collisional component (e.g. the hot gas) is lagging behind the non-collisional ones

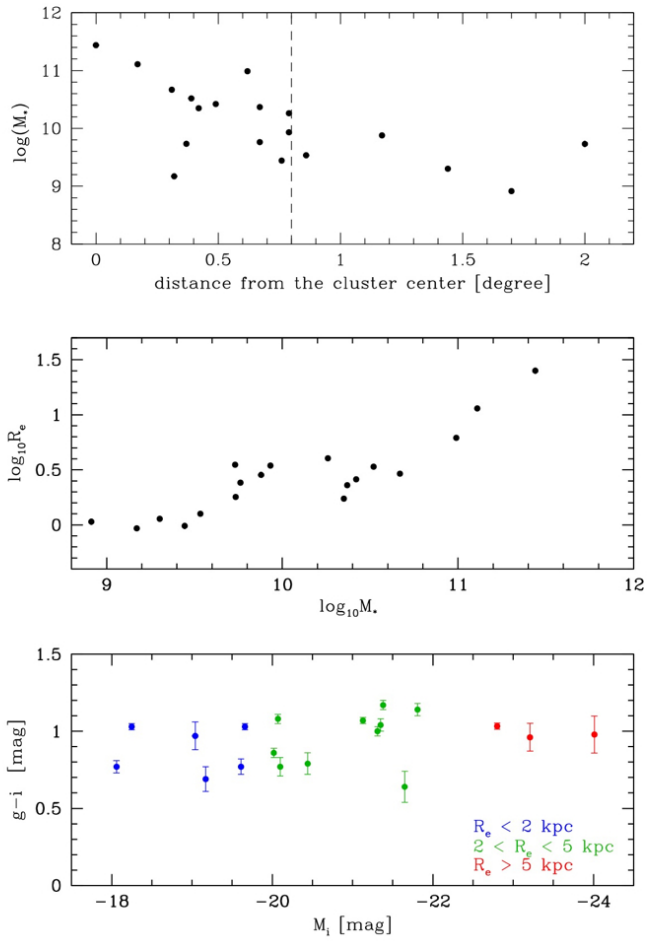

Fig. 12. Mass-size (*middle panel*) and colour-magnitude (*lower panel*) relations for the ETGs inside the virial radius of the Fornax cluster. Different colours are for galaxies in different ranges of the effective radius (values are listed in Table 4). *Top panel*: stellar mass as a function of the cluster-centric radius. The dashed vertical line corresponds to the transition radius 0.8° from the high-density to the low-density regions of the cluster.

(e.g. stars, GCs, and galaxies) due to ram pressure effects. These results seem confirmed by recent XMM observations presented in Su et al. (2017).

The dependence of the colours on the local density suggests a decrease of the star formation rate in galaxies from low- to high-density regions of the cluster. According to the observational evidence given above, there is a strong indication that the star formation in galaxies in the W-NW sub-clump, which are the reddest objects, was quenched due to external interactions (environmental quenching). The few galaxies in the low-density regions of the cluster, uniformly distributed inside the virial radius, have bluer colours, which could mean that they contain, on average, a younger stellar population and therefore they were able to continue forming stars. In any case, since the bluest galaxies in Fornax are also the least massive, the colour segregation could also result from the mass-metallicity relation, where low-mass galaxies in the outer part of the cluster would have a blue colour due to their lower metallicity (Peng et al. 2010, 2015). This issue needs more investigation, in particular, with the help of spectroscopic data, the metallicity and the age of the stellar populations should be derived for each galaxy of the sample in order to study how they change as a function of the cluster-centric radius.

6.5. Mass assembly in the galaxy outskirts

The deep FDS data allow us to map the colours out to the galaxy outskirts ($R \leq 5{-}10\,R_e$) and we have found that they are red in the galaxies located in the high-density region of the cluster compared to those measured in the outskirts of the galaxies in the low-density regions. The differences in colours in the outskirts of galaxies can reflect differences in stellar populations as a function of the environment, and therefore reflect a different process of mass assembly. Simulations show that galaxies with a low fraction of accreted mass in the stellar halo have a steeper metallicity gradient, while a high fraction of accreted mass tends to flatten the metallicity gradient (Cook et al. 2016). Therefore, the blue colours in the outskirts of the galaxies in the low-density regions of the cluster may suggest a lower fraction of the accreted mass with respect to the galaxies in the high-density regions. Also different progenitors can be responsible for differences in colours and metallicities: in the dense regions of the Fornax cluster, the build-up of the stellar halos could result from the accretion of rather massive, metal-rich satellite galaxies, whereas blue colours in the outskirts only allow for the contribution of minor mergers. The estimate of the stellar halo mass fraction in the bright ETGs of the Fornax cluster will be addressed and discussed in a forthcoming paper (Spavone et al., in prep.). A direct measure of the age and metallicity can be done by using spectroscopic data available for all galaxies of the sample (Sarzi et al. 2018) out to the regions of the galaxy outskirts. Results can be directly compared with theoretical predictions.

6.6. How does Fornax compare with nearby clusters?

Compared to the other nearby (<20 Mpc) massive Virgo cluster, Fornax has generally been considered as a classic example of a virialized cluster for its more regular galaxy distribution, high fraction of early-type systems, and lower velocity dispersion (Grillmair et al. 1994; Jordán et al. 2007). The new deep observations of the Virgo cluster, which detected many other new patches of ICL and tidal streams between galaxies (Mihos et al. 2017), have confirmed that it is a dynamically young and unrelaxed cluster. The deep FDS data brought to light the previously unknown intra-cluster baryons (ICL and GCs), including streams of stars between galaxies. These are all detected in the western side of the cluster, between the sub-clump and the cluster core. Outside this region, but inside the virial radius, the deep FDS data do not show any other significant sign of gravitational interactions. We suggest that the build-up of the cluster is still in process, with the W-NW group entering into the cluster, and we demonstrate how this mechanism is important in generating ICL. Compared to Virgo, Fornax hosts ~300 galaxies with $B_T \sim 18$ (Ferguson 1989), which is an order of magnitude lower than the galaxy population in Virgo, mostly concentrated inside 0.3 Mpc from the core. The situation is different in Virgo where there are at least three main sub-groups dominated by the giant ETGs M87, M84, and the south sub-clump around M49 (Binggeli et al. 1987). Therefore, in Fornax we expect to find the peak of the gravitational interactions in the core, as detected in the FDS data. In Virgo, the bulk of the projected ICL is found in the core around M87 and in the adjacent region including M86/M84, and there is evidence of an extensive ICL component in the field around M49 (Mihos et al. 2017). Like Fornax, also the Coma cluster was considered a virialised and evolved large-scale structure, given its spherical symmetry and compactness (Zwicky 1957; Kent & Gunn 1982; Mellier et al. 1988). To

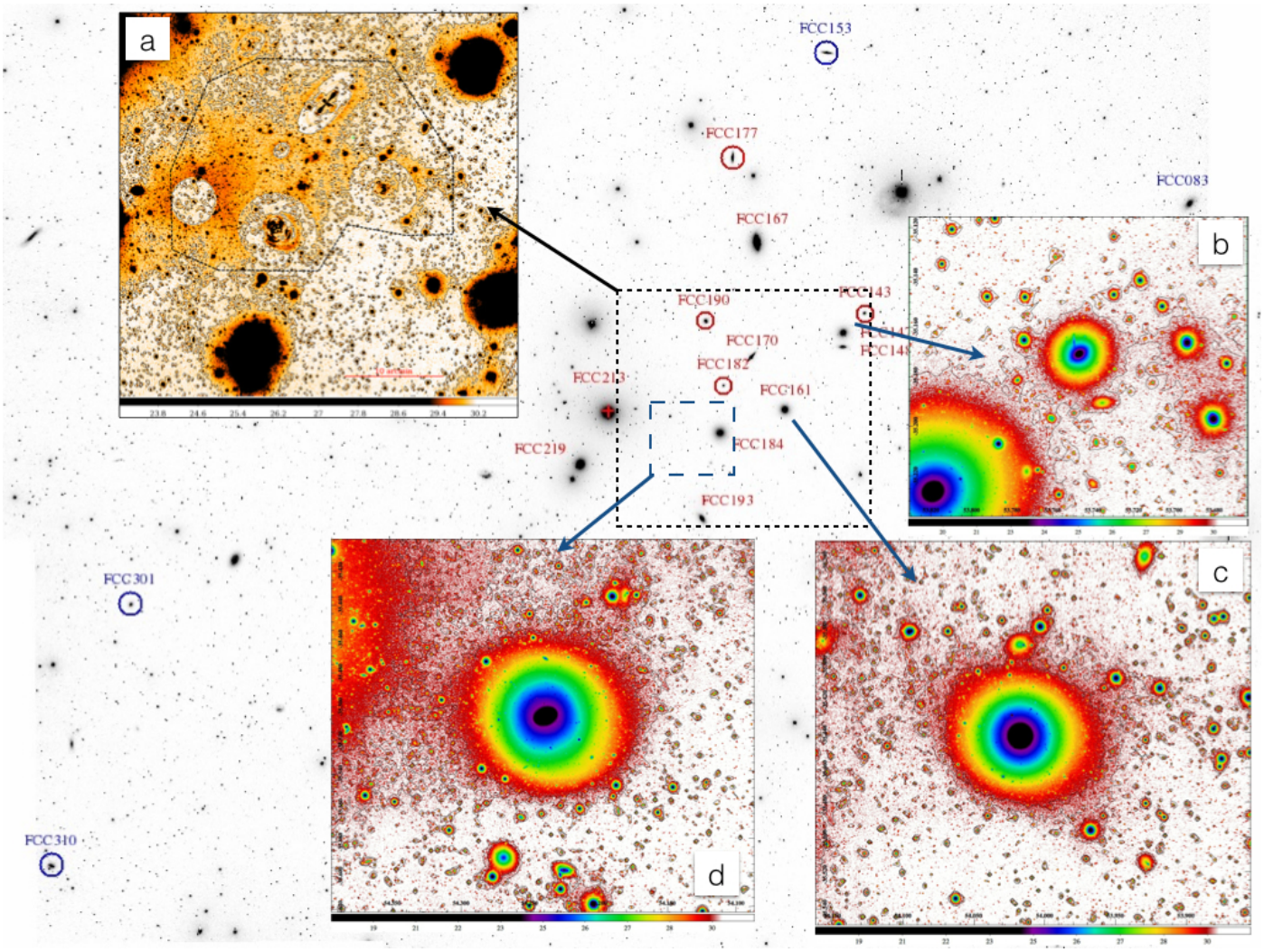

Fig. 13. Diffuse intra-cluster light in the Fornax cluster. *Panel a*: intra-cluster light detected in the core of the cluster by Iodice et al. (2017b). *Panels c and d*: asymmetric stellar halos in FCC 184 and FCC 161. *Panel d*: stellar bridge between NGC 1399 and FCC 184 detected by Iodice et al. (2016). *Panel b*: diffuse light detected between FCC 147 and FCC 143, on the north-western side of the cluster.

date, Coma also appears in a more dynamical active phase. As observed in Fornax, the ICL distribution is more elongated in one direction (toward the east) and over a common envelope between the two giant galaxies in the core (Jiménez-Teja et al. 2019). It is dominated by younger and low-metallicity stars, suggesting that this component could be formed by the stripping of stars from the galaxy outskirts and/or the disruption of dwarf galaxies during merging (see Jiménez-Teja et al. 2019, and references therein).

The hot gas in the Fornax cluster is four times less massive than in Virgo (Schindler et al. 1999; Paolillo et al. 2002; Scharf et al. 2005). This suggests that the role of ram pressure stripping is lower in Fornax than in Virgo, as also found from predictions by Davies et al. (2013), who estimated that the ram pressure stripping is about 16 times less important in Fornax than in Virgo. FDS data have shown that the galaxies in the low-density regions do not show detectable signs of tidal interactions as found in the cluster core; also the outskirts are quite regular in shape. Therefore, in these regions, ram pressure stripping could have been the main process that stopped the star formation in the galaxy outskirts, while it continued in the inner regions (see Sect. 5). The effect of ram pressure stripping on the Fornax cluster members is addressed in the analysis of the ALMA data (Zabel et al. 2019) and in a forthcoming paper from the FDS data on the late-type galaxies (Raj et al., in prep.).

7. Conclusions and future perspectives

The outskirts of galaxies are the least bound, so they are most sensitive to being tidally disturbed (Smith et al. 2016), as well as being affected by the ram pressure, which acts on the gas from the outside inwards, first stripping the outer disc and later reaching the inner disc with increasing ram pressure. Therefore, by studying the very faint outer parts of galaxies it is possible to map the regions where they are most sensitive to environmental effects. Inside the virial radius of the Fornax cluster, the deep FDS data permit the analysis of the light and colour distribution of the ETGs down to the faintest magnitudes ever reached, where the relics of the past gravitational interactions reside.

Such a study has provided strong constraints for the formation history of the Fornax cluster. It has provided strong constraints on the formation and evolution of the galaxies in the cluster and on the possible environmental mechanisms that have played a major role. Observations suggest that the Fornax cluster is not completely relaxed inside the virial radius. The bulk of the gravitational interactions between galaxies happened in the

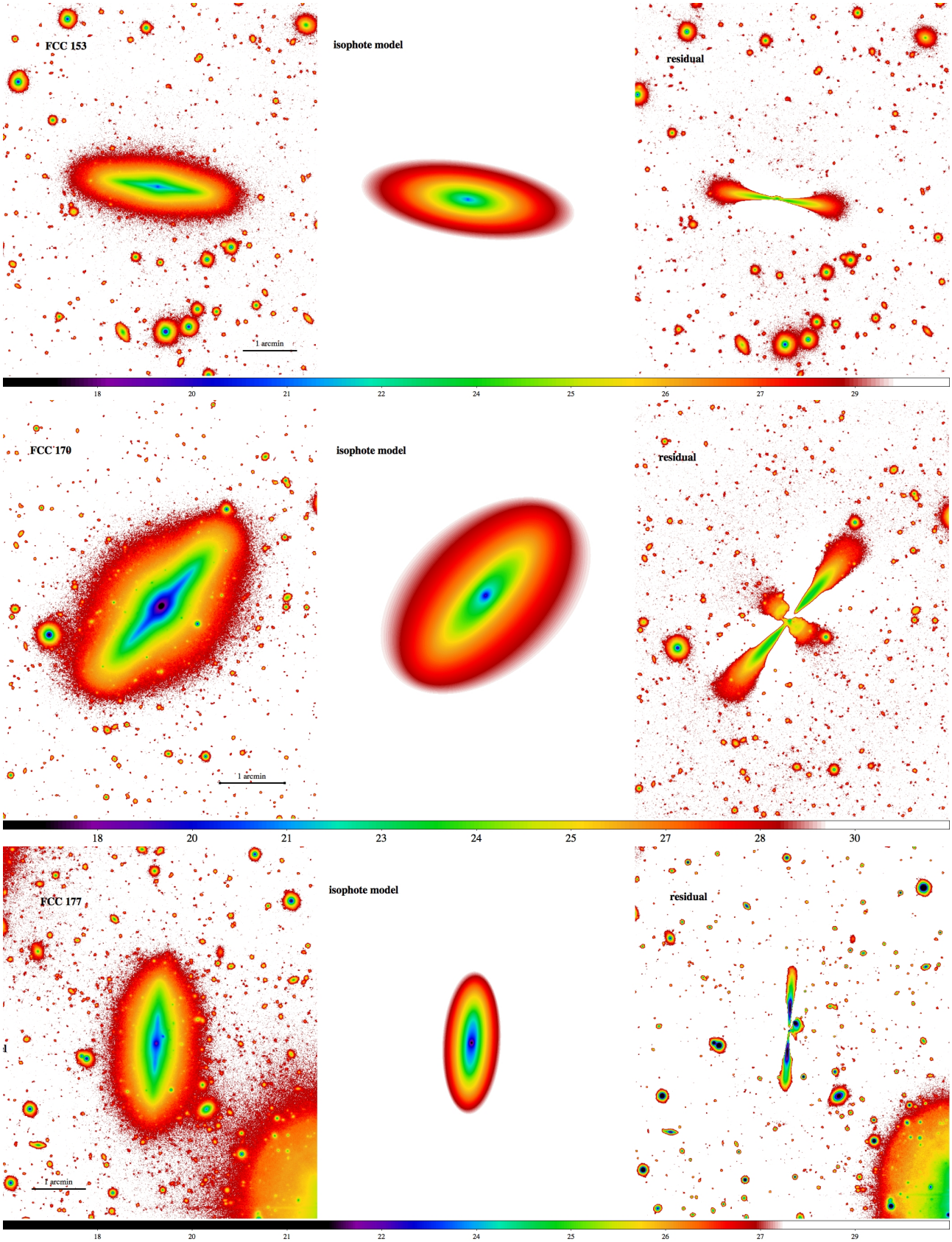

Fig. 14. Results from the isophote fits for the three S0 edge-on galaxies of the sample: FCC 153 (*top panels*), FCC 170 (*middle panels*), and FCC 177 (*lower panels*). For each galaxy, the *r*-band VST image is shown in the *left panels*, the two-dimensional models and residuals are shown in the *middle* and *right panels*, respectively. Images are in surface brightness levels with values reported in the colour bar.

W-NW core region of the cluster, where most of the bright early-type galaxies are located and where the intra-cluster baryons (diffuse light and GCs) are found. We suggest that the W-NW sub-clump of galaxies results from the accretion of a galaxy group, which has modified the structure of the galaxy outskirts (making asymmetric stellar halos) and has produced the intra-cluster baryons (ICL and GCs), concentrated in this region of the cluster.

Future works on FDS data will extend the analysis presented in this paper to all galaxies in the FDS over ∼26° of Fornax, including late-type galaxies. In particular, in a forthcoming paper, for all ETGs in our sample we will present the fit of the light distribution in order to estimate the structural parameters, deriving from them a quantitative morphological classification, and asses the stellar halo mass fraction to be compared with the theoretical predictions (Spavone et al., in prep.). The same kind of analysis is underway for the late-type galaxies (LTGs) inside the same area (Raj et al., in prep.). Moreover, we aim at mapping the colour gradients as function of the mass and cluster-centric radius out to the regions of the stellar halos in order to constrain the age and metallicities of the stellar populations and the importance of the accreted satellites during the mass assembly process (see e.g. La Barbera et al. 2012).

Auxiliary spectroscopic data, available for all ETGs inside the virial radius (Sarzi et al. 2018), will further constrain the star formation rate, age, and metallicity of the galaxies and their stellar halos. By taking advantage of kinematics and dynamical modelling, one could investigate the galaxy structure and, in particular, the nature of the disc flaring, since this could also naturally happen for galaxies in isolation as a result of weaker restoring force at larger distances (Narayan & Jog 2002) and a thick disc might not be the result of a dynamical heating (Brook et al. 2012).

Therefore, FDS data represent a mine to study the galaxy structure from the brightest inner regions to the faint outskirts, including the intra-cluster regions, and the evolution as a function of the cluster-centric radius. The deep observations can be directly compared with predictions from galaxy formation models also in relation with environment.

Acknowledgements. This work is based on visitor mode observations collected at the European Organisation for Astronomical Research in the Southern Hemisphere under the following VST GTO programs: 094.B-0512(B), 094.B-0496(A), 096.B-0501(B), 096.B-0582(A). The authors thank the anonymous referee for his or her suggestions that enabled us to significantly improve the paper. E.I. wishes to thank the ESO staff of the Paranal Observatory for their support during the observations at VST. E.I. and M.S. acknowledge financial support from the VST project (PI P. Schipani). E.I. is also very grateful to T. de Zeeuw and F. La Barbera for the discussions and suggestions on the present work. J. F-B. acknowledges support from grant AYA2016-77237-C3-1-P from the Spanish Ministry of Economy and Competitiveness (MINECO). GvdV acknowledges funding from the European Research Council (ERC) under the European Union's Horizon 2020 research and innovation programme under grant agreement No 724857 (Consolidator Grant ArcheoDyn). NRN and EI acknowledge financial support from the European Union Horizon 2020 research and innovation programme under the Marie Skodowska-Curie grant agreement n. 721463 to the SUNDIAL ITN network.

References

Aguerri, J. A. L. 2016, A&A, 587, A111
Aguerri, J. A. L., Iglesias-Paramo, J., Vilchez, J. M., & Muñoz-Tuñón, C. 2004, AJ, 127, 1344
Aguerri, J. A. L., Agulli, I., & Méndez-Abreu, J. 2018, MNRAS, 477, 1921
Arnaboldi, M., & Gerhard, O. 2010, Highlights Astron., 15, 97
Bassino, L. P., Faifer, F. R., Forte, J. C., et al. 2006, A&A, 451, 789
Bedregal, A. G., Aragón-Salamanca, A., Merrifield, M. R., & Milvang-Jensen, B. 2006, MNRAS, 371, 1912
Bialas, D., Lisker, T., Olczak, C., Spurzem, R., & Kotulla, R. 2015, A&A, 576, A103
Binggeli, B., Tammann, G. A., & Sandage, A. 1987, AJ, 94, 251
Blakeslee, J. P., Jordán, A., Mei, S., et al. 2009, ApJ, 694, 556
Blakeslee, J. P., Cantiello, M., Mei, S., et al. 2010, ApJ, 724, 657
Boselli, A., & Gavazzi, G. 2006, PASP, 118, 517
Boselli, A., Boissier, S., Cortese, L., et al. 2006, ApJ, 651, 811
Brook, C. B., Stinson, G. S., Gibson, B. K., et al. 2012, MNRAS, 426, 690
Bryant, J. J., Owers, M. S., Robotham, A. S. G., et al. 2015, MNRAS, 447, 2857
Buta, R. J. 2011, ArXiv e-prints [arXiv:1102.0550]
Cantiello, M., D'Abrusco, R., Spavone, M., et al. 2018, A&A, 611, A93
Caon, N., Capaccioli, M., & D'Onofrio, M. 1994, A&AS, 106, 199
Capaccioli, M., Spavone, M., Grado, A., et al. 2015, A&A, 581, A10
Cappellari, M., Emsellem, E., Krajnović, D., et al. 2011, MNRAS, 413, 813
Carollo, C. M., Franx, M., Illingworth, G. D., & Forbes, D. A. 1997, ApJ, 481, 710
Cook, B. A., Conroy, C., Pillepich, A., Rodriguez-Gomez, V., & Hernquist, L. 2016, ApJ, 833, 158
Cooper, A. P., Parry, O. H., Lowing, B., Cole, S., & Frenk, C. 2015, MNRAS, 454, 3185
Crnojević, D., Sand, D. J., Spekkens, K., et al. 2016, ApJ, 823, 19
Cui, W., Murante, G., Monaco, P., et al. 2014, MNRAS, 437, 816
D'Abrusco, R., Cantiello, M., Paolillo, M., et al. 2016, ApJ, 819, L31
Davies, J. I., Bianchi, S., Baes, M., et al. 2013, MNRAS, 428, 834
Dekel, A., & Birnboim, Y. 2006, MNRAS, 368, 2
De Lucia, G., & Blaizot, J. 2007, MNRAS, 375, 2
de Zeeuw, P. T., Bureau, M., Emsellem, E., et al. 2002, MNRAS, 329, 513
Dressler, A., Oemler, Jr., A., Couch, W. J., et al. 1997, ApJ, 490, 577
Drinkwater, M. J., Gregg, M. D., & Colless, M. 2001, ApJ, 548, L139
Duc, P.-A., Cuillandre, J.-C., Karabal, E., et al. 2015, MNRAS, 446, 120
Eigenthaler, P., Puzia, T. H., Taylor, M. A., et al. 2018, ApJ, 855, 142
Erwin, P., Pohlen, M., & Beckman, J. E. 2008, AJ, 135, 20
Fasano, G., Poggianti, B. M., Bettoni, D., et al. 2015, MNRAS, 449, 3927
Ferguson, H. C. 1989, AJ, 98, 367
Ferguson, H. C., & Sandage, A. 1988, AJ, 96, 1520
Ferrarese, L., Côté, P., Cuillandre, J.-C., et al. 2012, ApJS, 200, 4
Forbes, D. A., Franx, M., & Illingworth, G. D. 1995, AJ, 109, 1988
Fukugita, M., Ichikawa, T., Gunn, J. E., et al. 1996, AJ, 111, 1748
Grado, A., Capaccioli, M., Limatola, L., & Getman, F. 2012, Mem. Soc. Astron. It., 19, 362
Grillmair, C. J., Freeman, K. C., Bicknell, G. V., et al. 1994, ApJ, 422, L9
Gunn, J. E., & Gott, III., J. R. 1972, ApJ, 176, 1
Gutiérrez, C. M., Trujillo, I., Aguerri, J. A. L., Graham, A. W., & Caon, N. 2004, ApJ, 602, 664
Hilker, M. 2015, IAU General Assembly, 22, 2215712
Iodice, E., Capaccioli, M., Grado, A., et al. 2016, ApJ, 820, 42
Iodice, E., Spavone, M., Capaccioli, M., et al. 2017a, ApJ, 839, 21
Iodice, E., Spavone, M., Cantiello, M., et al. 2017b, ApJ, 851, 75
Jaffé, Y. L., Smith, R., Candlish, G. N., et al. 2015, MNRAS, 448, 1715
Janowiecki, S., Mihos, J. C., Harding, P., et al. 2010, ApJ, 715, 972
Jiménez-Teja, Y., Dupke, R.A., Lopes de Oliveira, R., et al. 2019, A&A, 622, A183
Jordán, A., Blakeslee, J. P., Côté, P., et al. 2007, ApJS, 169, 213
Kent, S. M., & Gunn, J. E. 1982, AJ, 87, 945
Kodama, T., Smail, I., Nakata, F., Okamura, S., & Bower, R. G. 2001, ApJ, 562, L9
Kormendy, J., Fisher, D. B., Cornell, M. E., & Bender, R. 2009, ApJS, 182, 216
La Barbera, F., Ferreras, I., de Carvalho, R. R., et al. 2012, MNRAS, 426, 2300
Larson, R. B., Tinsley, B. M., & Caldwell, C. N. 1980, ApJ, 237, 692
Laurikainen, E., Salo, H., Buta, R., et al. 2006, AJ, 132, 2634
Lewis, I., Balogh, M., De Propris, R., et al. 2002, MNRAS, 334, 673
Lisker, T., Vijayaraghavan, R., Janz, J., et al. 2018, ApJ, 865, 40
Łokas, E. L., Ebrová, I., del Pino, A., et al. 2016, ApJ, 826, 227
Martin, C., & GALEX Team 2005, in Maps of the Cosmos, eds. M. Colless, L. Staveley-Smith, & R. A. Stathakis, IAU Symp., 216, 221
Martínez-Delgado, D., Gabany, R. J., Crawford, K., et al. 2010, AJ, 140, 962
Martinez-Valpuesta, I., Aguerri, J. A. L., González-García, A. C., Dalla Vecchia, C., & Stringer, M. 2017, MNRAS, 464, 1502
Mastropietro, C., Moore, B., Mayer, L., et al. 2005, MNRAS, 364, 607
McNeil-Moylan, E. K., Freeman, K. C., Arnaboldi, M., & Gerhard, O. E. 2012, A&A, 539, A11
Mellier, Y., Soucail, G., Fort, B., & Mathez, G. 1988, A&A, 199, 13
Méndez-Abreu, J., Sánchez-Janssen, R., Aguerri, J. A. L., Corsini, E. M., & Zarattini, S. 2012, ApJ, 761, L6
Merluzzi, P., Busarello, G., Dopita, M. A., et al. 2016, MNRAS, 460, 3345
Merritt, A., van Dokkum, P., Abraham, R., & Zhang, J. 2016, ApJ, 830, 62
Michel-Dansac, L., Martig, M., Bournaud, F., et al. 2010, in AIP Conf. Ser., eds. V. P. Debattista, & C. C. Popescu, 1240, 283

Mihos, C. 2015, IAU General Assembly, 22, 2247903
Mihos, J. C., Harding, P., Feldmeier, J., & Morrison, H. 2005, ApJ, 631, L41
Mihos, J. C., Harding, P., Feldmeier, J. J., et al. 2017, ApJ, 834, 16
Monachesi, A., Gómez, F. A., Grand, R. J. J., et al. 2018, MNRAS, submitted [arXiv:1804.07798]
Moore, B., Lake, G., & Katz, N. 1998, ApJ, 495, 139
Munoz, R. P., Eigenthaler, P., Puzia, T. H., & Taylor, M. A. 2015, ApJ, 813, L15
Napolitano, N. R., Pannella, M., Arnaboldi, M., et al. 2003, ApJ, 594, 172
Narayan, C. A., & Jog, C. J. 2002, A&A, 394, 89
Paolillo, M., Fabbiano, G., Peres, G., & Kim, D.-W. 2002, ApJ, 565, 883
Pasquali, A., Smith, R., Gallazzi, A., et al. 2019, MNRAS, 484, 1702
Peng, Y.-J., Lilly, S. J., Kovač, K., et al. 2010, ApJ, 721, 193
Peng, Y., Maiolino, R., & Cochrane, R. 2015, Nature, 521, 192
Pinna, F., Falcón-Barroso, J., Martig, M., et al. 2019, A&A, in press, DOI: 10.1051/0004-6361/201833193
Pota, V., Napolitano, N. R., Hilker, M., et al. 2018, MNRAS, 481, 1744
Puchwein, E., Springel, V., Sijacki, D., & Dolag, K. 2010, MNRAS, 406, 936
Quinn, P. J. 1984, ApJ, 279, 596
Rhee, J., Smith, R., Choi, H., et al. 2017, ApJ, 843, 128
Roediger, J. C., Courteau, S., MacArthur, L. A., & McDonald, M. 2011, MNRAS, 416, 1996
Rudick, C. S., Mihos, J. C., Frey, L. H., & McBride, C. K. 2009, ApJ, 699, 1518
Sánchez, S. F., Kennicutt, R. C., Gil de Paz, A., et al. 2012, A&A, 538, A8
Sarzi, M., Iodice, E., Coccato, L., et al. 2018, A&A, 616, A121
Scharf, C. A., Zurek, D. R., & Bureau, M. 2005, ApJ, 633, 154
Schindler, S., Binggeli, B., & Böhringer, H. 1999, A&A, 343, 420
Schipani, P., Noethe, L., Arcidiacono, C., et al. 2012, J. Opt. Soc. Am. A, 29, 1359
Schlegel, D. J., Finkbeiner, D. P., & Davis, M. 1998, ApJ, 500, 525
Schuberth, Y., Richtler, T., Bassino, L., & Hilker, M. 2008, A&A, 477, L9
Schuberth, Y., Richtler, T., Hilker, M., et al. 2010, A&A, 513, A52
Schulz, C., Hilker, M., Kroupa, P., & Pflamm-Altenburg, J. 2016, A&A, 594, A119
Scott, N., Davies, R. L., Houghton, R. C. W., et al. 2014, MNRAS, 441, 274
Seigar, M. S., Graham, A. W., & Jerjen, H. 2007, MNRAS, 378, 1575
Serra, P., de Blok, W. J. G., Bryan, G. L., et al. 2016, in Proceedings of MeerKAT Science: On the Pathway to the SKA. 25–27 May, 2016 Stellenbosch, South Africa (MeerKAT2016), https://pos.sissa.it/cgi-bin/reader/conf.cgi?confid=277, 8
Sheardown, A., Roediger, E., Su, Y., et al. 2018, ApJ, 865, 118
Smith, R., Davies, J. I., & Nelson, A. H. 2010, MNRAS, 405, 1723
Smith, R., Sánchez-Janssen, R., Beasley, M. A., et al. 2015, MNRAS, 454, 2502
Smith, R., Choi, H., Lee, J., et al. 2016, ApJ, 833, 109
Spavone, M., Capaccioli, M., Napolitano, N. R., et al. 2017, A&A, 603, A38
Spiniello, C., Napolitano, N. R., Arnaboldi, M., et al. 2018, MNRAS, 477, 1880
Su, Y., Nulsen, P. E. J., Kraft, R. P., et al. 2017, ApJ, 851, 69
Taylor, E. N., Hopkins, A. M., Baldry, I. K., et al. 2011, MNRAS, 418, 1587
Tonry, J. L., Dressler, A., Blakeslee, J. P., et al. 2001, ApJ, 546, 681
Toomre, A., & Toomre, J. 1972, ApJ, 178, 623
Tremaine, S. 1981, in Structure and Evolution of Normal Galaxies, eds. S. M. Fall, & D. Lynden-Bell, 67
Trujillo, I., & Fliri, J. 2016, ApJ, 823, 123
Trujillo, I., Aguerri, J. A. L., Gutiérrez, C. M., & Cepa, J. 2001, AJ, 122, 38
Tully, R. B., & Trentham, N. 2008, AJ, 135, 1488
Tutukov, A. V., & Fedorova, A. V. 2011, Astron. Rep., 55, 383
van der Wel, A., Bell, E. F., Holden, B. P., Skibba, R. A., & Rix, H.-W. 2010, ApJ, 714, 1779
van Dokkum, P. G., Abraham, R., & Merritt, A. 2014, ApJ, 782, L24
Venhola, A., Peletier, R., Laurikainen, E., et al. 2017, A&A, 608, A142
Venhola, A., Peletier, R., Laurikainen, E., et al. 2018, A&A, 620, A165 (Paper IV)
Vijayaraghavan, R., & Ricker, P. M. 2013, MNRAS, 435, 2713
Zabel, N., Davis, T., Smith, W., et al. 2019, MNRAS, 483, 2251
Zwicky, F. 1957, Morphological Astronomy (Berlin: Springer)

Appendix A: Results on individual galaxies: A deep look at the outskirts

In this section we describe in detail the main properties of each galaxy of the sample from the FDS dataset presented in this paper. We focus on the faint features and structures in the outskirts of ETGs, which were unexplored in previous studies of the Fornax cluster. We identify as stellar envelope the regions at $\mu_r \geq 26$ mag arcsec^{-2}. For each galaxy of the sample, we discuss the light and colour distribution shown in Appendices B and C, respectively.

A.1. FCC 090

FCC 090 is a small ($R_e = 1.5$ kpc) and faint ($M_i = -18.06$ mag) elliptical galaxy (see Table 4) in the SW region of the cluster at 1.7° from NGC 1399 (see Fig. 2). The VST image in the r band is shown in Fig. B.1 (top left panel). The surface brightness is mapped down to $\mu_r \sim 29$ mag arcsec^{-2} and out to about $11R_e \sim 16.5$ kpc (see lower panels of Fig. B.1). The isophotes show a large twisting, with PA varying by about 60° from the centre to large radii (see top-right panel of Fig. B.1). The stellar envelope, at $\mu_r \simeq 28$–29 mag arcsec^{-2}, is flatter ($\epsilon \sim 0.4$) than the inner isophotes ($\epsilon \sim 0.2$) and it has faint ($\mu_r \geq 29$ mag arcsec^{-2}) substructures on the SE, in the form of a tiny tail (∼0.6 arcmin) towards the east, and on the north-eastern side where an over-density of light makes the isophotes more elongated towards the north. The colour map brings to light a very irregular structure (see Fig. C.1), where the isophotes show several ripples. The inner regions (for $R \leq 0.1$ arcmin) are quite blue (g–$r \sim 0.3$–0.4 mag) with respect to the outer and fainter envelope (g–$r \sim 0.6$–0.8 mag). Taken together, this could suggest a recent minor merging event in this galaxy. The accretion of one or more smaller companion galaxies by an early-type disc galaxy could form shells or ripples (e.g. Quinn 1984) like those observed in FCC 090. Preliminary results from the ALMA survey of the Fornax cluster (Zabel et al., in prep.) also suggest that past galaxy–galaxy interactions may be responsible for the irregular gas morphology and kinematics.

A.2. FCC 143 (NGC 1373)

FCC 143 is a compact ($R_e = 1.0$ kpc and $M_i = -19.04$ mag, see Table 4) elliptical galaxy on the western side of the cluster, at 0.76° from NGC 1399 (see Fig. 2). This galaxy is quite close in space to FCC 147, a more luminous and bigger elliptical galaxy SE of FCC 143. According to Blakeslee et al. (2009), the difference in distance is only 0.3 Mpc. The deep VST image in the r band shows a very faint bridge of light $\mu_r \simeq 29.5$ mag arcsec^{-2} between the two galaxies (see the top left panel of Fig. B.2), which suggests a possible ongoing interaction. In the centre, the bright and disc-like structure on the north is a superposed background edge-on disc galaxy. The outer and faint stellar envelope is rounder ($\epsilon \sim 0.05$) than the inner isophotes ($\epsilon \sim 0.2$). The major axis points towards and is aligned with the major axis of the companion galaxy FCC 147 ($P.A. \sim 120°$, see top right panel of Figs. B.2 and B.3). The g–i colour map and colour profile show that the centre is quite red (g–$i \sim 1.3$ mag) and has a remarkable gradient towards bluer values with radius (see the top left panels of Fig. C.1), with g–$i \sim 0.7$ mag at $R \sim 1$ arcmin. Therefore, the outer stellar envelope is blue, with colours comparable to those observed in the outskirts of the companion galaxy FCC 147 (see the lower left panels of Fig. C.1).

A.3. FCC 147 (NGC 1374)

FCC 147 is one of the brightest ($M_i \leq -21.31$ mag) elliptical galaxies in the core of the Fornax cluster, at 0.67° from NGC 1399, on the western side (see Fig. 2 and Table 4). This galaxy is close in space to FCC 143 (see also Sect. A.2), with which the deep VST image shows a possible ongoing interaction. It is also close to the S0 galaxy FCC 148 and the distances for the two galaxies are quite similar (Blakeslee et al. 2009). The surface brightness is mapped down to $\mu_r \sim 29$ mag arcsec^{-2} and out to about 13–$15\,R_e \sim 34$ kpc (see lower panels of Fig. B.3). The stellar envelope is quite extended ($1 \leq R \leq 10$ arcmin) and flatter ($\epsilon \sim 0.4$) than the inner isophotes ($\epsilon \sim 0.05$). The centre is red (g–$i \sim 1.4$ mag) and the colour profile decreases with radius of about 0.7 magnitudes in the outskirts, where g–$i \sim 0.7$ mag at $R \sim 2$ arcmin.

A.4. FCC 148 (NGC 1375)

This is an S0 galaxy with a marked boxy bulge (see Fig. B.4, top left panel), very close to the elliptical galaxy FCC 147, located on the western side of the cluster at 0.67° from NGC 1399. In order to account for the light from the nearby galaxy FCC 147, before performing the isophote fit on FCC 148, the 2D model of FCC147 was subtracted from the image. The 2D model for FCC 147 was obtained by the isophote fit for this galaxy, using the IRAF task BMODEL. Figure B.4 (top left panel) shows the resulting image for FCC 148. The SB profiles show two breaks in all bands (see lower left panel of Fig. B.4): the inner break is at $R \sim 0.3$ arcmin ($\sim 1\,R_e \sim 1.3$ kpc), where the profile becomes steeper, and the second break occurs at about $4\,R_e$(∼5 kpc), where the profile shows an upturn. This is a typical example of a composite Type-II + Type-III profile (see Sect. 5). Since the ellipticity and PA profiles also change at the second break (see top right panels of Fig. B.4), according to Erwin et al. (2008) this part of the surface brightness distribution maps the stellar envelope rather than being a truncated disc. In these regions, colours are bluer (g–$i \sim 0.7 - 0.9$) than in the inner disc (g–$i \sim 1$), even if a dip of about 0.2 magnitudes is observed in the centre ($0.3 \leq R \leq 3$ arcsec, see Fig. C.1, lower right panels), suggesting the presence of bluer substructure. In the same range of radii, long-slit kinematics by Bedregal et al. (2006) pointed out the evidence of a kinematically decoupled component.

A.5. FCC 153 (IC 1963)

FCC 153 is an edge-on S0 galaxy located in the low-density region on the north of the cluster, at a projected distance from NGC 1399 of 1.17° (see Fig. 2). As observed for FCC 148, also in this case the SB profiles show two breaks. The inner one is at $R \sim 0.2$ arcmin ($\sim 1\,R_e \sim 3$ kpc), followed by a steep exponential-like decline out to about $5\,R_e$ (see lower panels Fig. B.5). At larger radii, the SB profiles appear shallower out to $10\,R_e$ and down to $\mu_r \sim 29$ mag arcsec^{-2}. Together with the other two edge-on S0 galaxies of the sample (FCC 170 and FCC 177), FCC 153 shows a flaring in the disc, towards the outer radii, which is detected both in the light distribution (see the top panels of Fig. 14) and in the colour map (see Sect. 5.1). The colour map (see Fig. C.2, top left panel) reveals a thin and red disc (g–$i \sim 0.8$ mag) with a flaring in the outer regions ($R \geq 1$ arcmin), where it appears a bit bluer (g–$i \sim 0.7$ mag).

A.6. FCC 161 (NGC 1379)

This is the brightest ($M_i = -21.35$ mag, see Table 4) elliptical galaxy inside the stellar halo of NGC 1399. In projection, it is located about 0.5° from NGC 1399, on the western side (see Fig. 2). This galaxy is in the area where intra-cluster light (ICL) was detected (Iodice et al. 2017b). As also pointed out by Iodice et al. (2017b), the stellar halo of the galaxy is very asymmetric: it extends in the NE-SW direction and an excess of light is detected on the SW side (see Fig. B.6, top left panel). The surface brightness distribution is mapped down to $\mu_g \sim 30$ mag arcsec^{-2} and out to ~13 R_e (~34 kpc, see lower panels of Fig. B.6). A strong twisting (~50°) and an increasing flattening ($0 \leq \epsilon \leq 0.4$) is observed for $R \geq 2$ arcmin in the region of the stellar envelope, where the SB profiles show a shallower decline. In the nuclear regions, for $R \leq 2$ arcsec, where the PA shows a twist of about 50° and there is a small increase in the ellipticity (~0.05), the colour map reveals the presence of nuclear dust (see Fig. C.2), where $g-i \sim 1.2$ mag. The outer stellar envelope, for $R \geq 2$ arcmin, is bluer ($g-i \sim 1.$ mag) than the inner and brightest region of the galaxy where the colour profile shows a small gradient from $g-i \sim 1.2$ mag to $g-i \sim 1.1$ mag (see top right panels of Fig. C.2).

A.7. FCC 167 (NGC 1380)

FCC 167 was chosen as an illustrative example to show each step of the analysis presented in this work. Some details on its structure were already given in Sect. 4. It is the brightest S0 galaxy inside the virial radius of the cluster, with $M_i = -22.8$ mag (see Table 4). In the inner ~1 arcmin, the high-frequency residual image reveals a bar-like boxy structure along the major axis of the galaxy, which ends with a bright knot on each side at $R \sim 1.3$ arcmin (see right panel of Fig. 3). The outer and fainter isophotes ($R \geq 3$ arcmin and $\mu_r \sim 27-30$ mag arcsec^{-2}) appear less flattened and twisted with respect to the inner and more disky ones (see top left panel of Figs. 3 and B.7). The r-band SB profile extends out to 10 arcmin (~52 kpc) from the centre, which is about 10 R_e, and down to $\mu_r = 29 \pm 1$ mag arcsec^{-2} (see lower right panel of Fig. 3). The dust absorption affects the light distribution inside 0.1 arcmin, and perturbs the PA and ellipticity profiles at the same distance (see top right panel of Fig. B.7). At larger radii, two breaks are observed. The first break marks the end of the bar-like boxy structure; it is between 1 and 1.5 arcmin, where the SB profile becomes steeper. The second break is at $R \sim 3$ arcmin, where the SB profile is shallower. The ellipticity and PA profiles also show different behaviours at the break radii given above, in particular the isophotes are progressively rounder at larger radii. As suggested by Erwin et al. (2008), this is an indication that light in this region is due to a spheroidal component rather than being part of the disc, therefore the SB profile is classified as Type III-s. The $g-i$ colour map and the azimuthally averaged $g-i$ colour profile are shown in Fig. 4. The galaxy is quite red in the centre, with $g-i \simeq 1.2-1.3$ mag for $R \leq 0.1$ arcmin. A peak is observed at ~5 arcsec, where $g-i \sim 1.3$ mag. At larger radii, the galaxy is bluer, having $g-i \simeq 1.1-1.2$ mag for $0.1 \leq R \leq 3$ arcmin (see bottom panel of Fig. 4). Inside 1 arcmin, the spiral-like structure detected in the light distribution (see Fig. 3) appears also in the $g-i$ colour map (see the upper panels of Fig. 4). It seems more extended on the western side of the galaxy and has a colour gradient toward bluer values ($g-i \leq 1.2$ mag). In the inner 10 arcsec, the ring of dust appears as a quite red ($g-i \sim 1.3$ mag) structure. At larger radii, for $R \geq 3$ arcmin, a strong gradient towards red colours is observed ($g-i \sim 1.2-1.5$ mag), which is significant even taking into account the larger errors (see lower panel of Fig. B.7).

A.8. FCC 170 (NGC 1381)

This is an edge-on S0 galaxy close to the centre of the cluster, located at a projected distance of 0.42° from NGC 1399 (see Fig. 2). Together with FCC 161 and FCC 184, FCC 170 is in the area where the diffuse intra-cluster light was detected by Iodice et al. (2017b). The inner and bright regions show a boxy bulge and a thin disc, while the faintest outskirts ($\mu_r \sim 27-30$ mag arcsec^{-2}) resemble the superposition of a thick disc and a rounder envelope (see Fig. B.8). This galaxy has a prominent flaring of the disc towards outer radii (see the middle panels of Fig. 14), which is more extended and thickest compared to the similar features detected in FCC 153 and FCC 177 (see Sect. 5.1). The SB profiles show two breaks (see lower panels of Fig. B.8), the first in the inner regions at $R \sim 1$ arcmin (2 $R_e \sim 4$ kpc) and the second at $R \sim 3$ arcmin (7 $R_e \sim 6$ kpc). To the second break radius corresponds a variation of the PA and ellipticity profiles, with a twisting of about 20° and ϵ increases from ~0.3 to ~0.5 (see top panel of Fig. B.8). As discussed for the other S0 galaxies of the sample, this is a typical example of a composite Type-II + Type-III profile. The inner boxy bulge and the thin disc are quite red, with $g-i \sim 1.2$ mag (see lower left panel of Fig. C.2). The thick disc has $g-i \sim 1-1.1$ mag and the stellar envelope is even bluer, with $g-i \leq 0.9$ mag.

A.9. FCC 177 (NGC 1380A)

This is an edge-on S0 galaxy in the north of the cluster, at a projected distance of 0.78° from NGC 1399 (see Fig. 2). It is characterised by a small and bright bulge ($R \leq 30$ arcsec and $\mu_r \geq 20$ mag arcsec^{-2}), an extended thin disc ($R \leq 2$ arcmin and $\mu_r \sim 20-27$ mag arcsec^{-2}), and a thick stellar halo ($R \geq 2$ arcmin and $\mu_r \sim 24$ mag arcsec^{-2}, see Fig. B.9). Therefore, the resulting SB profiles are of Type-II + Type-III, as observed for many other S0 galaxies of the sample (see Sect. 5). As for FCC 153 and FCC 170, a flaring of the disc is observed in the light distribution (see Sect. 5.1), which is also detected in the colour map, in the outer regions of the disc ($R \geq 1$ arcmin) along the major axis. Differently from FCC 153, colours are red, $g-i \sim 1.1-1.3$ mag (see lower right panel of Fig. C.2). In the inner regions ($R \leq 0.5$ arcmin), the colour map shows a thin and blue feature ($g-i \sim 0.9$ mag). The thick stellar envelope, which can be mapped along the galaxy minor axis, has a bluer colour than the thin disc, with $g-i \sim 0.85-1$ mag.

A.10. FCC 182

FCC 182 is a small ($R_e = 1.2$ kpc, see Table 4) face-on S0 galaxy, very close to the cluster centre, at a projected distance of 0.32° from NGC 1399 (see Fig. 2). This galaxy is completely embedded in the ICL detected by Iodice et al. (2017b). Differently from the other galaxies in this area (FCC 161, FCC 170, and FCC 184), the outer isophotes of FCC 182 appear quite regular and symmetric (see the top right panel of Fig. B.10). The flattened isophotes ($\epsilon \sim 0.3$) and the constant PA (~170°) inside 0.1 arcmin suggest the presence of a small bar. For $0.1 \leq R \leq 0.3$ arcmin, a moderate twisting of about 50° is observed, where the isophotes are almost round. At larger radii, the ellipticity increases again ($\epsilon \sim 0.2$) and the PA varies by more than 100°.

In this region, the SB profiles show an extended exponential-like decline down to $\mu_r \sim 29$ mag arcsec^{-2} and out to 7 R_e(~ 8.4 kpc). The colour map and colour profile show that inside 0.1 arcmin the galaxy is very red ($g-i \sim 1.15$ mag), while outside, for $0.1 \leq R \leq 0.3$ arcmin, a small gradient towards bluer colours is observed ($g-i \sim 1.15-1$ mag). The stellar envelope, for $R \geq 0.3$ arcmin, has redder colours, with $g-i$ increasing to ~1.2 mag (see the top left panel of Fig. C.3).

A.11. FCC 184 (NGC 1387)

This is the brightest ($M_i = -21.81$ mag, see Table 4) elliptical galaxy closest in space to NGC 1399. According to Blakeslee et al. (2009), the distance differs by 1.6±1.2 Mpc. In projection, it is located at about 0.3° from NGC 1399, on the western side (see Fig. 2 and Table 4). In the intra-cluster region, on the western side of NGC 1399 and towards FCC 184, Iodice et al. (2016) detected a faint ($\mu_g \sim 30$ mag arcsec^{-2}) stellar bridge, about 5 arcmin long (~29 kpc). Based on the colour analysis, it could result from the stripping of the outer envelope of FCC 184 on its eastern side. Such a feature was also detected in the spatial distribution of the blue GCs (Bassino et al. 2006; D'Abrusco et al. 2016). This galaxy is in the area of the intra-cluster light (Iodice et al. 2017b). As also pointed out by Iodice et al. (2016, 2017b), the outer isophotes of the galaxy are very asymmetric: they extend on the W-SW side (see Fig. B.11, top left panel), opposite to the region where the bridge of light towards NGC 1399 is detected. The surface brightness distribution is mapped down to $\mu_r \sim 29$ mag arcsec^{-2} and out to ~15 R_e(~43 kpc, see lower panels of Fig. B.11). A strong twisting (~100°) and an increasing flattening ($0 \leq \epsilon \leq 0.3$) is observed for $R \geq 2$ arcmin, in the region of the stellar envelope, where the SB profiles show a shallower decline. Inside 1 arcmin, the image suggests the presence of a small inner bar, characterised by the typical peak in ellipticity profile ($\epsilon \sim 0.3$). In the nuclear regions, for $R \leq 5$ arcsec, where the PA also shows a twist of about 50°, the colour map reveals the presence of a nuclear ring of dust (see Fig. C.3), where $g-i \sim 1.4$ mag. A nuclear ring of about 6 arcsec was also found from the near-infrared images in the K_s band by Laurikainen et al. (2006). The outer stellar envelope, for $R \geq 2$ arcmin, is quite red ($g-i \sim 1.6$ mag) compared to the inner and brightest region of the galaxy where the colour profile shows a small gradient from $g-i \sim 1.4$ mag to $g-i \sim 1.2$ mag (see top right panels of Fig. C.3).

A.12. FCC 190 (NGC 1380B)

This is one of the four barred S0 galaxies close in projection to the cluster centre (see Fig. 8), on the NW side. FCC 190 is at a distance of 20.3 ± 0.7 Mpc (see Table 2). This is consistent with the distance of the closest galaxies FCC 182 (19.6±0.8 Mpc) and FCC 170 (21.9±0.8 Mpc), and FCC 167 (21.2±0.7 Mpc), which is located north-west of FCC 190 (see Table 2) These four galaxies, being close in space and aligned along the north-south direction, could be a primordial sub-group of galaxies in-falling into the cluster. In FCC 190 the stellar envelope is at 90° with respect to the inner bar, and extends down to $\mu_r \sim 29$ mag arcsec^{-2} and out to 7 R_e (see Fig. B.12). Also the $g-i$ colours are quite different between the two components: the inner bar is red, with $g-i \sim 1.13$ mag, while the outer isophotes become bluer at $R \sim 0.5$ arcmin and $g-i \sim 0.9$ mag at the outer radius (see lower left panels of Fig. C.3).

A.13. FCC 193 (NGC 1389)

This barred S0 galaxy is at a projected distance of 0.39° from NGC 1399 on the SW side (see Fig. 2). South of FCC 193, as well as west and east of it, there are no more ETGs in the high-density region of the cluster (see Sect. 5). The outer and fainter isophotes, mapped down to $\mu_r \sim 29$ mag arcsec^{-2} and out to 14 R_e (see Fig. B.13), show a sharp boundary on the southern side, so that they appear more boxy than on the northern side. The position angle of the major axis of the outer envelope differs from the major axis of the bright central bulge by more than 30° (see the top right panel of Fig. B.13). The centre of FCC 193 is very red, with $g-i \sim 1.2$ mag, while bluer colours are measured with increasing semi-major axis (lower right panels of Fig. C.3).

A.14. FCC 213 (NGC 1399)

This is NGC 1399, the brightest cluster galaxy of the Fornax cluster inside the virial radius. A detailed discussion of FCC 213 based on FDS data is presented by Iodice et al. (2016).

A.15. FCC 219 (NGC 1404)

This is the second brightest ETG of the Fornax cluster, ~1 mag fainter than NGC 1399 (see Table 2), inside the viral radius. Even if FCC 219 is superposed on the very luminous outskirts of NGC 1399 and it is in the halo of a bright star south of it, the isophotes have a regular shape with semi-major axis, showing an increasing flattening and a twisting of about 10° for $R \geq 1$ arcmin, where $\mu_r \geq 23$ mag arcsec^{-2} (see Fig. B.14). The SB profiles show an extended exponential-like decrease for $R \geq 1$ *Re* (see the lower panels of Fig. B.14) out to 7 R_e and down to $\mu_r \sim 28$ mag arcsec^{-2}. Since FCC 219 is completely superposed on the stellar envelope of NGC 1399, it is reasonable to think that the outskirts of both galaxies overlap in projection at the faintest magnitudes, being indistinguishable by the photometry alone. The $g-i$ colour profile is quite constant ~1.3–1.2 mag out to $R \sim 1$ arcmin, very similar to that for NGC 1399 (see lower panels of Fig. C.4). At larger radii, the colours are bluer $g-i \sim 0.7$, consistent with the $g-i$ colours derived for the stellar envelope of NGC 1399. The inner regions of FCC219 are quite red, $g-i \sim 1.3$. A small (few arcsecs) red feature is detected on the south of the galaxy centre, which seems to be connected to a red tail on its eastern side. It could be the remnant of a disrupted small galaxy or a background galaxy.

A.16. FCC 276 (NGC 1427)

This is the brightest ($M_i = -21.3$ mag, see Table 4) elliptical galaxy located on the eastern side of the cluster, at a projected distance of 0.79° from NGC 1399 (see Fig. 2), in the transition region of the cluster from high to low density (see Fig. 2). The SB profiles are mapped out to ~9 R_e, except for the u-band SB, which is less extended (~6 R_e), and down to $\mu_r \sim 29$ mag arcsec^{-2} in the r band (see Fig. B.15). The outer and fainter isophotes appear asymmetric: they are more extended on the N-NW side, where many diffuse and very faint ($\mu_r \sim 30$ mag arcsec^{-2}) patches of light are detected, than the isophotes on the opposite SE side, which show a sharp boundary. The $g-i$ colour profile and colour map (see the top left panels of Fig. C.5) show a very blue nucleus: for $R \leq 2$ arcsec the $g-i$ decreases from 0.85 mag to ~0.65 mag (this is not a seeing effect, since it affects the profile only for $R \leq 0.01$ arcmin). Similar behaviour was found by Carollo et al. (1997) in the $V-I$ colour

profile (obtained with the *Hubble* Space Telescope), where $V-I$ decreases by ∼0.15 mag inside 0.1 arcsec. The $g-i$ colour map shows a disky and blue ($g-i \sim 0.7$ mag) nucleus surrounded by redder regions ($g-i \sim 0-8-0.9$ mag) with a ring-like feature made of red knots. The presence of a nuclear disc between 0.3 and 3 arcsec was suggested by Forbes et al. (1995). The galaxy becomes bluer with increasing radius and in the outskirts $g-i \sim 0.7-0.6$ mag.

A.17. FCC 277 (NGC 1428)

This galaxy is located on the eastern side of the cluster, at a projected distance of 0.86° from NGC 1399 (see Fig. 2), in the transition region of the cluster from the high to low density (see Fig. 2) north of FCC 276, the other elliptical galaxy in this area. FCC 277 is about two magnitudes fainter than FCC 276 (see Table 4) and the distance differs by 1.1±1.3 Mpc (Blakeslee et al. 2009). Like FCC 276, FCC 277 resembles a "normal" elliptical galaxy without any prominent subcomponents (see Fig. B.16), such as bars or X-shaped bulges observed for many of the ETGs in the high-density region of the cluster on the western side. The *gri* SB profiles extend out to ∼15 R_e, while the SB in the u band is less extended (∼7 R_e). The limiting magnitude is $\mu_r \sim 29$ mag arcsec^{-2} in the r band (see Fig. B.16). The shape of the stellar envelope is quite regular. As observed in FCC 276, also in FCC 277 the inner regions of the galaxy are bluer: $g-i$ decreases by about 0.1 magnitude (from 0.8 to 0.7 mag) for $R \leq 2.4$ arcsec (see the top-right panels of Fig. C.5). The $g-i$ colour map shows a clear bluer nuclear structure with $g-i \sim 0.7$ mag. The outer regions of the galaxy tend to get bluer ($0.8 \leq g-i \leq 0.65$ mag) with increasing distance from the centre, $0.3 \leq R \leq 0.9$ arcmin. At larger radii ($R > 1$ arcmin), the colour profile shows redder values ($g-i \sim 0.75$ mag): these regions could be affected by the scattered light of the bright and red foreground star on the NE side of the galaxy.

A.18. FCC 301

This is the faintest ($M_i = -18.82$ mag, see Table 4) elliptical galaxy in the sample located on the SE side of the cluster, at a projected distance of 1.44° from NGC 1399 (see Fig. 2), in the low density region of the cluster (see Fig. 2). The *gri* SB profiles extend out to ∼11−14 R_e, while the SB in the u band is less extended and reaches ∼7 R_e (see Fig. B.17). The inner regions ($R \leq 0.1$ arcmin) are flatter ($\epsilon \sim 0.4-0.5$) than the stellar envelope (see top panels of Fig. B.17), which has smooth and unperturbed isophotes. As observed in FCC 276 and in FCC 277, also FCC 301 shows a blue structure in the inner regions of the galaxy. The $g-i$ colour map and colour profile reveal a blue ($g-i \sim 0.6$ mag) disc-like structure in the nucleus (see the lower left panels of Fig. C.5), inside 6 arcsec. The flattened isophotes and blue colours are both consistent with an inner disc component in this galaxy. This is also in agreement with the stellar long-slit kinematics by Bedregal et al. (2006), where a flat and low velocity dispersion is found in the inner 5 arcsec, so that the authors suggested the presence of a counter-rotating stellar disc, consistent with the new FDS data. The galaxy is quite red in the regions outside the nuclear disc-like structure, with $g-i \sim 0.7-0.8$ mag out to $R \sim 0.3$ arcmin. At larger radii, the stellar envelope is bluer, with $g-i \sim 0.65-0.55$ mag out to $R \sim 1$ arcmin.

A.19. FCC 310 (NGC 1460)

This is the only barred S0 galaxy on the eastern side of the cluster, south of NGC 1399, at a projected distance of 2°, so at the virial radius. The prominent and bright ($\mu_r \leq 24$ mag arcsec^{-2}) bar is evident in the image as well as in the SB and ellipticity and PA profiles (see Fig. B.18). The *gri* SB profiles extend out to ∼6−7 R_e. They show two breaks: the inner one, due to the bar, at $R \sim 0.5$ arcmin, where the SB profiles become steeper, and the outer one at $R \sim 1$ arcmin and for $\mu_r \geq 26$ mag arcsec^{-2}, where a shallow and almost exponential-like decrease is observed. The isophotes in these regions are rounder ($\epsilon \sim 0.2$) and twisted by about 100° (see top right panels of Fig. B.18). As observed for all ETGs on the eastern side of the cluster (FCC 276, FCC 277, and FCC 301), FCC 310 also shows a blue nucleus, with $g-i \sim 0.65$ in the centre and $g-i \sim 0.8$ at $R \sim 2$ arcsec (see the lower right panels of Fig. C.5). Colour is almost constantly $g-i \sim 0.8$ mag along the bar, for $0.03 \leq R \leq 0.5$ arcmin. At larger radii, the galaxy outskirts are bluer, with $g-i \sim 0.6$ mag at $R \sim 1$ arcmin.

Appendix B: *r*-band VST images of the ETGs inside the virial radius of the Fornax cluster: Surface brightness, ellipticity, and PA profiles

In each figure of this section we show the results from the fit of the isophote, performed for all ETGs in the Fornax cluster listed in Table 2 in the *ugri* VST images (see Sect. 3 for details). The top left panel of each figure shows an extracted region of the VST mosaic in the *r* band around each galaxy of the sample, plotted in surface brightness levels (shown in the colour bar). The black line indicates the scale in arc-minutes and the corresponding value of the effective radius R_e in the *r* band (listed in Table 3). The top right panels show the PA (top) and ellipticity (lower) profiles, derived by the isophote fit from *ugri* VST images. In the lower panels, we show the azimuthally averaged surface brightness profiles in *ugri* bands, plotted in logarithmic scale (left) and in linear scale (right) as a function of the effective radius R_e derived in each band (see Table 3). The vertical dotted line (left panel) delimits the region affected by the seeing.

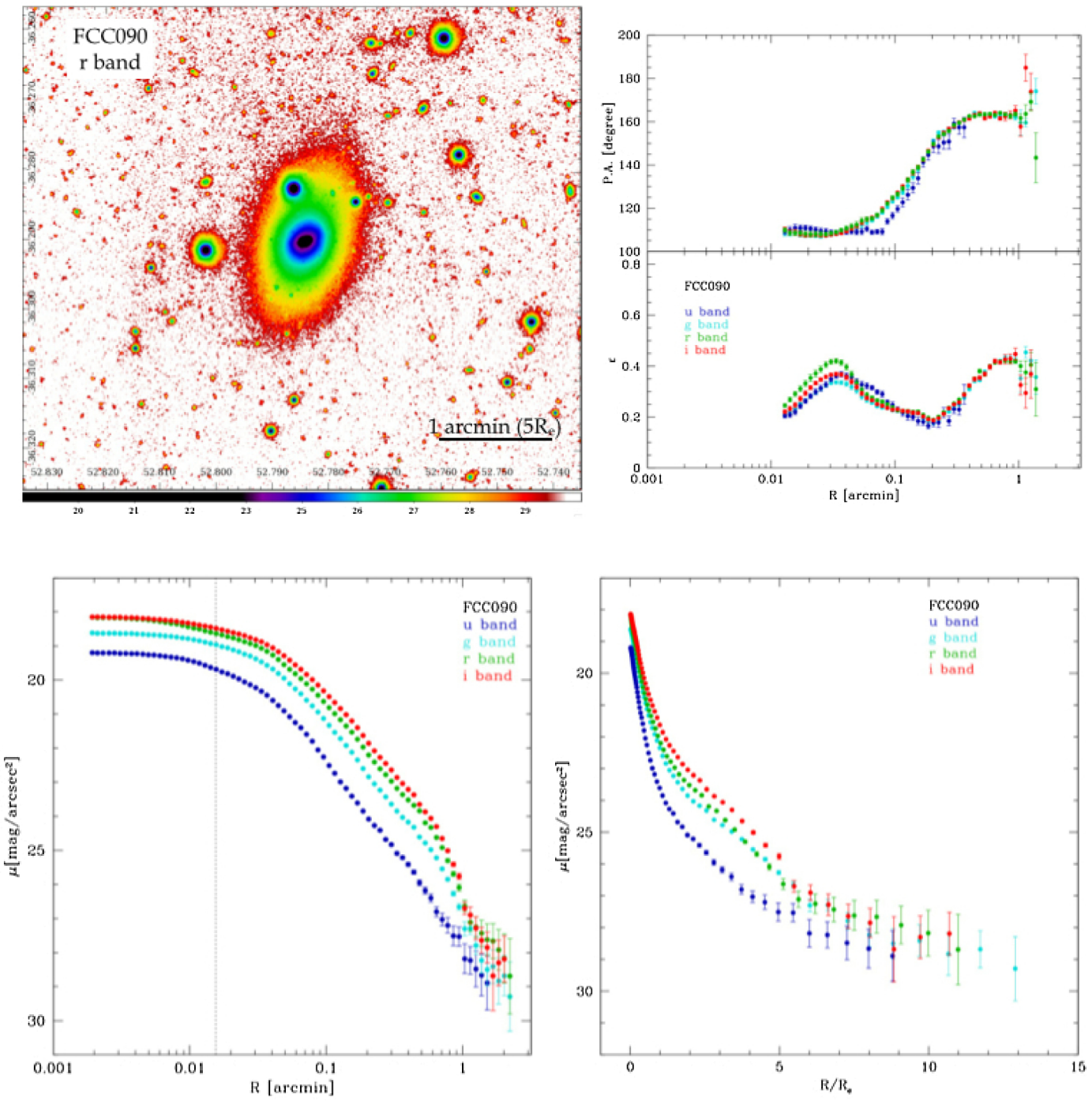

Fig. B.1. Surface photometry for FCC 090.

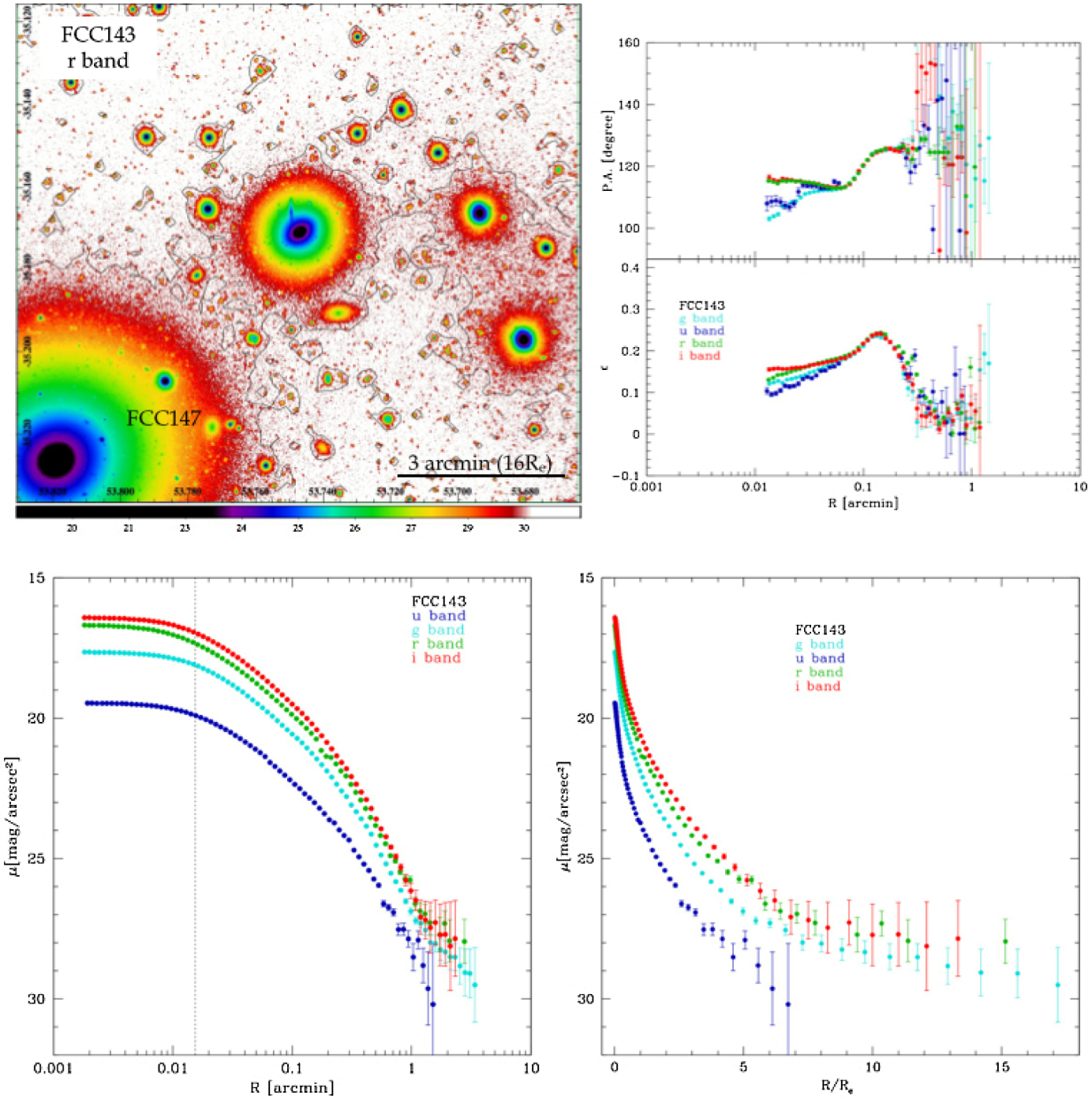

Fig. B.2. Surface photometry for FCC 143.

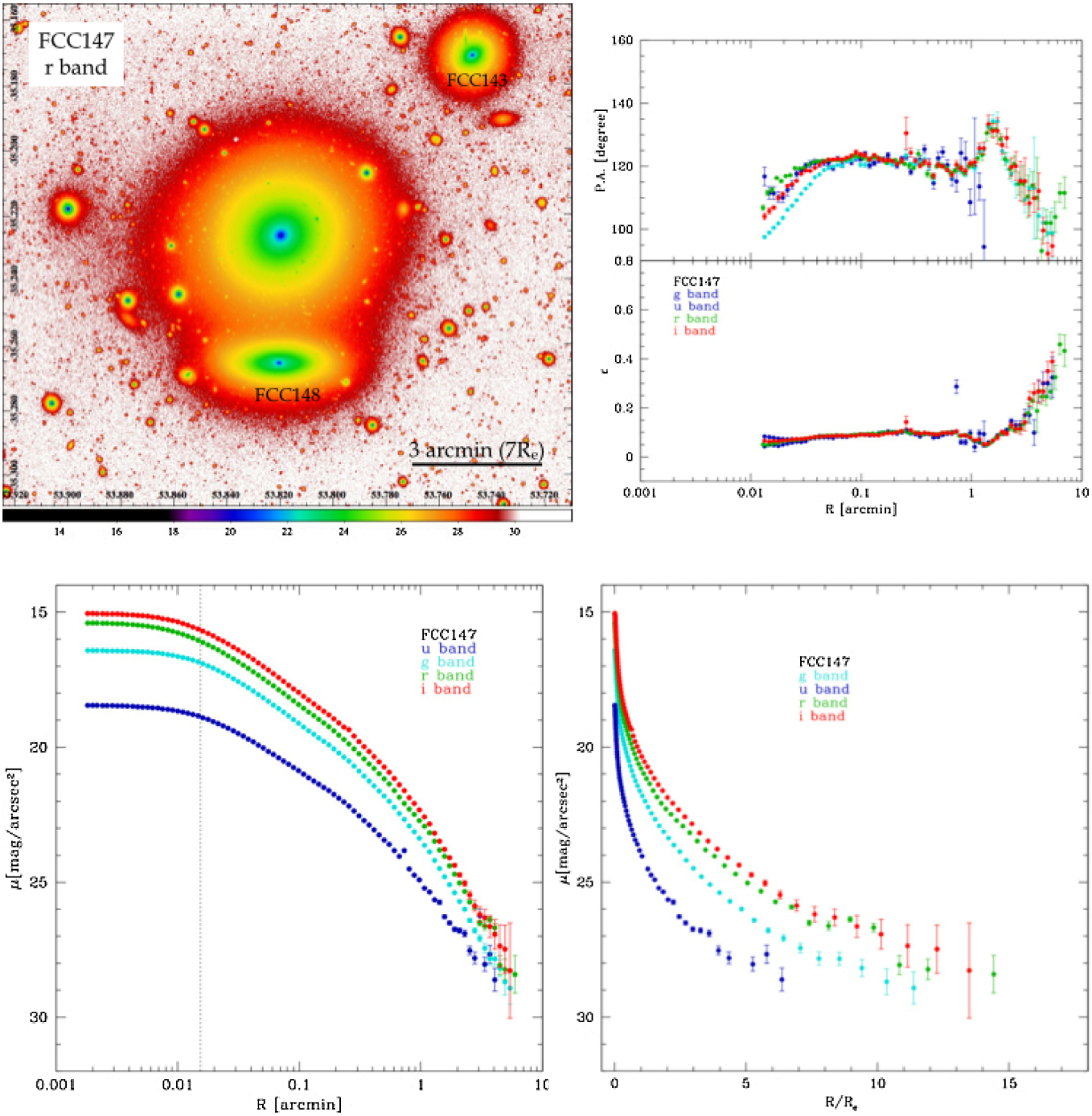

Fig. B.3. Surface photometry for FCC 147.

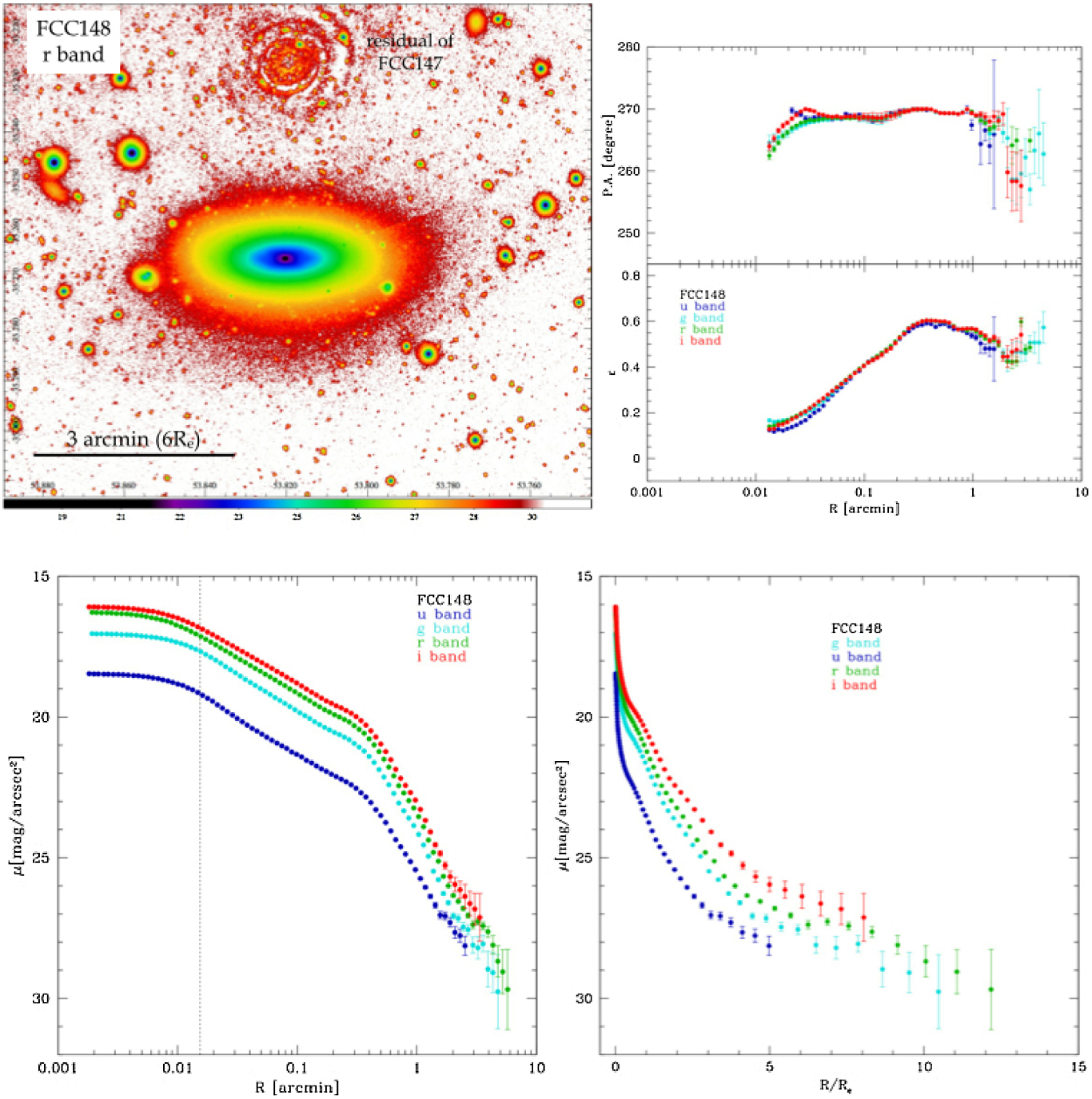

Fig. B.4. Surface photometry for FCC 148.

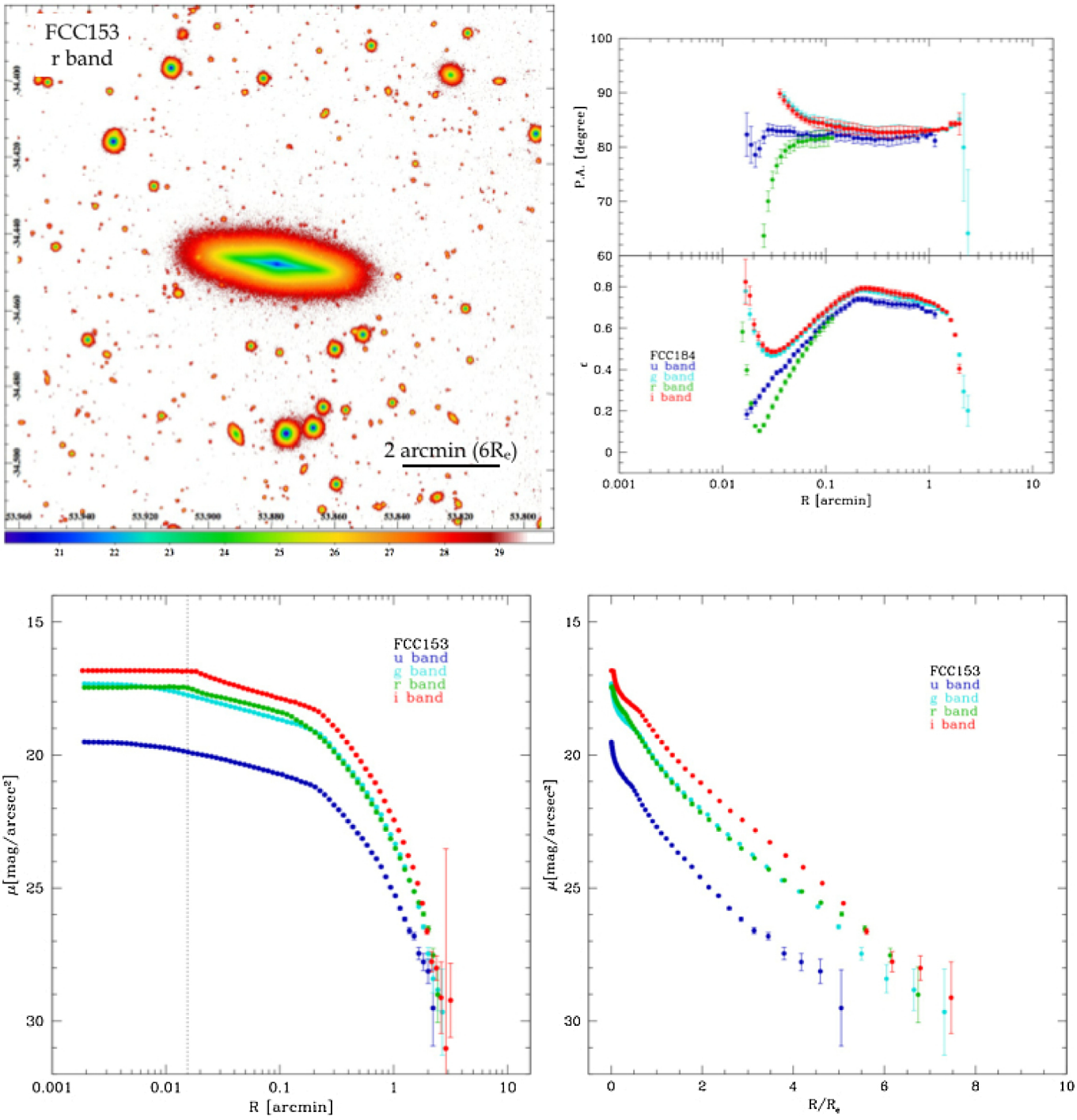

Fig. B.5. Surface photometry for FCC 153.

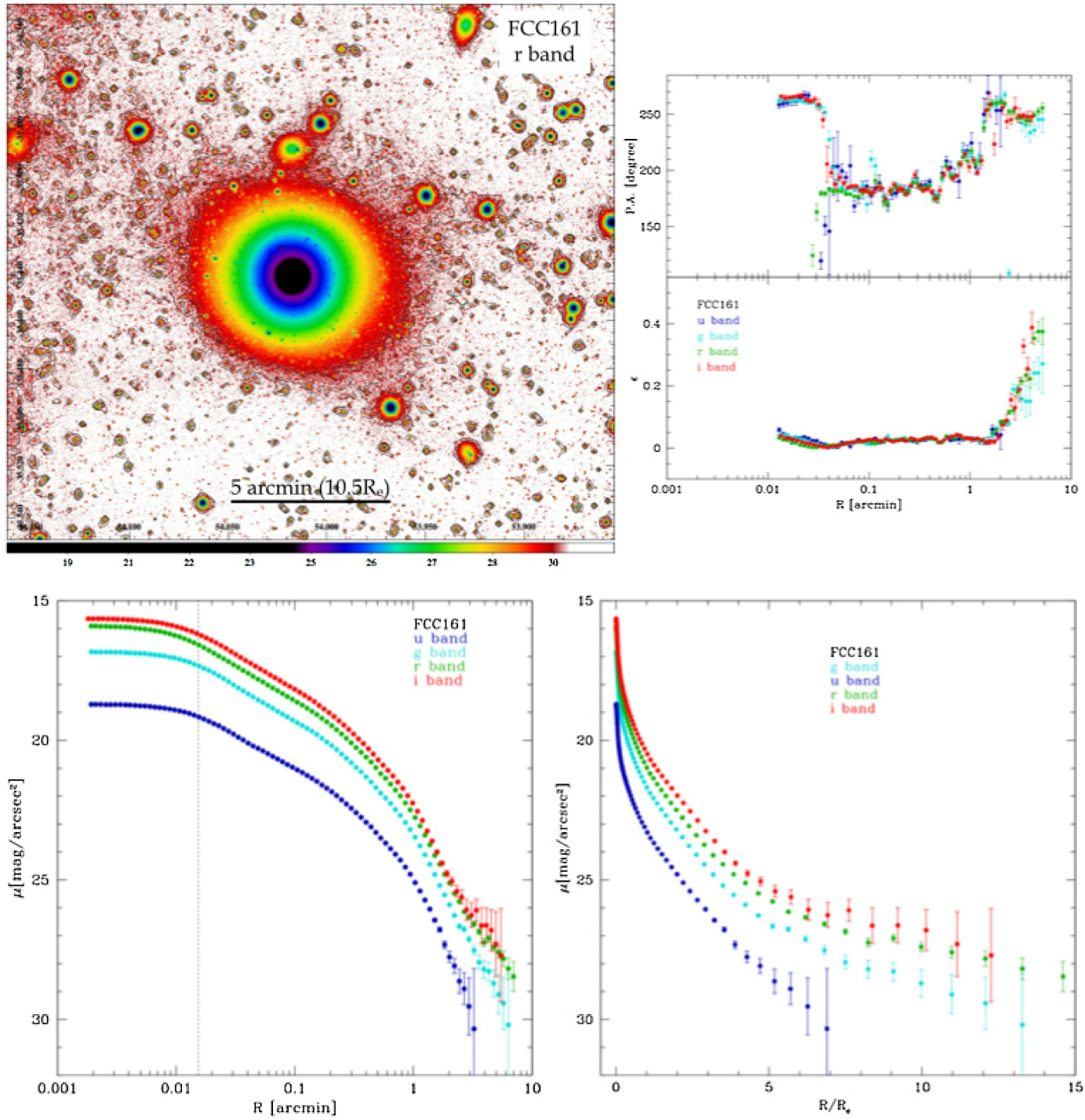

Fig. B.6. Surface photometry for FCC 161.

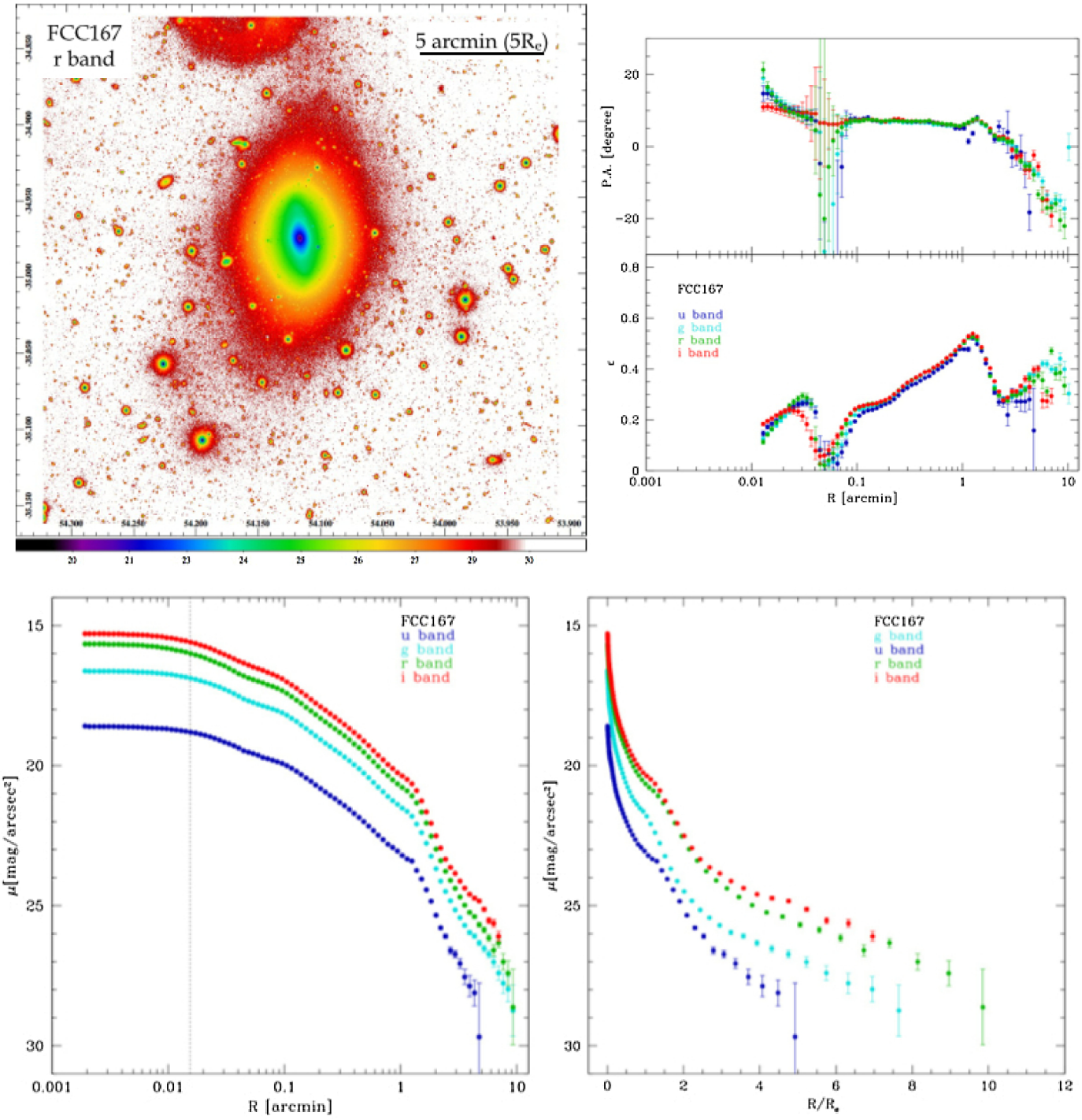

Fig. B.7. Surface photometry for FCC 167.

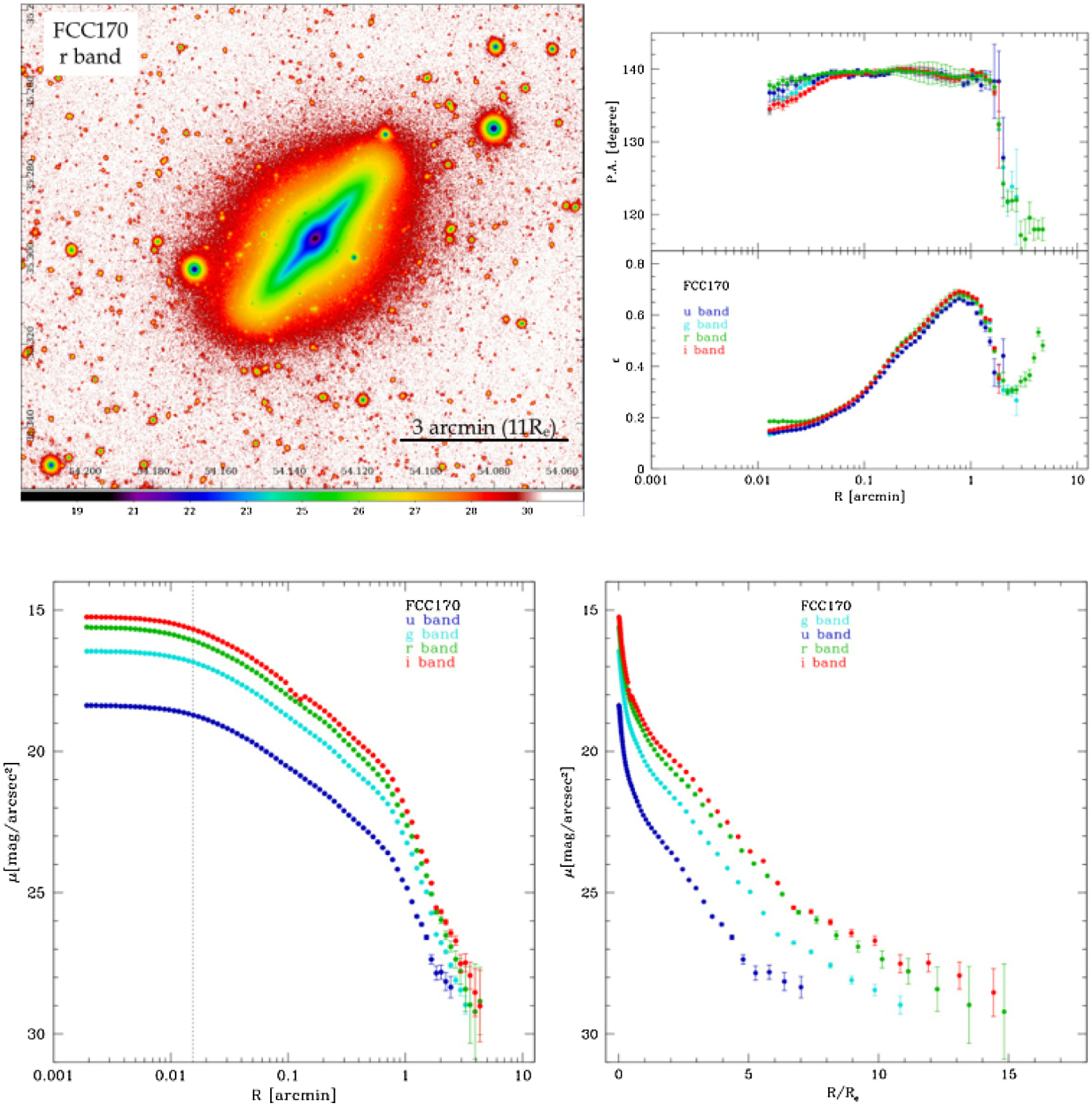

Fig. B.8. Surface photometry for FCC 170.

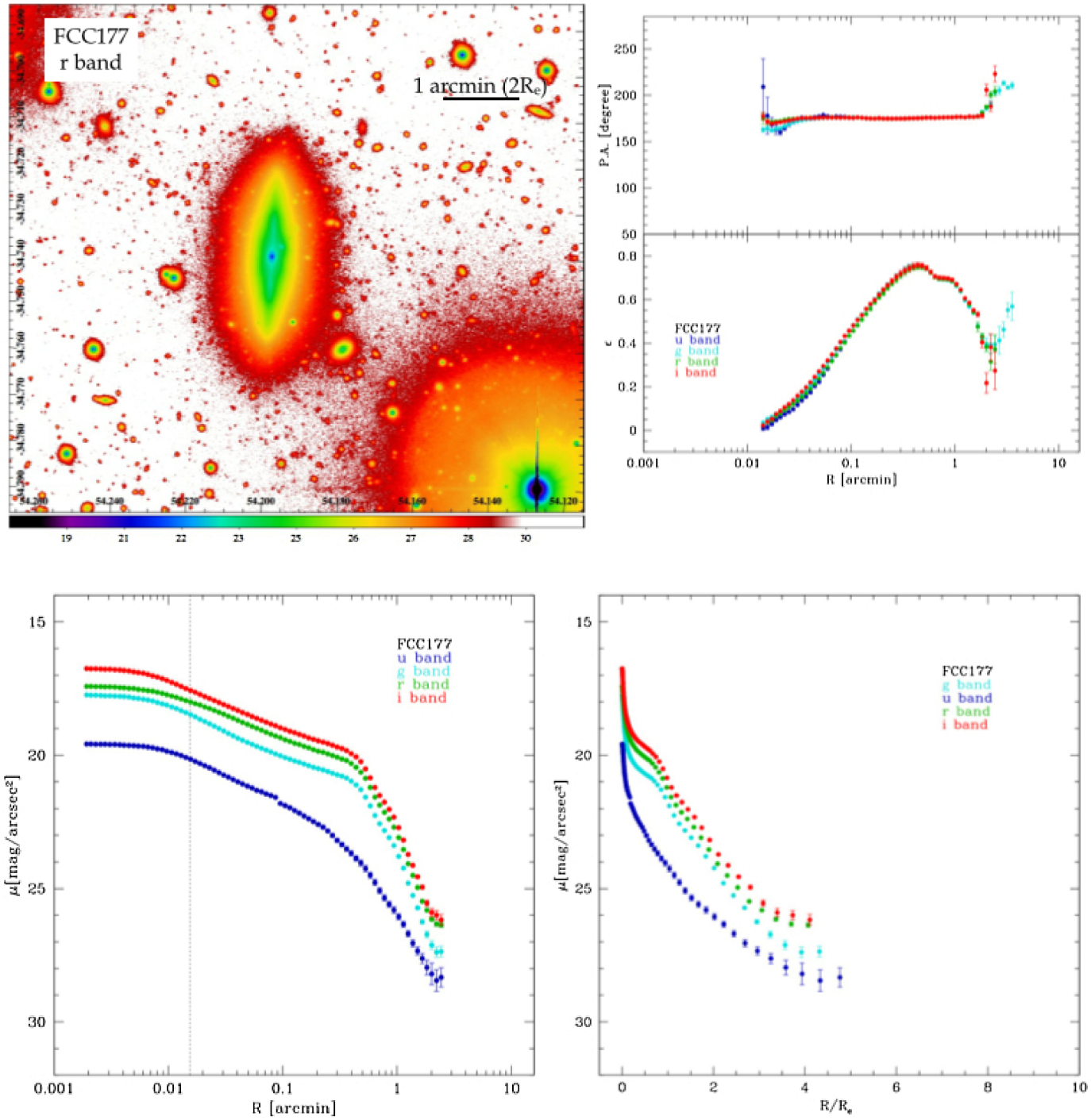

Fig. B.9. Surface photometry for FCC 177.

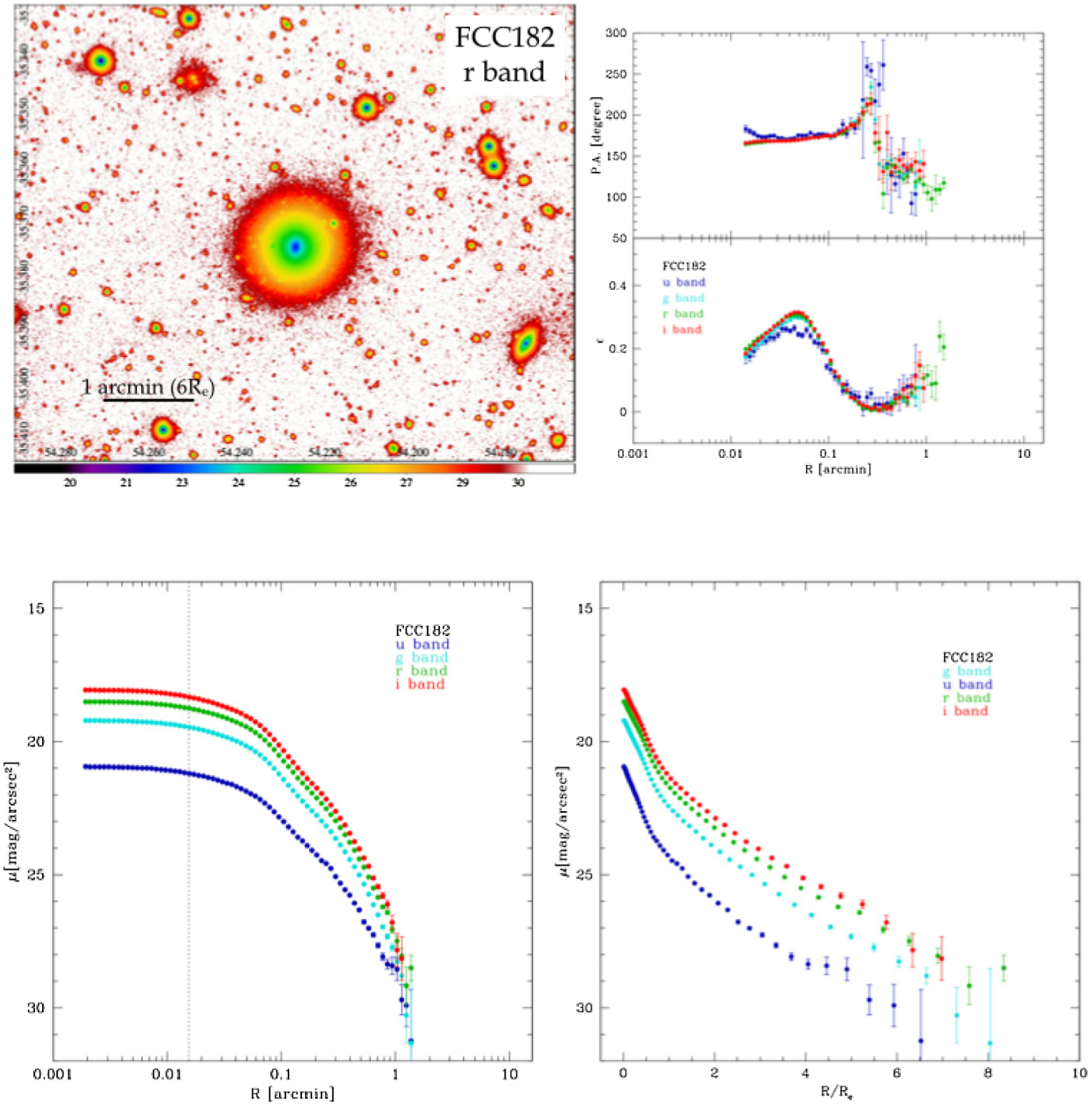

Fig. B.10. Surface photometry for FCC 182.

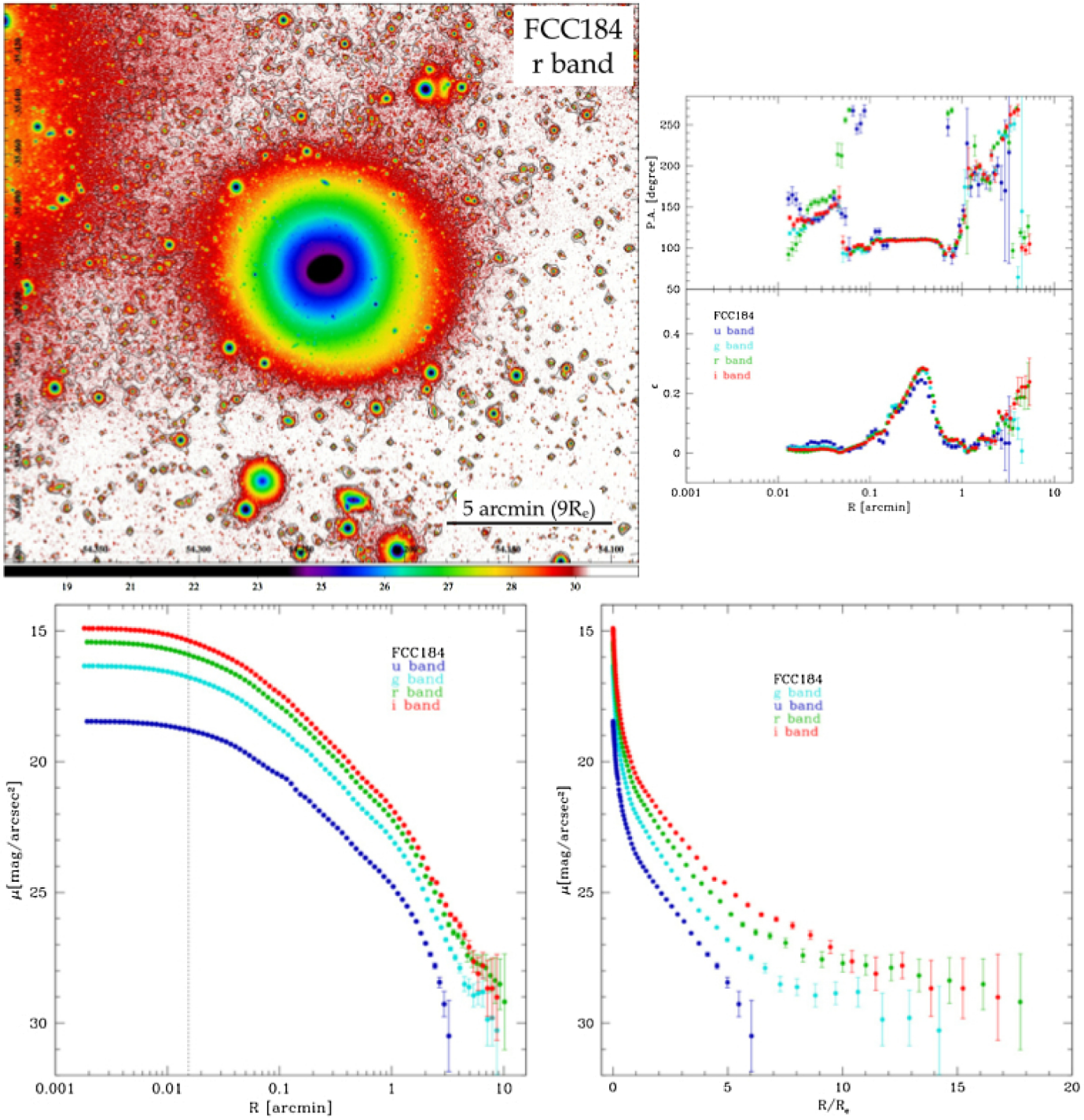

Fig. B.11. Surface photometry for FCC 184.

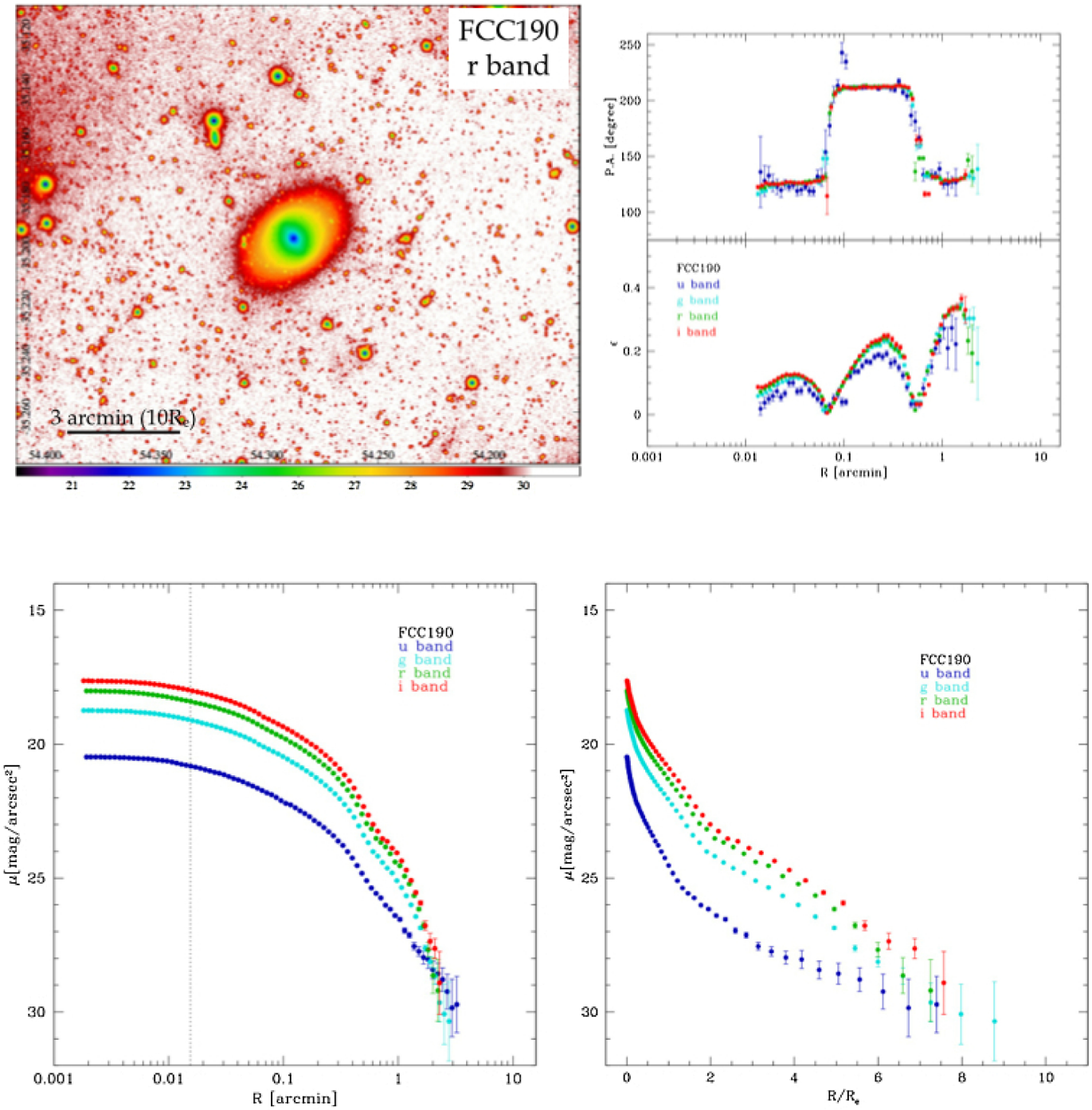

Fig. B.12. Surface photometry for FCC 190.

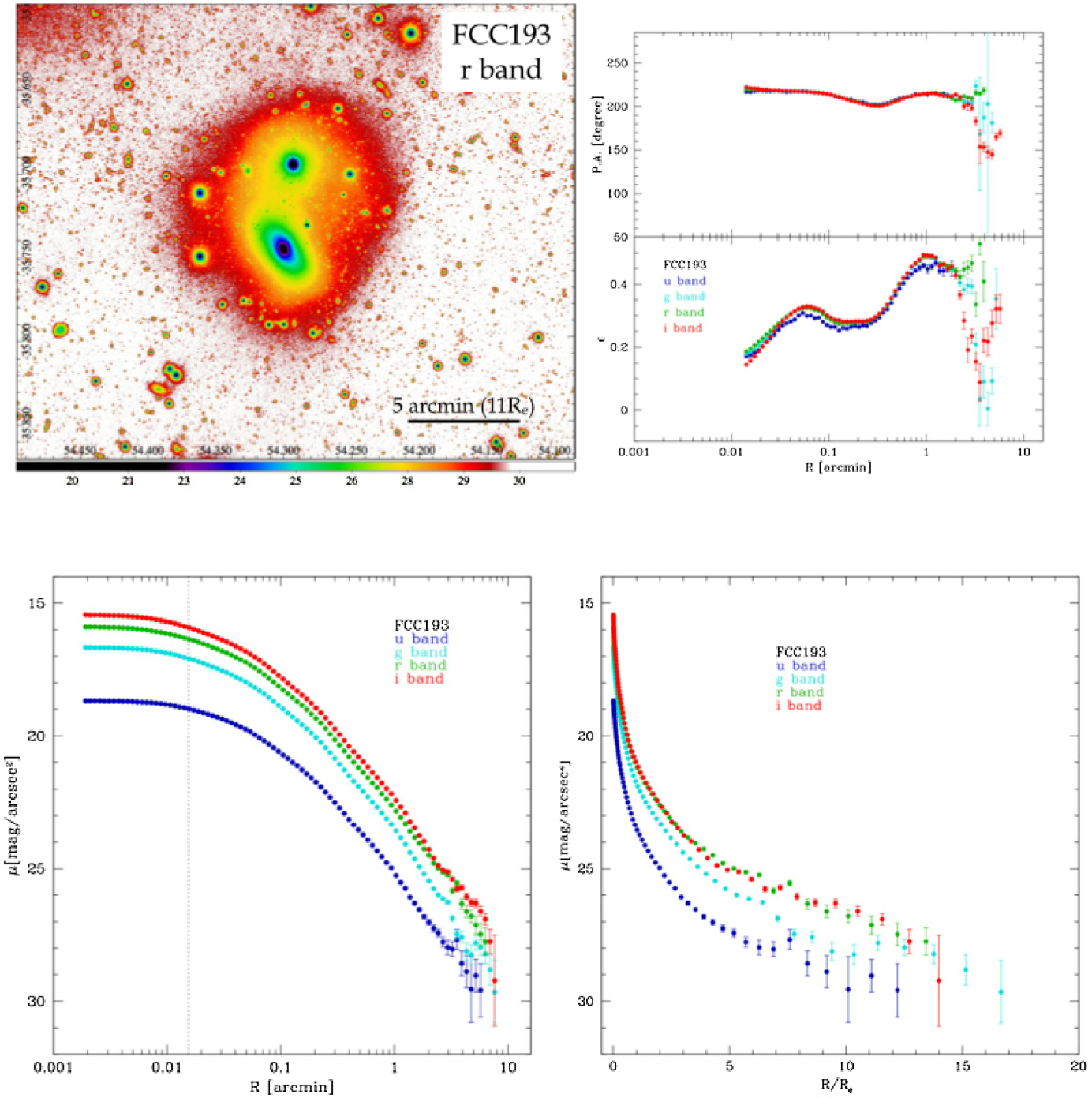

Fig. B.13. Surface photometry for FCC 193.

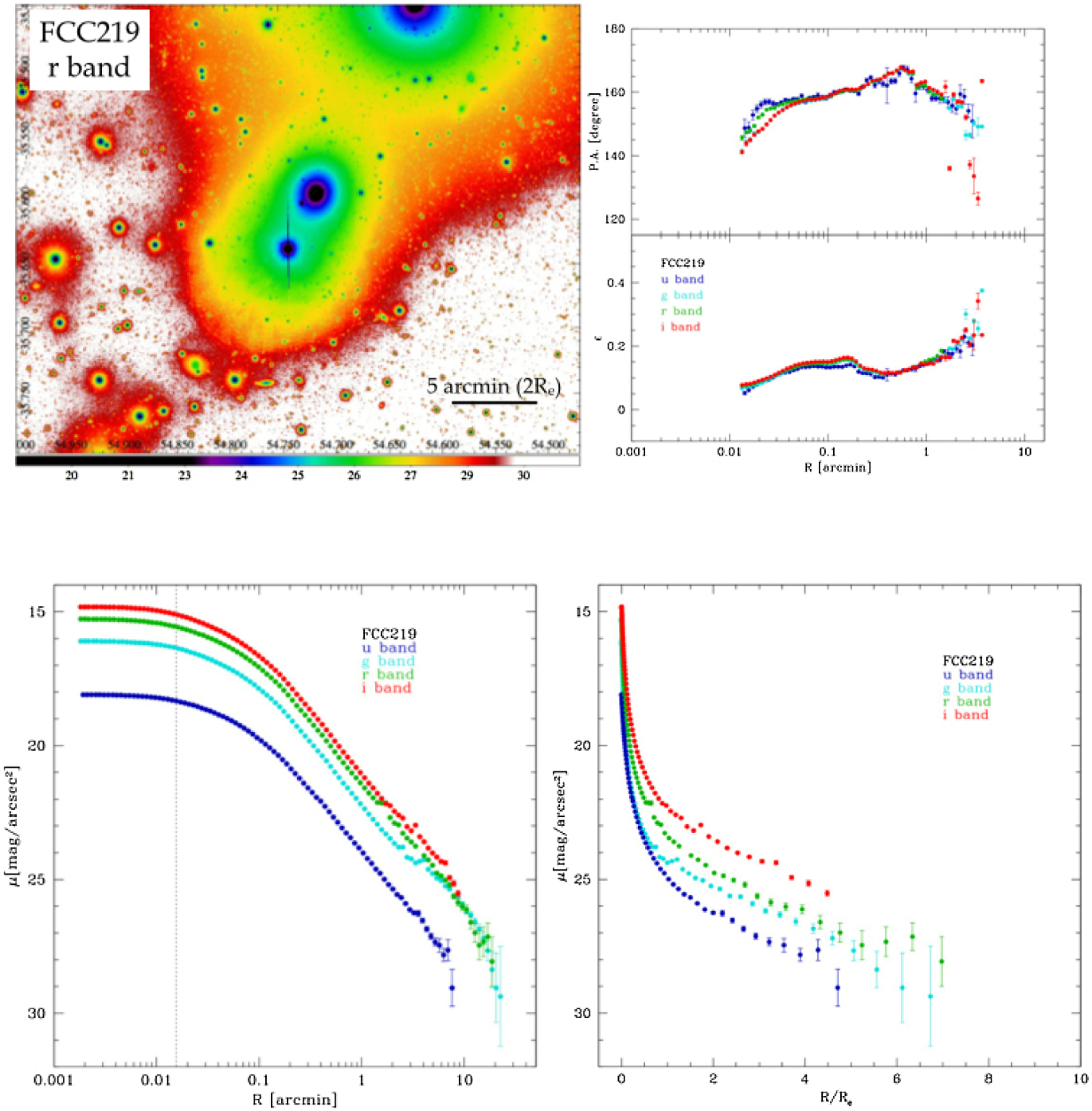

Fig. B.14. Surface photometry for FCC 219.

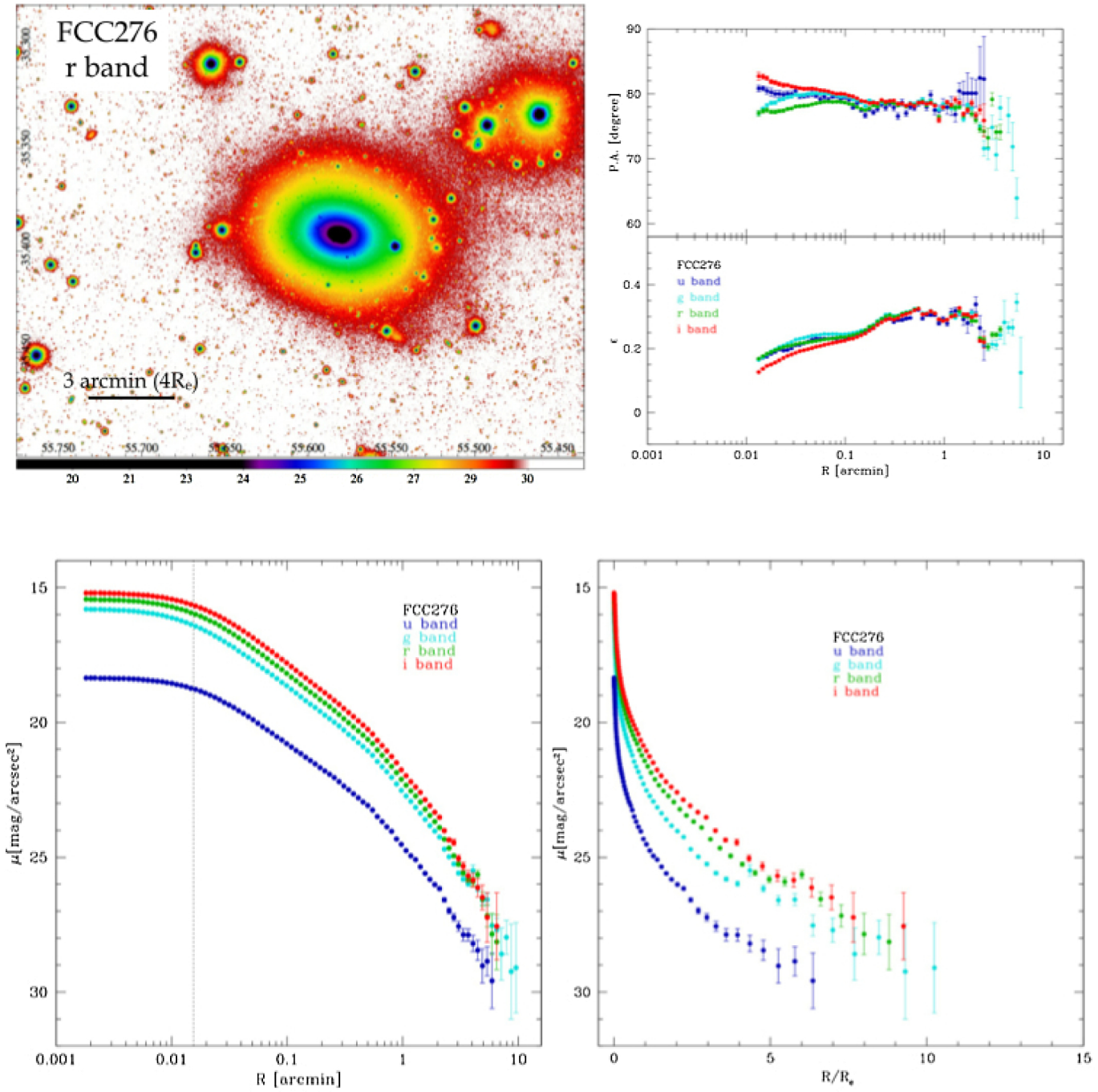

Fig. B.15. Surface photometry for FCC 276.

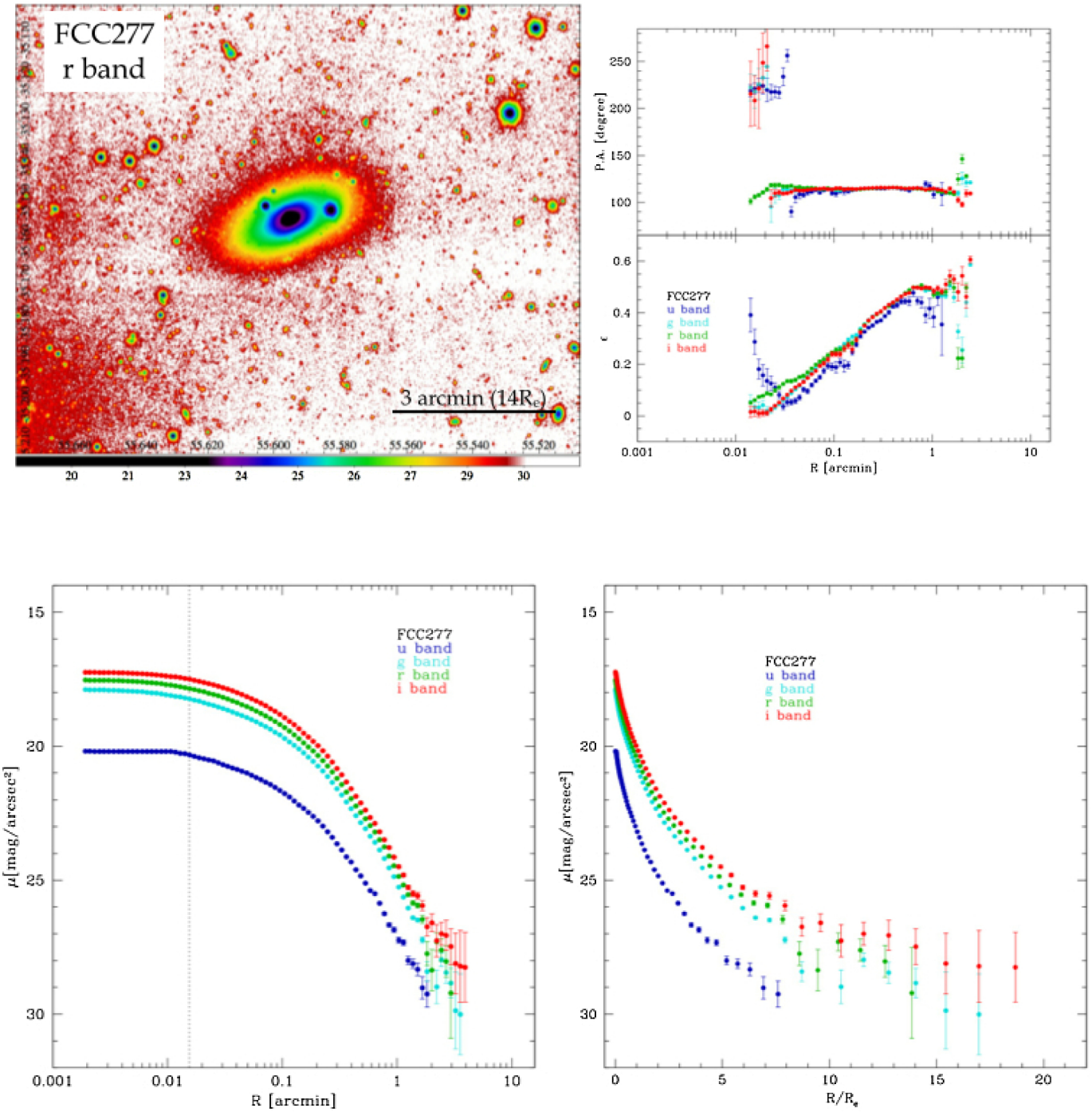

Fig. B.16. Surface photometry for FCC 277.

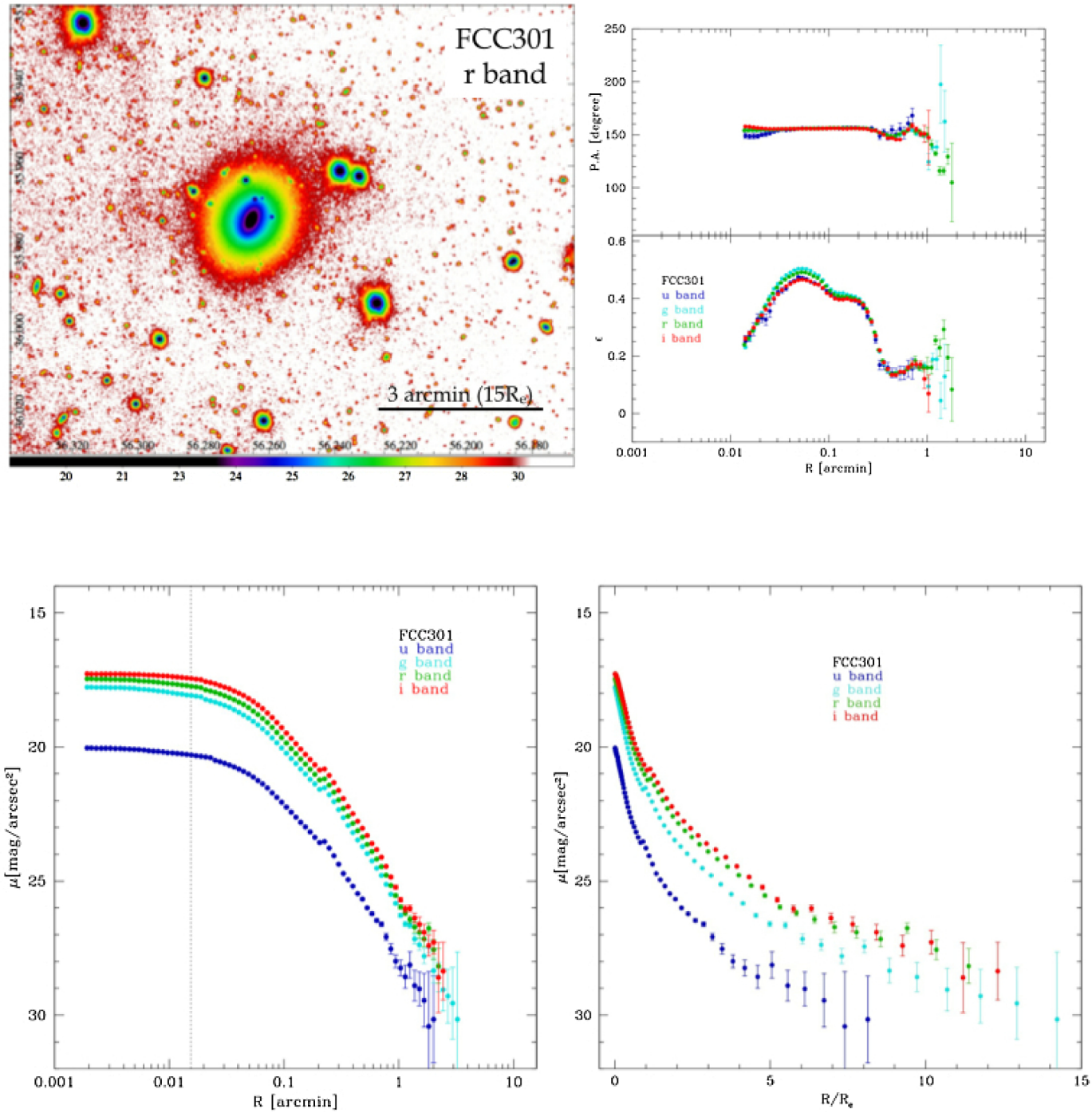

Fig. B.17. Surface photometry for FCC 301.

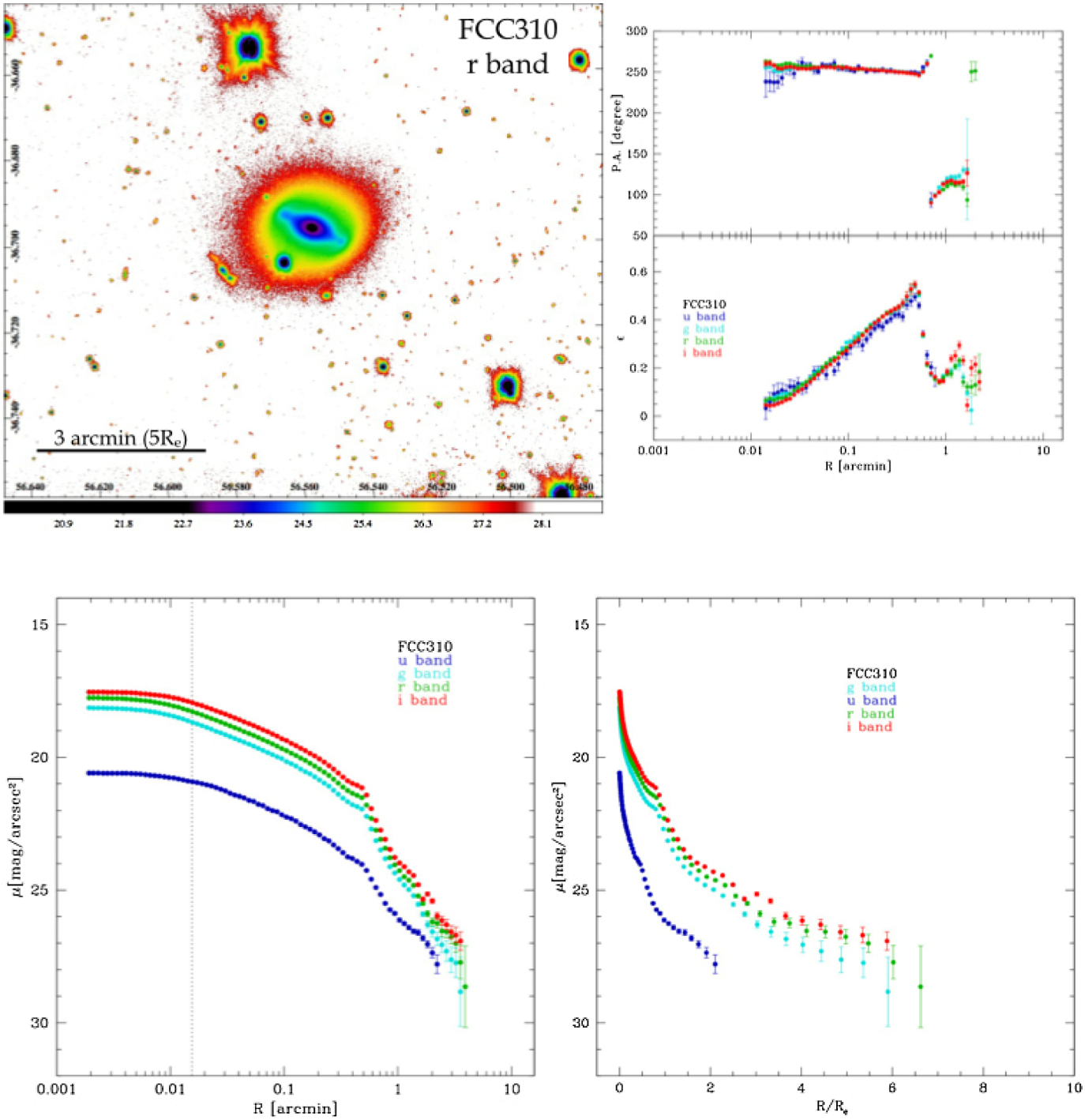

Fig. B.18. Surface photometry for FCC 310.

Appendix C: Colour distribution: 2D map and profiles

In each figure of this section we show the $g-i$ colour map and azimuthally averaged colour profile for each ETG of the sample.

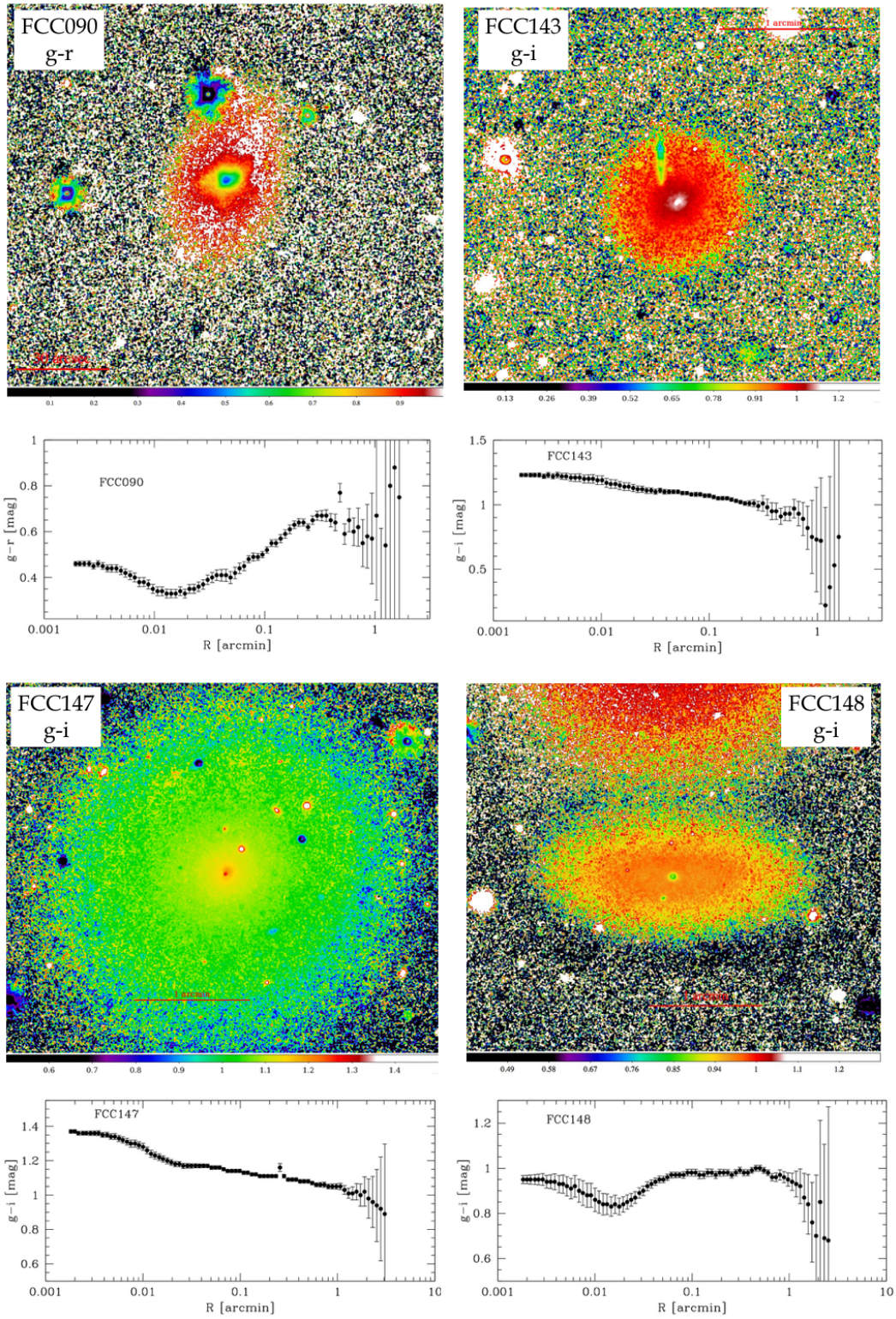

Fig. C.1. Colour maps and colour profiles ($g-i$) for FCC 090 (*top left panels*), FCC 143 (*top right panels*), FCC 147 (*lower left panels*), and FCC 148 (*lower right panels*).

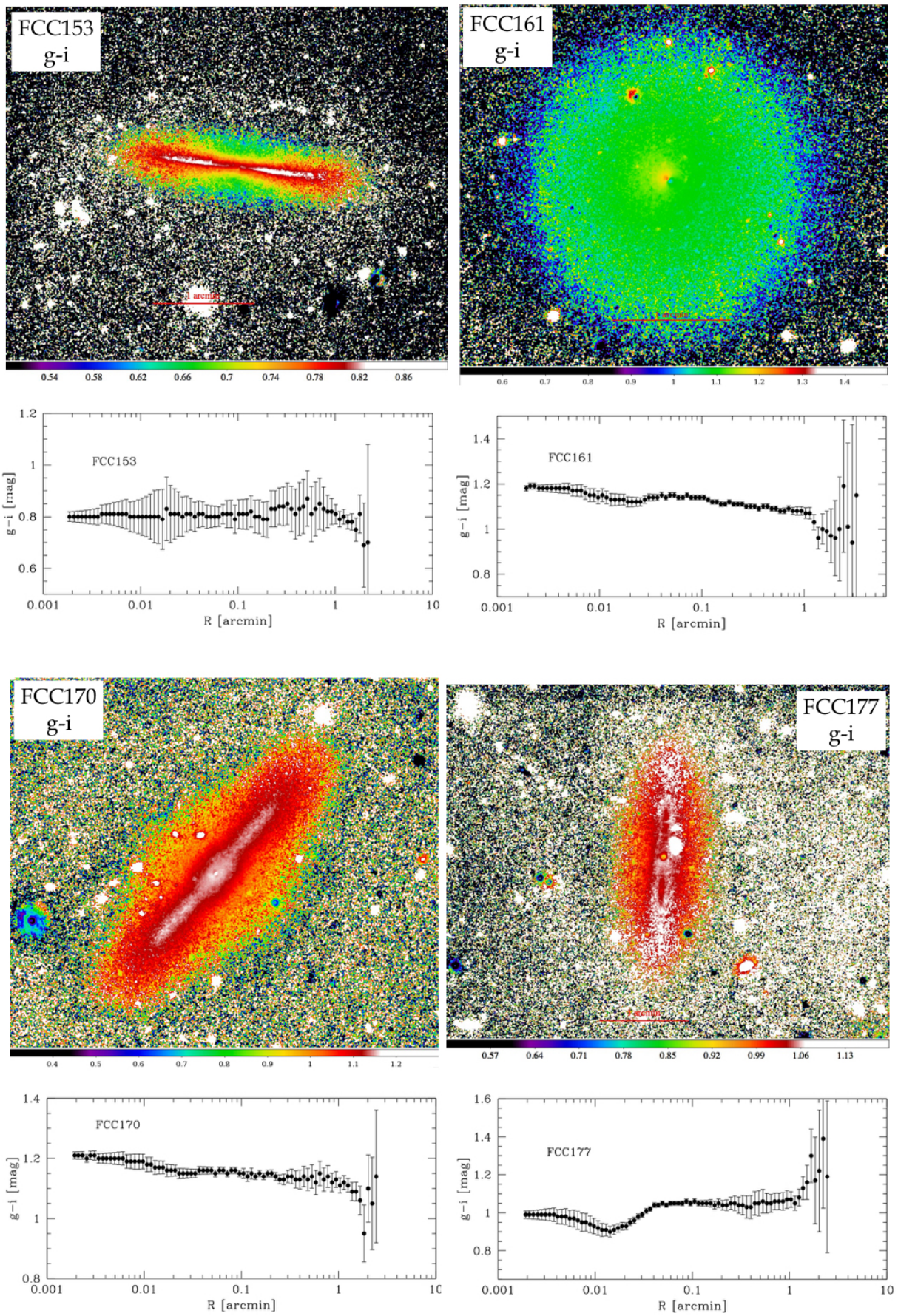

Fig. C.2. Colour maps and colour profiles ($g-i$) for FCC 153 (*top left panels*), FCC 161 (*top right panels*), FCC 170 (*lower left panels*), and FCC 177 (*lower right panels*).

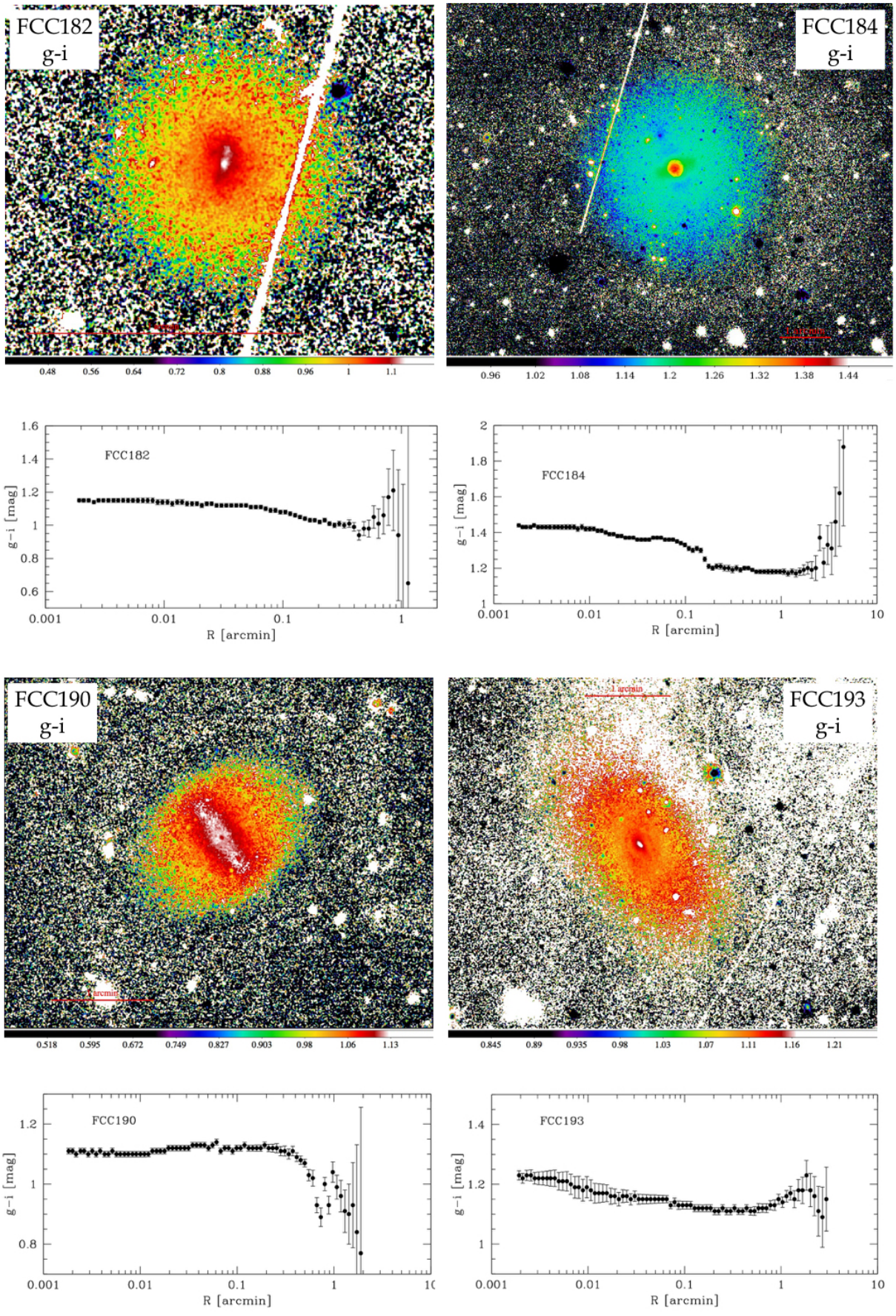

Fig. C.3. Colour maps and colour profiles ($g-i$) for FCC 182 (*top left panels*), FCC 184 (*top right panels*), FCC 190 (*lower left panels*), and FCC 193 (*lower right panels*).

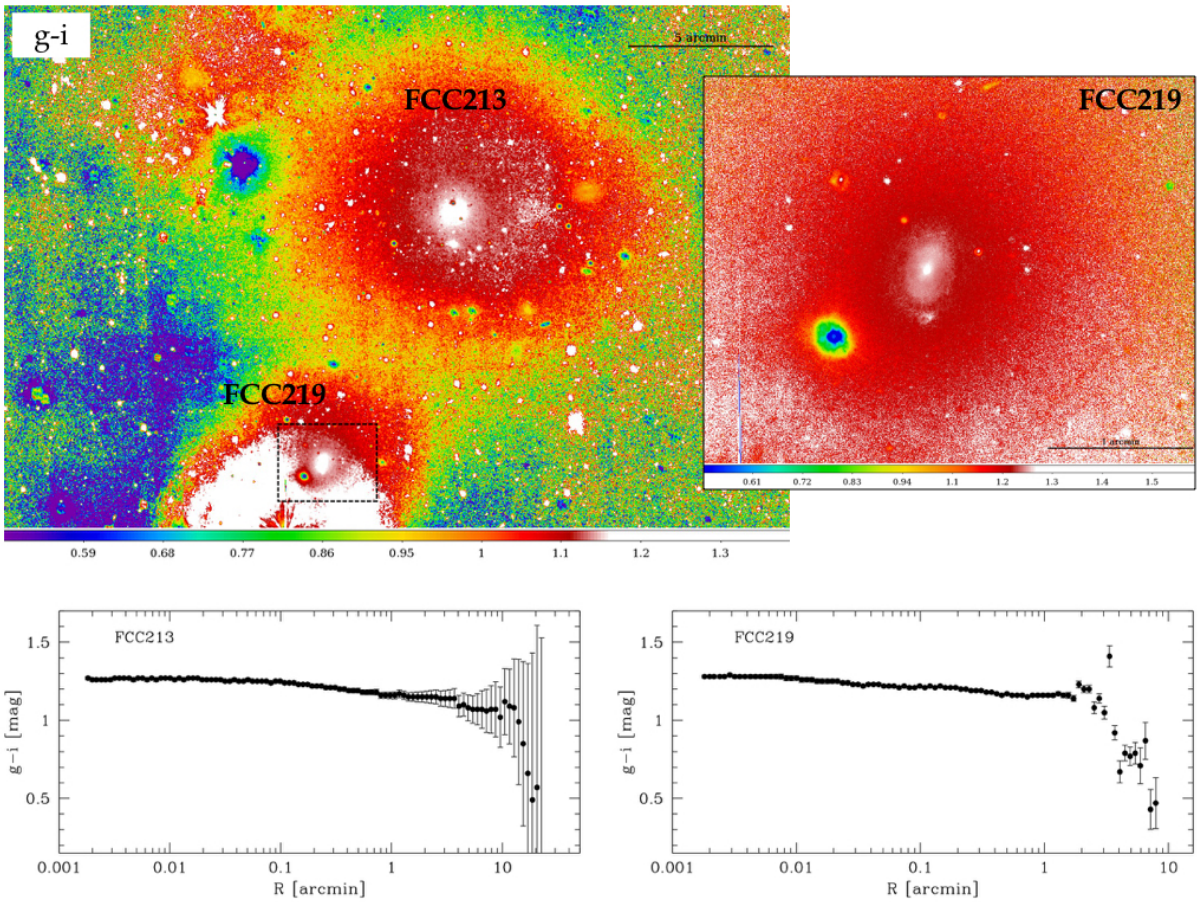

Fig. C.4. Colour map (*top panels*) and azimuthally averaged colour profiles (*bottom panels*), $g-i$, for the two bright ETGs in the core of the Fornax cluster, FCC213 and FCC219. The image size of the top left panel is 0.45×0.38°. In the top right panel there is an extracted image (3.4×2.6 arcmin) of FCC219 into the central regions (dashed box in the *top left panel*).

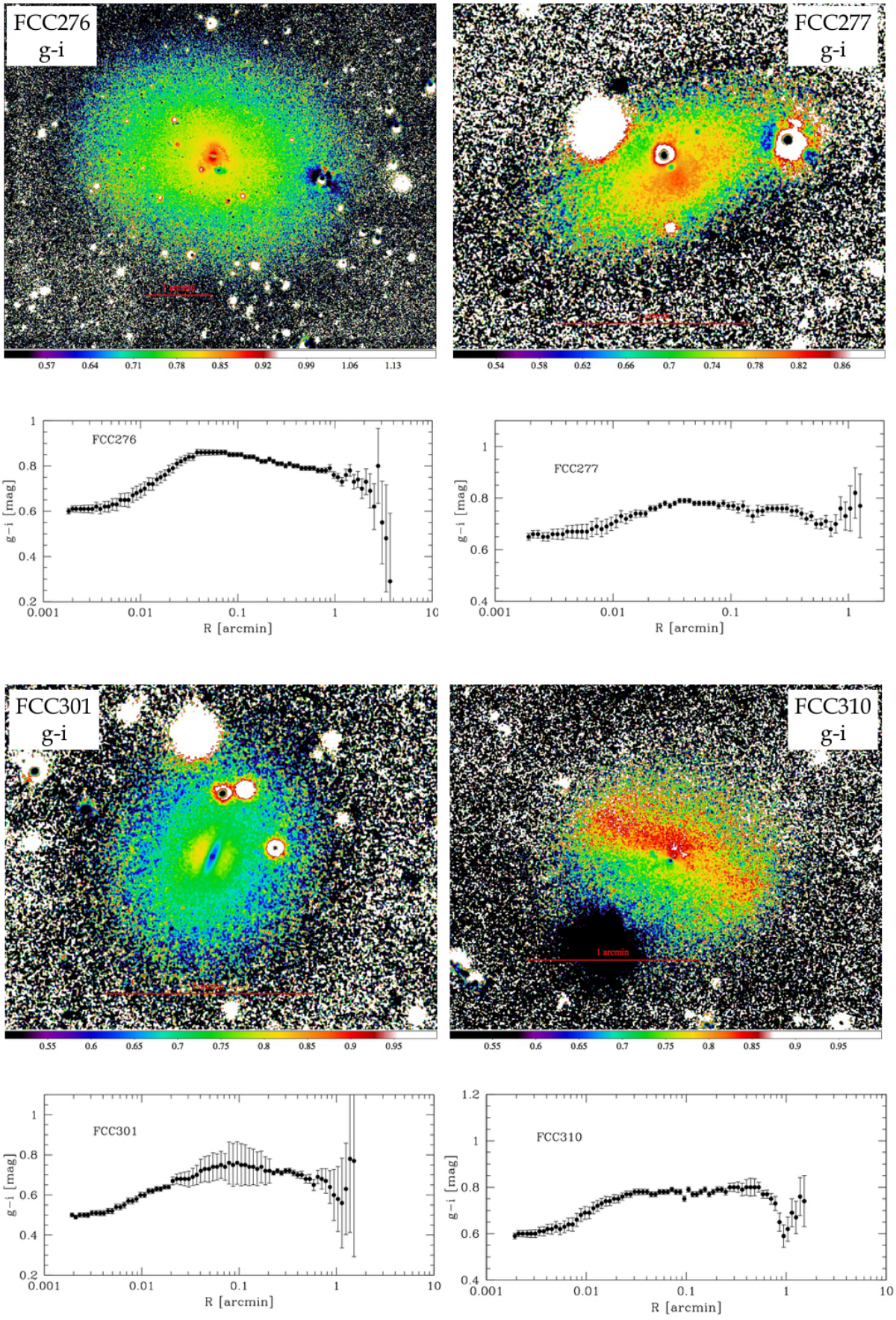

Fig. C.5. Colour maps and colour profiles ($g-i$) for FCC 276 (*top left panels*), FCC 277 (*top right panels*), FCC 301 (*lower left panels*), and FCC 310 (*lower right panels*).